E.O. Paton Electric Welding Institute of the National Academy of Science of Ukraine
International Association "Welding"

The Paton Welding Journal

08
2026

International Scientific-Technical and Production Journal ♦ Founded in January 2000 (12 Issues Per Year)

Address of Editorial Office:
E.O. Paton Electric Welding Institute, 11 Kazymyr Malevych Str., 03150, Kyiv, Ukraine
E-mail: office@paton.kiev.ua; https://paton.org.ua/en/

Address of Publisher:
International Association "Welding", 11 Kazymyr Malevych Str., 03150, Kyiv, Ukraine
Tel.: (38044) 205 23 90, E-mail: patonpublishinghouse@gmail.com; journal@paton.kiev.ua
https://patonpublishinghouse.com/eng/journals/tpwj

The Journal was registered by the National Council of Ukraine on Television and Radio Broadcasting on 09.05.2024, carrier identifier R30-04569
ISSN 0957-798X (Print), ISSN 3041-2293 (Online)
DOI: https://doi.org/10.37434/tpwj, from #01, 2020 to now; DOI: https: //doi.org/10.15407/tpwj from #01, 2014 to #12, 2019.

Subscriptions, 12 issues per year:
348 Euro — annual subscription for the printed (hard copy) version, air postage and packaging included;
288 Euro — annual subscription for the electronic version (sending issues in pdf format or providing access to IP addresses).

Representative Offices of "The Paton Welding Journal":

BRAZIL, Arc Dynamics
Address: Nova Iguacu, Rio de Janeiro, Brazil
Daniel Adolpho, Tel.: +55 21 9 6419 5703,
E-mail: dadolpho@arcdynamics.com.br

CHINA, China-Ukraine Institute of Welding, Guangdong Academy of Sciences
Address: Room 210, No. 363 Changxing Road, Tianhe, Guangzhou, 510650, China
Zhang Yupeng, Tel.: +86-20-61086791,
E-mail: patonjournal@gwi.gd.cn

BULGARIA, Bulgarian Welding Society
Address: Blvd. Asen Yordanov No.10, Sofia 1592, Bulgaria
Pavel Popgeorgiev, Tel.: +359 899 96 22 20,
E-mail: office@bws-bg.org

POLAND, PATON EUROPE Sp. z o. o.
Address: ul. Kapitałowa 4, 35-213, Rzeszów, Poland
Anton Stepakhno, Tel.: +38067 509 95 67,
E-mail: Anton.Stepakhno@paton.ua

The content of the Journal includes articles received from authors from around the world in the field of welding, cutting, cladding, soldering, brazing, coating, 3D additive technologies, electrometallurgy, material science, NDT and selectively includes translations into English of articles from the following journals, published in Ukrainian:

- «Avtomatychne Zvaryuvannya» (Automatic Welding), https://patonpublishinghouse.com/eng/journals/as;
- «Suchasna Elektrometalurhiya» (Electrometallurgy Today), https://patonpublishinghouse.com/eng/journals/sem;
- «Tekhnichna Diahnostyka ta Neruinivnyi Kontrol» (Technical Diagnostics & Nondestructive Testing), https://patonpublishinghouse.com/eng/journals/tdnk.

CONTENTS

ORIGINAL ARTICLES

INFORMATION

*Translated Article(s) from “Avtomatychne Zvaryuvannya” (Automatic Welding), No. 3, 2026.
**Translated Article(s) from “Avtomatychne Zvaryuvannya” (Automatic Welding), No. 4, 2026.
***Translated Article(s) from “Suchasna Elektrometalurhiya” (Electrometallurgy Today), No. 1, 2026.
****Translated Article(s) from “Suchasna Elektrometalurhiya” (Electrometallurgy Today), No. 2, 2026.
*****Translated Article(s) from “Tekhnichna Diahnostyka ta Neruinivnyi Kontrol” (Technical Diagnostics & Nondestructive Testing), No. 2, 2026.

Indexing: The electronic edition of “The Paton Welding Journal” is stored in the V.I. Vernadsky National Library of Ukraine (eVerLib), included in the OPEN UKRAINIAN CITATION INDEX database and international databases: CROSSREF, SCOPUS (www.scopus.com/sourceid/21101444671), EBSCO, Google Scholar, INDEX COPERNICUS, Scilit, ULRICHSWEB, BASE, Jisk, German Union Catalogue of Serials (ZDB), SCISPACE, TIB — Leibniz Information Centre for Science and Technology and University Library.

The purpose of “The Paton Welding Journal” is to emerging new scientific knowledge, to present a forum for discussing of new result in welding and related technologies which contribute to the creation of new technologies and engineering samples with improved technical and economic performance and to facilitate their implementation. That is why in articles published in the journal, the emphasis is on both scientific novelty and practical value. Extensive cooperation of the Journal with research institutes, educational centers and industrial makes it possible to review articles by leading experts and to involve in the publication of advanced research results.

DOI: https://doi.org/10.37434/tpwj2026.08.01

FEATURES OF FORMATION OF THE STRUCTURE AND BALLISTIC RESISTANCE OF ARMOR STEEL WELDED JOINTS PRODUCED BY PULSED PLASMA ARC WELDING WITH COMBINED ALLOYING OF THE WELD METAL

O.A. Slyvinskyy[1,2], V.D. Poznyakov[2], V.M. Korzhyk[2], Ye.V. Illiashenko[2], S.P. Bisyk[3]

[1]National Technical University of Ukraine "Igor Sikorsky Kyiv Polytechnic Institute"
37 Prosp. Beresteiskyi, 03056, Kyiv, Ukraine
[2]E.O. Paton Electric Welding Institute of the NASU
11 Kazymyr Malevych Str., 03150, Kyiv, Ukraine
[3]National Defence University of Ukraine
28 Prosp. Povitrianykh Syl, 03049, Kyiv, Ukraine

ABSTRACT

The results of a study on the effect of pulsed-plasma welding with combined alloying of the weld metal using an austenitic filler wire and an insert rod on the structure formation and ballistic resistance of welded joints of modern high-hardness armor steels Armox 500T and Mars 600 are presented. It was established that pulsed-plasma welding ensures the formation of full-penetration butt joints with a thickness of 5–6 mm without edge preparation at a specific heat input of $Q/\delta \approx 0{,}16$ kJ·mm^{-2}. It is shown that at the same level of thermal input, welded joints of Mars 600 steel are characterized by a smaller width of the softened subzone within the heat-affected zone compared to Armox 500T steel, due to the increased resistance of the silicon-alloyed initial martensitic structure to short-term tempering. It was established that the combined alloying of the weld metal with OK Autrod 16.95 filler wire and OK Tigrod 308L insert rod, combined with a high proportion of the base metal in the weld formation, ensures the creation of high-strength martensitic-type structures. In the welded joints of Armox 500T steel, a martensitic-bainitic structure of the weld metal is formed, with a hardness that is not inferior to the hardness of the base metal. For Mars 600 steel, the formation of a heterogeneous martensitic structure of varying dispersion along the weld height was observed. In the upper part of the weld, a refined structure with signs of structureless martensite was detected. Based on the results of EDX and NDIR analysis, an uneven distribution of carbon and alloying elements along the weld height was established. The possible influence of the pulsating constricted plasma arc on the intensification of mass transfer and mixing of the weld pool metal is discussed, which may be one of the factors contributing to the formation of the observed structural anisotropy of the weld metal. Ballistic testing confirmed that the developed technology of pulsed-plasma welding with combined alloying of the weld metal ensures producing the welded joints of armor steels of various hardness classes with ballistic resistance equivalent to that of the base metal.

KEYWORDS: high hardness armor steel, pulsed plasma arc welding, combined alloying of the weld metal, structure formation, martensitic structures, heat-affected zone, ballistic resistance

INTRODUCTION

Rolled sheets 2 to 20 mm thick from armor steels heat-treated to a high hardness of *HBW* 4.9–5.9 GPa are widely used for manufacture of the military and special equipment structures with armor protection from small arms bullets, as well as fragments of shells and mines. At present mechanized consumable electrode gas-shielded welding in active shielding gas (MAG) with application of high-alloyed Cr–Ni–Mn welding wires of austenitic class is the most common method of joining these materials in production [1]. Under the condition of minimal degree of mixing of the deposited and base metal the weld forms an austenitic or austenitic-ferritic structure, ensuring the required level of fatigue strength [2] and cold cracking resistance [3] of the welded joints. At the same time, a disadvantage of such a technological solution is a significant structural and mechanical mismatch between the metal of the weld, heat-affected zone (HAZ) and base metal of the armor. In particular, a microhardness gradient on the line of fusion of the weld and the HAZ overheated region is equal to 3.5–4.5 GPa·mm^{-1} on average [4, 5]. Compared to the base metal, which usually has a homogeneous structure of fine-acicular tempered martensite, the metal of the austenitic weld has considerably lower values of dynamic strength and hardness, and is inferior to it by the ballistic resistance values [6].

One of the promising ways of solving this problem is controlled formation of the structural-phase composition of the weld metal due to an increase of the proportion of base metal in its composition and controlling the conditions of crystallization and phase transformations [7].

The previous research shows the possibility of increasing the hardness of armor steel weld metal by applying TIG-welding [8], hybrid laser-arc [9] and hybrid plasma-arc process [10, 11]. Promising is the application of pulsed-plasma welding, which combines the high energy concentration of the plasma arc with the possibility of independent adjustment of the heat input and quantity of filler metal. Such features of the process create the prerequisites for a controlled influence on the proportion of the base metal in the weld, intensification of mixing of the weld pool metal and formation of structures with higher strength and ductility values. Here, pulsation of current of the constricted plasma arc affects not only the thermal regime of the process, but also the hydrodynamic condition of the weld pool. The periodical change in current is accompanied by a change in the current density, degree of arc constriction, plasma flux velocity and its pressure on the melt surface. It results in enhancement of the convective flux mass transfer into the weld pool, which promotes more intensive mixing of the base and filler metals [12–16].

This is of particular importance for armor steel joints, as increase of the base metal proportion in the weld promotes the preservation of a sufficient carbon content in it for formation of martensitic-type structures. Moreover, intensification of mixing creates the preconditions for a more uniform distribution of alloying elements in the weld metal and a controlled formation of its structural-phase state [14–16].

In [5] it was found that the pulsed-plasma welding of armor steels allows an essential reduction of filler metal losses, compared to MAG welding, which promotes formation of a predominantly martensitic structure in the weld metal with hardness close to or even higher than that of the base metal. Owing to the features of low-temperature transformation of austenite a favourable residual stressed state is ensured in the weld metal that increases the cold cracking resistance of the joints [5].

At the same time, there are practically no data in the available literature as to the influence of such structural changes on the ballistic resistance of armor steel welded joints. The features of structure formation and weld metal ballistic resistance in case of simultaneous application of several high-alloy welding consumables and the influence of the pulsating plasma arc on the mass transfer and structure formation processes, remain particularly insufficiently studied.

THE AIM

of the work is to establish the regularities of formation of the structure, hardness, and ballistic resistance of the welded joints of armor steels for ballistic protection, which were produced by pulsed-plasma welding with combined alloying of the weld metal by filler and insert welding consumables of austenitic class.

MATERIAL AND METHODS OF INVESTIGATION

Investigations were conducted using rolled sheets from steels of two grades: Armox 500T and Mars 600. By its chemical composition (Table 1) and mechanical properties the rolled sheets from Armox 500T steel correspond to US DOD standard for high hardness armor (~500 *HB*) [17], and that from Mars 600 steel — to ultra-high hardness armor (~600 *HB*) [18].

Automatic pulsed-plasma welding was performed using PLAZER-300 EMF unit (Manufacturer **“**SCIENCE-PRODUCTION CENTER “PLAZER”, Ukraine, TU U 27.9-38388946-001:2025). Butt joints of plates from Armox 500T steel 5.4 mm thick, from Mars 600 steel — 6.2 mm thick, without edge preparation were produced on a copper backing with a machined backing groove. Plasma-forming gas Ar and shielding gas — a mixture of Ar + 18 % CO_2 — were applied. Results of works [19–22] were used during selection of the optimal welding modes.

A feature of the welding technology was simultaneous application of two welding consumables of different brands (Table 1). ESAB OK Autrod 16.95 filler wire 1.0 mm in diameter was used. In addition to it, an ESAB OK Tigrod 308L insert rod 1.2 mm in diameter was placed in the gap between the plates to be welded during welding of Mars 600 steel and a rod 1.0 mm in diameter was used for welding Armox 500T steel plates, in order to control the structural-phase composition of the weld. The rod was located at ~1.0 mm distance from the lower plane of the plates being joined.

The welding mode parameters (Table 2) were selected in order to ensure a complete penetration of the joints in one pass, with simultaneous minimizing of the heat input into the base metal: I_{av} — average value of modulated current, applied for energy input calculation; I_p and

Table 1. Chemical composition of the base materials and welding consumables, wt.%

Material	C	S	P	Si	Mn	Ni	Cr	Mo	B	Al
Base material										
Armox 500T	0.28	0.002	0.007	0.24	0.85	0.90	0.50	0.354	0.001	0.050
Mars 600	0.43	0.0006	0.0054	0.82	0.499	1.881	0.15	0.33	0.0028	0.035
Welding consumables										
OK Autrod 16.95	0.06	0.010	0.020	0.80	6.70	8.10	18.2	0.10	–	–
OK Tigrod 308L	0.018	0.007	0.018	0.33	2.0	10.3	20.0	0.11	–	–

Table 2. Parameters of the modes of experimental sample welding

Sample material	I_{av}, A	I_p, A	I_{paus}, A	f, Hz	S	U_w, V	V_f, m/min	V_w, mm/s	Q, kJ·mm^{-1}
Mars 600	213	290	180	300	3.3	26.0	1.9	3.3	1.0
Armox 500T	201	280	170	300	3.3	25.7	1.6	3.6	0.86

I_{paus} — pulse and pause current; f and S — pulse frequency and duty cycle; U_w — average value of welding current; v_f and v_w — filler wire feed rate and welding speed. Energy input Q was calculated for the value of effective heating efficiency of plasma welding $\eta = 0.6$ according to DSTU ISO/TR 17671-1:2015.

Microstructure of the welded joints was studied in a metallographic microscope iScope IS.1053-PLMi (etchants: 4 and 15 % solution of nitric acid in ethyl alcohol to reveal the structure of the base metal and weld metal, accordingly) and in a scanning electron microscope TESCAN VEGA 3.

Vickers durometric test was conducted in microhardness meter LHVS-1000Z with the load of 2.94 N (300 g) in the welded joint cross-section in two measurement directions (Figure 1): at the depth of 1.5 mm from the face plane of the joined plates (direction x), as well as by the weld height — along their vertical axis (direction y).

Analysis of the chemical composition of the welds was conducted by the method of energy-dispersive X-ray (EDX) spectroscopy by mapping the surfaces of metallographic sections of 1×1 mm area and non-dispersion infrared-absorption (NDIR) spectroscopy using Horiba EMIA PRO detector.

Ballistic tests were conducted at the accredited Research Center for Testing, Expertise, and Certification of Personal Armored Protection Equipment of the National University of Defence of Ukraine to verify the compliance of welded samples with the protection class according to DSTU 3975-2000 "Armour Protection of Specialized Cars. General Technical Requirements". "The shooting was carried out from a distance of 10 m at an impact angle of 90° with 5.45 mm caliber bullets (5.45×39 assault rifle cartridge) of two types: PS with a core made of 65G steel heat-treated to a hardness of 56–60 *HRC*, and PP (improved penetration) with a conical core made of steel 75 with a hardness of 60 *HRC*.

EXPERIMENTAL RESULTS

Within the HAZ of the studied welded joints, the results of microdurometric analysis (Figure 2) demonstrate a pattern of a change in hardness with greater distance from the weld, which is typical for welding the quenched and tempered steels, in particular armor steels.

Metal of the overheated complete recrystallization sections (HAZ1), which underwent austenitization during heating, after cooling has the maximal hardness, which is higher than that of the base metal (declared by manufacturers of both the steels minimal guaranteed base metal hardness in the heat-treated state is marked by horizontal dashed lines). Within the incomplete recrystallization and tempering regions (HAZ2), the hardness drop below the level of the base metal hardness values occurs as a result of the processes of tempering and recrystallization of the initial structure which are due to the influence of the welding heat. At the same time, microhardness distribution within the welds in the horizontal (x) and vertical (y) measurement directions is indicative of formation of high-hardness structures of the order of HAZ1 metal hardness.

Comparison of the results of durometric analysis of welded samples of Armox 500T and Mars 600

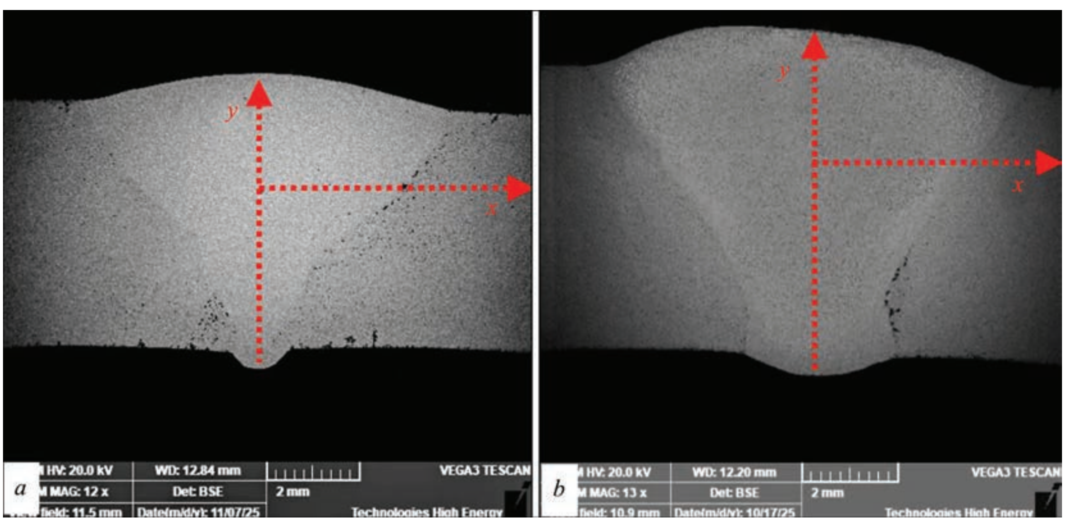

Figure 1. Shape of penetration of armor steel welded joints with marked directions of microhardness measurement: *a* — Armox 500T steel; *b* — Mars 600 steel

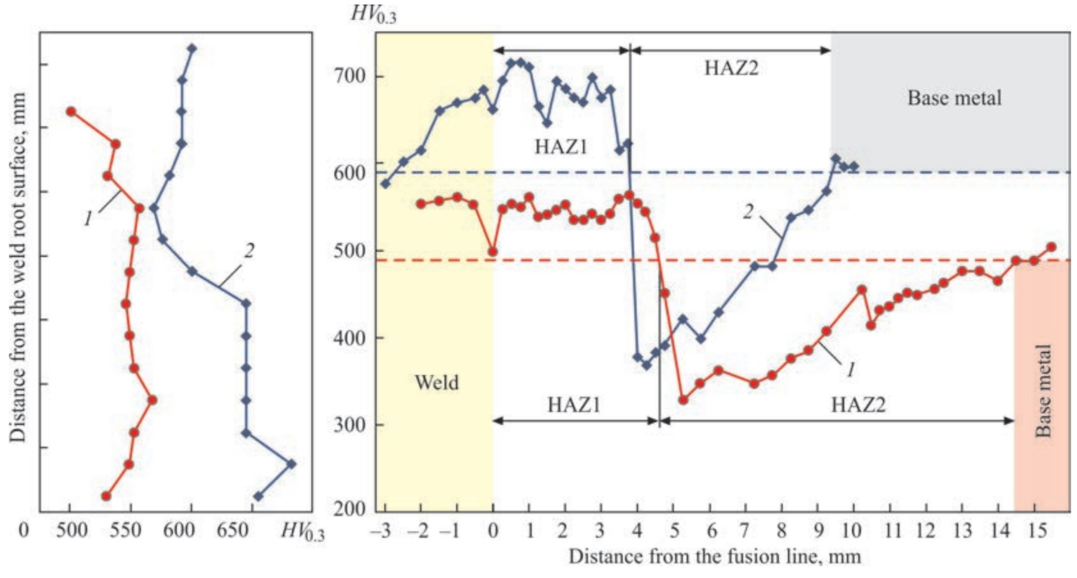

Figure 2. Microhardness distribution along the vertical axes of the welds and in the cross-section of the welded joints: *1* — Armox 500T steel; *2* — Mars 600 steel

steels shows that the extent of the HAZ in the joint of Armox 500T steel turned out to be markedly greater, first of all, due to its wider softened HAZ2 region. In the sample from Armox 500T steel in the vertical (y) measurement direction a noticeable microhardness reduction in the upper quarter of the weld is also observed, which is due to an increase in the deposited metal proportion in it. Microhardness distribution by the height of the weld formed during welding of a sample from Mars 600 steel allows outlining three regions: 1) near the weld root, ~3 mm high, with the highest hardness; 2) middle one, ~2 mm high, within which a gradual hardness reduction takes place; 3) upper one, ~2 mm high, with an intermediate microhardness value, compared to the two other regions.

Considering that for joints of both the steels the values of specific heat input are practically the same: $Q/\delta \approx 0.16$ kJ·mm^{-2} (where δ is the base metal thickness), as well as due to the remoteness of the softened HAZ2 regions from the area of the metallurgical reactions with the welding consumables, the causes for greater extent of the HAZ in the welded joint of Armox 500T steel can only be attributed to differences in alloying and technologies of thermomechanical treatment of the studied steels. Metallographic studies of the base metal microstructure demonstrated the troostite-martensitic structure of the sample from Armox 500T steel (Figure 3, *a*), whereas Mars 600 steel has the structure of fine-acicular lath martensite (Figure 3, *b*). It is also worth noting the presence of bands with different etchability across the thickness of the rolled stock of both the steels. By the data of [23] for rolled steel armor Armox 500T these features of the structure state are associated not with the chemical heterogeneity of the material, but with the biomodal nature of distribution of the size of primary austenite grains formed during hot rolling. Higher etchability bands coincide with the location of fine grains of former austenite, and they look darker than the light-coloured bands of metal with coarser primary grain.

Comparison of chemical composition of the studied steels (Table 1) shows that while in Armox 500T silicon is a deoxidizer, Mars 600 steel is alloyed with this element. Considering that silicon in the martensite solid

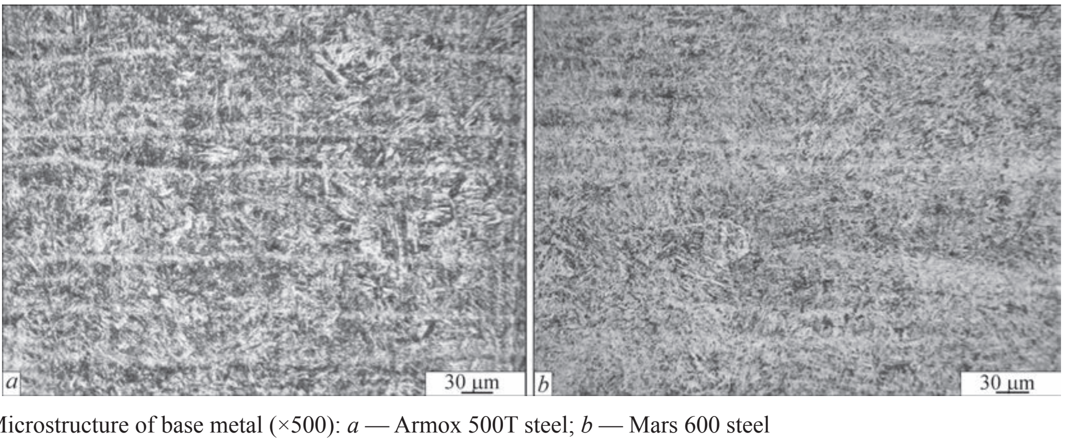

Figure 3. Microstructure of base metal (×500): *a* — Armox 500T steel; *b* — Mars 600 steel

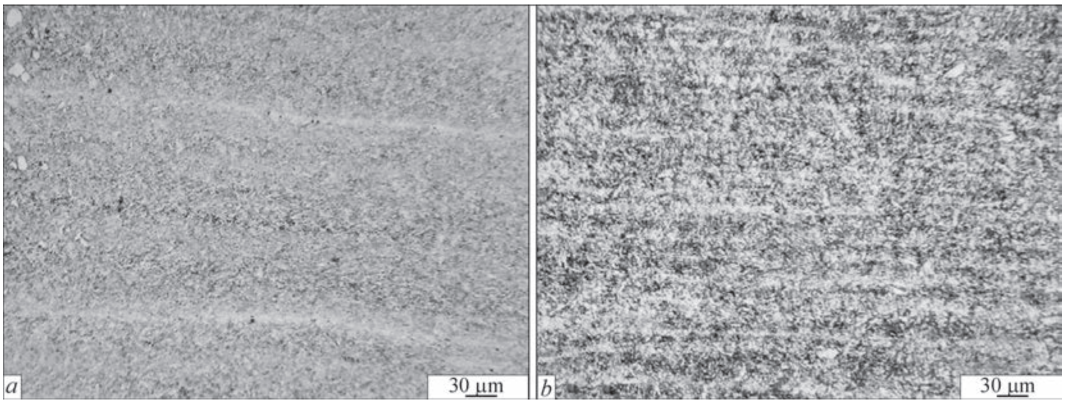

Figure 4. Microstructure of the high-tempered HAZ region (×500): *a* — Armox 500T steel; *b* — Mars 600 steel

solution slows down the diffusion mobility of carbon in the crystalline lattice, and inhibits carbide nucleation at the initial tempering stages [24, 25], short-term heating of the welding HAZ portion of Mars 600 steel, the most remote from the weld, to low-tempering temperatures did not lead to any significant changes in its structural state or hardness. As a result, the width of the softened region (HAZ2) of the welded sample of this steel turned out to be smaller, and the visible changes in its structure compared to the base metal were observed only for the metal which was heated to the high-tempering temperatures. Figure 4 is a comparison of the microstructure in high-tempered regions of the HAZ of the produced welded joints. In the Armox 500T steel sample the primary structure bimodal in terms of the primary grain size distribution was transformed into tempered troostite along the higher etchability band and recrystallized granular ferrite along the light etching bands (Figure 4, *a*). The metal structure in the high-tempered region of the sample from Mars 600 steel is more homogeneous and it consists of just tempered troostite (Figure 4, *b*).

Metallographic investigations of the welded sample from Armox 500T steel did not reveal any noticeable differences in the microstructure in different weld metal regions. Intensive mixing of the base, filler and insert materials led to formation of microregions of different etchability through the entire volume of the weld with different concentration of alloying elements (Figure 5, *a*). However, standard optical metallography methods did not allow revealing any morphological signs of primary structure recrystallization products. Contrarily, the results of studying the Mars 600

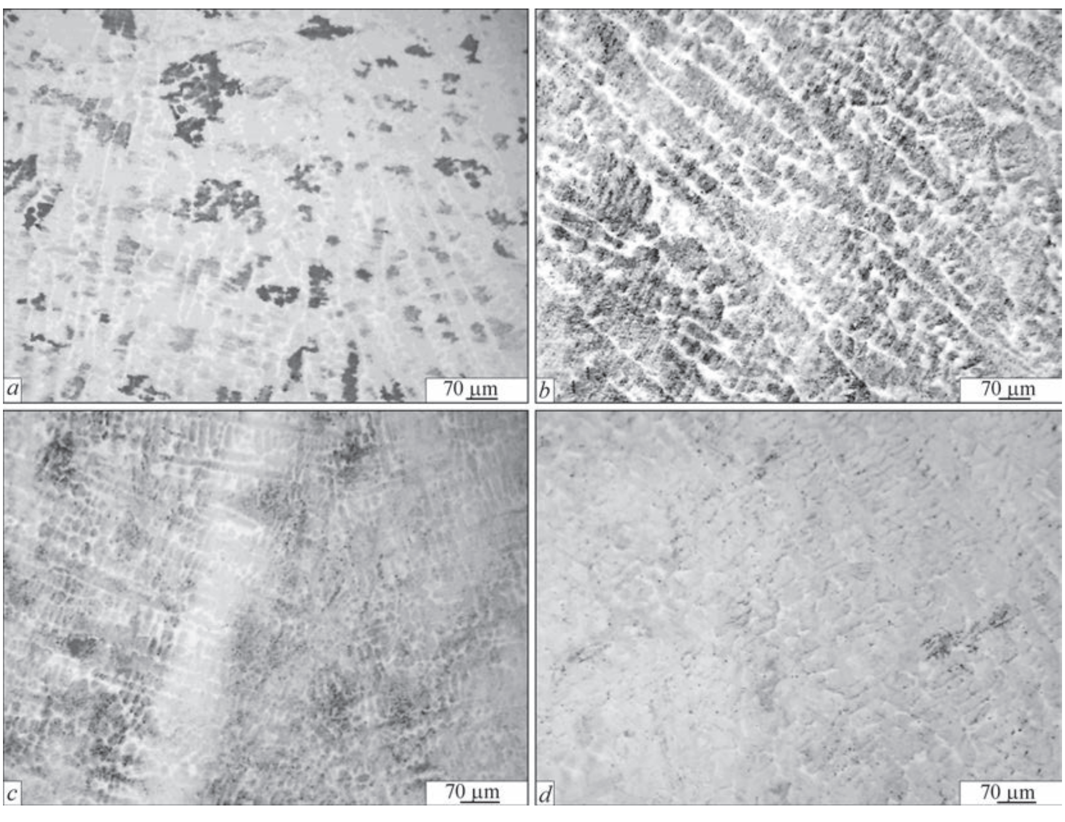

Figure 5. Microstructure of weld metal of the welded joints (×200): Armox 500T steel (*a*) and Mars 600 steel — root region (*b*), middle region (*c*), upper region (*d*)

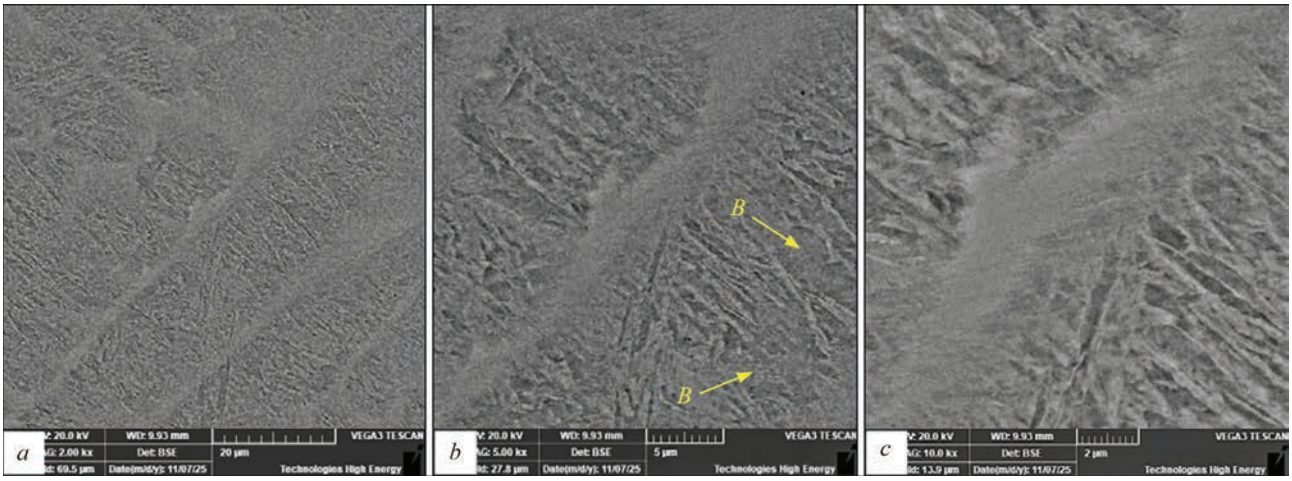

Figure 6. Microstructure of weld metal of Armox 500T steel sample: ×2000 (*a*); ×5000 (*b*); ×10000 (*c*). B — bainite of block morphology

steel sample point to formation of a heterogeneous (at the macrolevel) structure of the weld, which correlates with the determined microhardness distribution along its vertical axis (Figure 2). Lath martensitic structure was detected inside the crystallites of the weld metal root area (Figure 5, *b*). Within the middle weld region along the height, which features a reduction of microhardness, optical microscopy did not detect any martensite packets, but light-etching bands appeared (Figure 5, *c*). The upper region of the weld, where the metal has somewhat higher microhardness values, looks like a solid "white layer", where just the dendritic crystallite boundaries are etched (Figure 5, *d*).

The features of structure formation in the weld determined for Mars 600 steel sample are due to its more intensive alloying by welding consumables, compared to the weld on Armox 500T steel sample, owing to a higher filler wire feed rate, larger diameter of the insert rod and lower welding speed.

Scanning electron microscopy revealed the martensitic-bainitic structure of the weld metal of the welded sample from Armox 500T steel. Lath martensite packets (Figure 6, *a*, *c*), as well as bainitic structure blocks (Figure 6, *b*), are present within the individual branches of the columnar crystallites. Their formation is caused by the concentration heterogeneity of the alloying element distribution in the weld metal. The average width of the columnar crystallites is equal to 13–22 μm.

The structure of cast metal in the root area of the weld of Mars 600 steel welded sample is homogeneous, fine-acicular martensitic (Figure 7, *a*–*c*). The average width of the columnar crystallites reaches 14–30 μm. Contrarily, the metal of the weld upper region has a much finer primary structure with the crystallite width of 5–12 μm (Figure 7, *d*–*f*), which is, obviously, due to the features of the influence of the pulsating constricted arc on the weld pool solidification conditions, simultaneously alloyed by the filler and insert wires. No acicular or packet structure of classical martensite was found inside the dendrite cells even with the magnification of ×10000 (Figure 7, *e*).

The high microhardness of ~580–600 $HV_{0.3}$ in the metal of the weld upper region determined in the Mars 600 steel sample (Figure 2) and the results of microstructural studies (Figure 5, *d*; Figure 7, *f*) are indicative of formation in this part of the weld of the so-called structureless martensite (hardenite) — a nanocrystalline mixture of martensite and residual austenite. The **"**white layer**"** of structureless martensite, created by the methods of hardening treatment of the surface of the engineering and tool steels [26, 27], as well as heterogeneous steel armor [28], is characterized by a high hardness and friction and wear resistance. Refinement of the dendritic structure in the weld upper region due to intensive mixing of the pool melt, with further overcooling below M_s temperature promoted blocking of martensite crystals growth by the boundaries of highly refined austenite grains, that, according to the classical concepts [29], is the necessary precondition of structureless martensite formation.

Results of studying the chemical composition of weld regions in joints of Armox 500T and Mars 600 steels are given in Table 3. Considering the high error of EDX-determination of carbon concentration, its average content in the metal of both the welds was determined additionally by the method of NDIR-spectroscopy. One can see from the data in Table 3 that the average carbon content in the weld metal of Armox 500T steel sample almost did not decrease compared to its content in the base metal (Table 1). At the same time, the average carbon content in the weld metal of the Mars 600 steel sample was reduced by ~25 % compared with the base metal. For welds of the joints of both the steels, there is a tendency toward a reduction of the content of all the alloying elements alongside an increase in the carbon concentration in the weld root

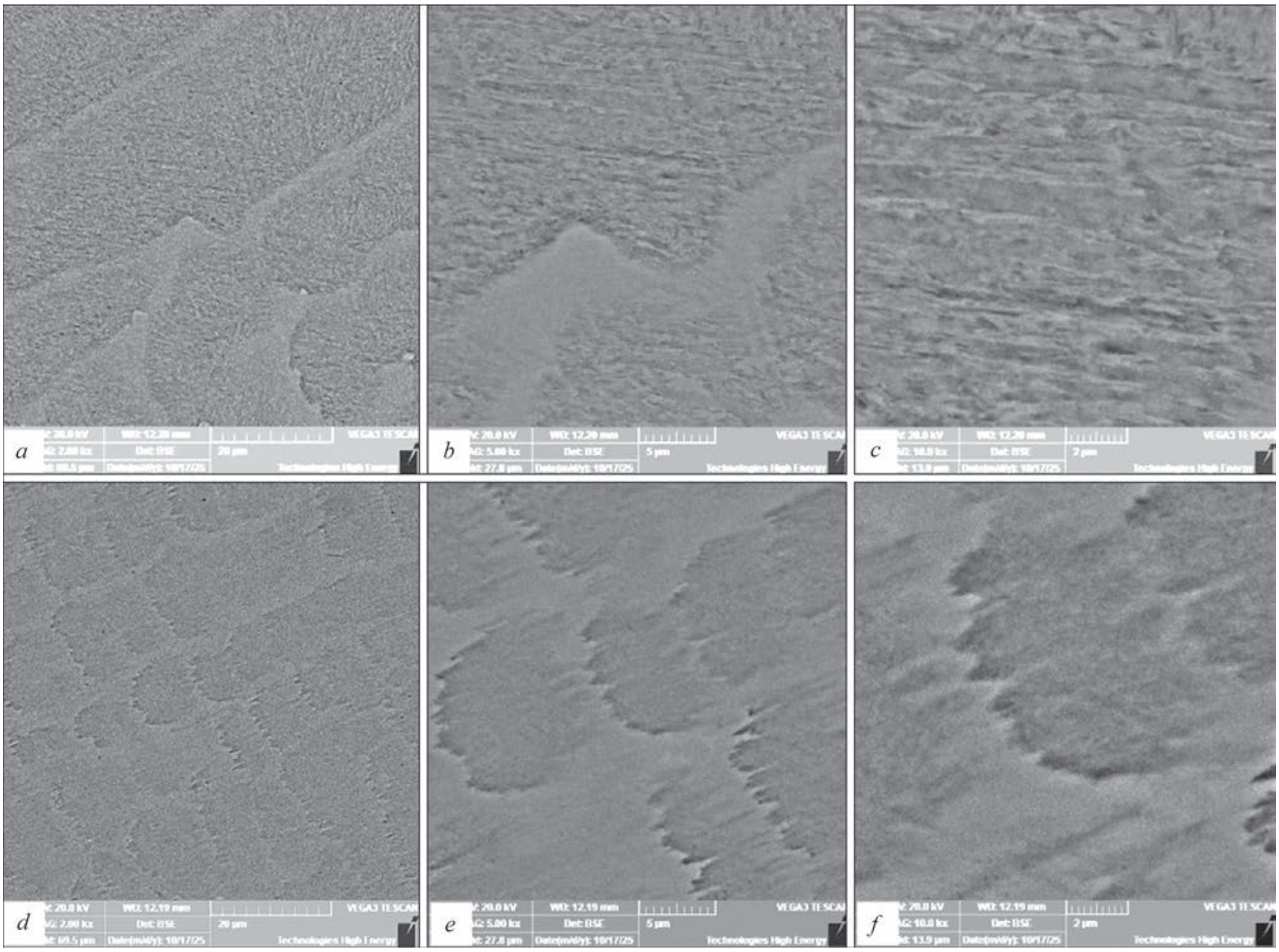

Figure 7. Microstructure of the root (*a–b*) and upper (*d–f*) regions of weld metal of Mars 600 steel sample: ×2000 (*a*, *d*); ×5000 (*b*, *e*); ×10000 (*c*, *f*)

regions, compared with the upper regions, despite the near-root position of the low-carbon high-alloy insert material. This effect is attributable to the features of the pulsating constricted arc influence on the hydrodynamic and convective fluxes in the pool melt.

Despite the presence of signs of structureless martensite in the metal of upper region of the weld on the Mars 600 steel, it is somewhat inferior to the hardness values for the root region metal (Figure 2), because of the significantly lower carbon content. Moreover, this is the only region of all the studied regions of both the welds, where the total alloying element content meets the criteria for high-alloy steel (>10 wt.%).

Results of ballistic tests of the welded samples are given in Figure 8. According to the test protocol, a sample from Armox 500T steel 5.4 mm thick has passed ballistic tests for resistance to fire from a 5.45×39 mm 7N6M assault rifle cartridge with a PS bullet (a bul-

Table 3. Chemical composition of weld metal of the studied welded joints, wt.%

Method of analysis	Element	Armox 500T		Mars 600		
		Weld region		Weld region		
		Top	Root	Top	Middle	Root
EDX	C	6.04*	6.54*	6.81*	7.60*	8.42*
	Si	0.26	0.20	0.65	0.62	0.58
	Mn	1.60	1.49	1.81	1.30	1.20
	Cr	4.56	2.96	5.10	3.79	3.63
	Ni	1.94	1.79	3.30	2.88	2.69
	Mo	0.28	0.26	0.24	0.20	0.21
NDIR	C	0.27		0.32		

*Due to the high measurement error, the carbon content values determined by the method of energy-dispersive X-ray spectroscopy, are given only for comparative analysis.

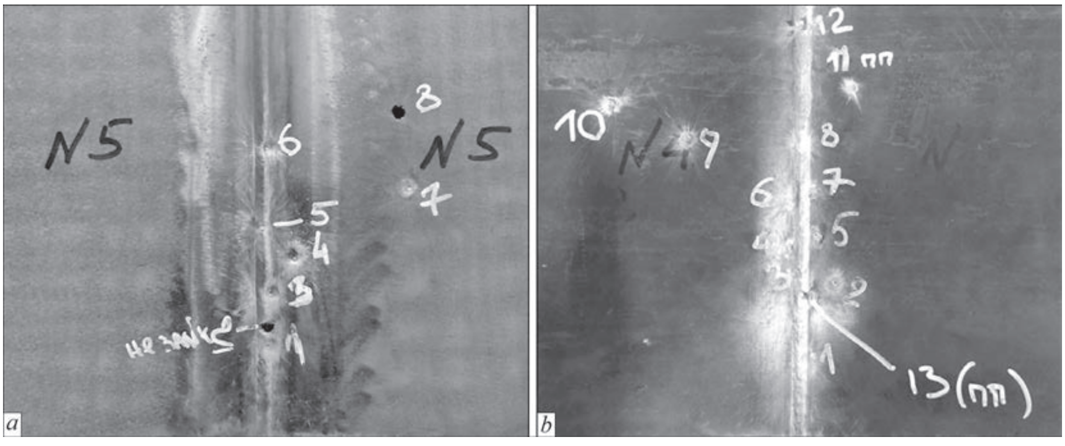

Figure 8. Appearance of welded samples after ballistic testing: *a* — Armox 500T steel; *b* — Mars 600 steel

let with a hardened steel core in a steel jacket), which is defined as protection class PZSA-3, according to DSTU 3975–2000. Shooting of the sample using the 7N10 cartridge with a PP bullet (an enhanced-penetration bullet with a hardened steel core in a steel jacket) caused complete penetration (Figure 8, *a*) both in the weld metal (hit No. 2, "fail") and in the base metal unaffected by the welding thermal cycle (hit No. 8).

A welded sample made of Mars 600 steel 6.2 mm thick, successfully withstood ballistic testing for resistance to impacts from both types of ammunition (Figure 8, *b*): the PS bullet (hits Nos 1–9), as well as the PP bullet (hits Nos 10–13), which meets the requirements of the PZSA-4 protection class in accordance with the DSTU 3975-2000 standard.

DISCUSSION OF RESULTS

Obtained results show that application of pulsed-plasma welding with combined alloying of the weld metal allows realizing an approach to armor steel welding with application of high-alloy austenitic filler materials, which differs significantly from the traditional technologies of mechanized arc welding. The latter are characterized by formation of an austenitic or austenitic-ferritic weld metal with the hardness level lower than that of the base metal, which is often regarded as one of the factors reducing the local ballistic resistance of armor steel welded joints.

In the studied joints a different approach to formation of the weld metal structure and properties is realized. Martensitic-type structures form in the weld metal, despite the application of high-alloy welding consumables of austenitic class. This is indicative of the important role of the base metal in formation of the weld structure and confirms the effectiveness of combined alloying application under the conditions of a high proportion of the base metal in the weld metal.

Comparison of the results for Armox 500T and Mars 600 steels showed that the pattern of structure formation is determined not only by the welding conditions, but also by the features of armor steel chemical composition. A higher carbon and silicon content in Mars 600 steel favours the formation of finer martensitic structures and improves the metal resistance to the tempering processes in the HAZ. This is in agreement with the microhardness measurement results and the determined reduction in the width of the HAZ softened zone, compared to Armox 500T steel.

One of the key features of the applied technology is application of the pulsed mode of plasma welding. It is known that the periodical change in the plasma arc current is accompanied by a change in the current density, electromagnetic forces, degree of the arc constriction, and pressure of the plasma flux on the melt surface, which results in appearance of the nonstationary convective fluxes in the weld pool and intensification of mass transfer in the melt [14–16].

In keeping with the data of [14], the surface tension forces, electromagnetic forces, plasma flux and buoyancy forces have the decisive influence on the metal flow in plasma welding. When operating in the pulsed mode, the above factors act in the nonstationary mode, leading to a periodical disturbance of the melt and intensification of the mass transfer processes. Similar tendencies as to the influence of the pulsed arc on weld formation, structure refinement and increase of the metal homogeneity were also established in [13, 15, 16].

Taking into account the derived results, it can be assumed that the determined features of alloying element and carbon distribution along the weld height, as well as formation of a heterogeneous weld metal structure are the result of the combined action of alloying and intensive stirring of the weld pool metal. The periodical change in the pressure of the plasma flux and the electromagnetic forces may promote a more effective interaction of the base metal with the filler wire and the insert rod, creating the conditions for formation of a gradient distribution of the chemical elements in the weld metal.

An important feature of the obtained results is the fact that the high ballistic resistance of the welded joints is achieved not due to the local strengthening of individual regions, but as a result of formation of a more balanced structural and mechanical state of the welded joint as a whole. Formation of high-strength weld metal of martensitic type in a combination with the restricted width of the softened HAZ regions allows avoiding an abrupt mismatch in the properties between the individual joint zones, which is one of the key factors for ensuring the ballistic resistance at the base metal level.

Thus, investigation results indicate that application of pulsed-plasma welding with combined alloying of the weld metal creates the conditions for formation of a martensitic-type weld metal with the ballistic resistance level equivalent to that of the base metal in the heat-hardened condition. Achievement of such a result is due to the combined action of the high proportion of the base metal in the weld metal, combined alloying with filler wire and insert rod of austenitic class, as well as the features of the hydrodynamic processes in the weld pool in the pulse mode of plasma welding. It is probable that the periodical action of the pulsating constricted plasma arc promotes an intensification of mass transfer and mixing of the melt, creating additional preconditions for formation of the established structural state of the weld metal [14–16].

CONCLUSIONS

1. It is shown that pulsed-plasma welding with independent regulation of the heat input and filler metal quantity ensures formation of full-penetration butt joints of Armox 500T and Mars 600 armor steels 5–6 mm thick without edge preparation at the specific heat input of $Q/\delta \approx 0.16$ kJ/mm^2. At the same level of thermal impact, Mars 600 steel features a smaller width of the HAZ softened region, compared with Armox 500T steel, which is associated with an increased silicon content and higher resistance of its martensitic structure to short-time tempering.

2. It was determined that combined alloying of the weld metal with OK Autrod 16.95 filler wire and OK Tigrod 308L insert rod in combination with a high proportion of the base metal in the weld allows avoiding the formation of a soft austenitic weld metal, characteristic for the traditional MAG-welding of armor steels. A martensitic-bainitic structure of the weld metal forms in the joints of Armox 500T steel with a hardness, which is not inferior to base metal hardness.

3. For Mars 600 steel a pronounced structural anisotropy of the weld metal along its height was found. In the root region a fine-acicular martensite with the highest microhardness value is formed, in the middle part — a structure with lower hardness values, and in the upper region — a refined structure with the signs of structureless martensite. The derived results are indicative of a significant influence of the solidification conditions and alloying element distribution on the weld metal structure formation.

4. It is shown that application of the pulsed mode of plasma welding is one of the important features of the used technology. Taking into account the results of structural and chemical studies it can be assumed that the periodical action of the pulsating constricted plasma arc promotes an intensification of mass transfer and mixing of the weld pool metal, creating additional prerequisites for formation of a graded distribution of alloying elements and carbon along the weld height.

5. Ballistic testing confirmed that the developed technology of plasma-arc welding with combined alloying of the weld metal ensures producing welded joints of armor steels of different hardness classes, with ballistic resistance equivalent to that of the base metal. For samples from Mars 600 steel, resistance to impacts from PS and PP bullets is ensured, whereas for Armox 500T it has been established that destruction is determined by the bullet resistance level of the base metal under stricter testing conditions, rather than by the properties of the weld.

REFERENCES

1. DSTU V 9014:2020: *Arc welding of high-hardness steel structures for light armored vehicles. Technical specifications*. Kyiv, SE “UkrNDNTs” [in Ukrainian].
2. Men, I., Naroditsky, D. (2023) Vibration fatigue testing procedure of high strength MARS 600 steel fillet welds using stainless steel consumable electrode. *Advanced Engineering Forum,* **49**, 57–78. DOI: https://doi.org/10.4028/p-o0a804
3. Gaivoronskyi, O.A., Poznyakov, V.D., Zavdoveyev, A.V. et al. (2023) Prevention of cold cracking in armour steel welding. *The Paton Welding J.*, **5**, 3–10. DOI: https://doi.org/10.37434/tpwj2023.05.01
4. Çoban, O., Kaymak, F., Gürol, U. et al. (2025) Characterization of fillet welded armor steel performed by robotic gas metal arc welding: effect of heat input on microstructure and microhardness. *J. of Mater. Eng. and Perform.*, **34**, 231–244. DOI: https://doi.org/10.1007/s11665-023-09058-y
5. Slyvinskyy, O.A., Kvasnytskyi, V.V., Prokhorenko, O.V. et al. (2025) The influence of low-temperature austenite transformation in weld metal on the residual stress state of welded joints of armor steel. *Metallofiz. Noveishie Tekhnol.*, **47**, 1295–1318 [in Ukrainian]. DOI: https://doi.org/10.15407/mfint.47.12.1295
6. Madhusudhan Reddy, G., Mohandas, T., Papukutty, K.K. (1998) Effect of welding process on the ballistic performance of high-strength low-alloy steel weldments. *J. Mater. Process Tech.*, 74(**1–3**), 27–35. DOI: https://doi.org/10.1016/S0924-0136(97)00245-8
7. Slyvinskyy, O.A., Kovtoniuk, M.M. (2025) Approaches to enhancing the ballistic performance of welded joints in high and ultra-high hardness armor steels (Review). *The Paton Welding J.*, **12**, 11–19. DOI: https://doi.org/10.37434/tpwj2025.12.02
8. Morsy, M.A., Abdel Aziz, S.M., Abdelwahed, K. et al. (2022) Effect of welding parameters on the mechanical and metallur-

gical properties of armor steel weldment. *J. Eng. Appl. Sci.*, **69**, 62. DOI: https://doi.org/10.1186/s44147-022-00102-7
9. Sowards, J.W., Hussey, D.S., Jacobson, D.L. et al. (2018) Correlation of neutron-based strain imaging and mechanical behavior of armor steel welds produced with the hybrid laser arc welding process. *J. Res. Natl. Inst. Stand. Technol.*, **123**, 123011. DOI: https://doi.org/10.6028/jres.123.011
10. Günena, A., Bayara, S., Karakaş, M.S. (2020) Effect of different arc welding processes on the metallurgical and mechanical properties of Ramor 500 armor steel. *J. Eng. Mater. Technol.*, **142**, 021007. DOI: https://doi.org/10.1115/1.4045569
11. Skowrońska, B., Szulc, J., Bober, M. et al. (2022) Selected properties of Ramor 500 steel welded joints by hybrid PTA-MAG. *J. Adv. Join. Proces.*, **5**, 100111. DOI: https://doi.org/10.1016/j.jajp.2022.100111
12. Son, H.J., Jeong, Y.C., Seo, B.W. et al. (2023) Weld quality analysis of high-hardness armored steel in pulsed gas metal arc welding. *Metals*, 13(**2**), 303. DOI: https://doi.org/10.3390/met13020303
13. Sathish Kumar, K., Arivazhagan, N. (2024) An innovative pulsed current arc welding technology for armor steel: Processes, microstructure and mechanical properties. *Mater. Today Commun*., **38**, 108237. DOI: https://doi.org/10.1016/j.mtcomm.2024.108237
14. Ngo Huu, M., Nguyen Van, A., Nguyen Van, T. et al. (2020) Material flow behavior on weld pool surface in plasma arc welding process considering dominant driving forces. *Appl. Sci.*, 10(**10**), 3569. DOI: https://doi.org/10.3390/app10103569
15. Lu, Z., Zhang, W., Jiang, F. et al. (2019). A primary study of variable polarity plasma arc welding using a pulsed plasma gas. *Materials*, 12(**10**), 1666. DOI: https://doi.org/10.3390/ma12101666
16. Wang, Z., Jiang, D., Wu, J., Xu, M. (2020) A review on high-frequency pulsed arc welding. *J. Manuf. Process*., **60**, 503–519. DOI: https://doi.org/10.1016/j.jmapro.2020.10.054
17. (2008) MIL-DTL-46100E (MR) with Amendment 1. *Armor plate, steel, wrought, high hardness.* U.S. Detail Specification. Aberdeen, U.S. Army Research Laboratory.
18. MIL-DTL-32332A (MR). *Armor plate, steel, wrought, ultra-high hardness* (2018) U.S. Detail Specification. Aberdeen, U.S. Army Research Laboratory.
19. Khoshnaw, F., Krivtsun, I., Korzhyk, V. (2023) Chapter 2. Arc welding methods. In: *Welding of metallic materials: Methods, metallurgy and performance.* Ed. by F. Khoshnaw. Amsterdam, Elsevier, 37–71. DOI: https://doi.org/10.1016/B978-0-323-90552-7.00004-3
20. Sydorets, V., Korzhyk, V., Khaskin, V. et al. (2017) Electrical characteristics of the equipment for the hybrid plasma-MIG welding. In: *Proc. of the IEEE 58th Inter. Scientific Conf. on Power and Electrical Engineering of Riga Technical University (RTUCON), Riga, Latvia*, 1–6. DOI: https://doi.org/10.1109/RTUCON.2017.8124811
21. Kvasnytskyi, V., Korzhyk, V., Lahodzinskyi, I. et al. (2020) Creation of volumetric products using additive arc cladding with compact and powder filler materials. In: *Proc. of IEEE 10th Inter. Conf. Nanomaterials: Applications & Properties (NAP), Sumy, Ukraine,* 02SAMA16-1–02SAMA16-5. DOI: https://doi.org/10.1109/NAP51477.2020.9309696
22. Shevchenko, V., Korzhyk, V., Gao, S. et al. (2024) Formation of stainless steel welded joints produced with the application of laser and plasma energy sources. *Metals*, 14(**6**), 706. DOI: https://doi.org/10.3390/met14060706
23. Garasym, Ju. A., Bondarevska, N.O., Teliovich, R.V. et al. (2021) Influence of high-speed heat-setting on armor resistance of high-strength sheet metal of protective purpose. *Metallofiz. Noveishie Tekhnol.*, **43**, 1235–1246 [in Ukrainian]. DOI: https://doi.org/10.15407/mfint.43.09.1235
24. Wang, Lj., Cai, Qw., Wu, Hb. et al. (2011) Effects of Si on the stability of retained austenite and temper embrittlement of ultrahigh strength steels. *Inter. J. Miner. Metall. Mater.*, **18**, 543–550. DOI: https://doi.org/10.1007/s12613-011-0475-0
25. Kim, B., Celada, C., San Martín, D. et al. (2013) The effect of silicon on the nanoprecipitation of cementite. *Acta Mater.*, **61**, 6983–6992. DOI: https://doi.org/10.1016/j.actamat.2013.08.012
26. Kozechko, V.A., Kozechko, V.I. (2024) Combined ultrasonic-mechanical treatment. *Metallofiz. Noveishie Tekhnol.*, **46**, 851–860. DOI: https://doi.org/10.15407/mfint.46.09.0851
27. Kolisnichenko, O.V., Korzhyk, V.M., Senderowski, C. et al. (2025) Influence of pulse plasma treatment on wear resistance of 40Kh steel surface layers. *The Paton Welding J.*, **9**, 39–45. DOI: https://doi.org/10.37434/tpwj2025.09.05
28. Bolotsky, M. (1945) *Armor-rolled: Metallurgical examination of British homogenous and face hardened armor*. Technical report WAL 710/724. Watertown Arsenal Laboratory.
29. Zav'yalov, A.S., Teplukhin, G.N., Gabeev, K.V. (1979) Conditions and mechanism of formation of structureless martensite (hardenite). *Met. Sci. Heat Treat*., **21**, 750–752. DOI: https://doi.org/10.1007/BF00708376

ORCID

O.A. Slyvinskyy: 0000-0001-6418-4898,
V.D. Poznyakov: 0000-0001-8581-3526,
V.M. Korzhyk: 0000-0001-9106-8593,
Ye.V. Illiashenko: 0000-0001-9876-0320,
S.P. Bisyk: 0000-0002-5009-2113

CONFLICT OF INTEREST

The Authors declare no conflict of interest

CORRESPONDING AUTHOR

O.A. Slyvinskyy
[1]National Technical University of Ukraine
"Igor Sikorsky Kyiv Polytechnic Institute"
37 Prosp. Beresteiskyi, 03056, Kyiv, Ukraine.
[2]E.O. Paton Electric Welding Institute of the NASU
11 Kazymyr Malevych Str., 03150, Kyiv, Ukraine
E-mail: o.slyvinsky@gmail.com

SUGGESTED CITATION

O.A. Slyvinskyy, V.D. Poznyakov, V.M. Korzhyk, Ye.V. Illiashenko, S.P. Bisyk (2026) Features of formation of the structure and ballistic resistance of armor steel welded joints produced by pulsed plasma arc welding with combined alloying of the weld metal. *The Paton Welding J*., **08**, 3–12.
DOI: https://doi.org/10.37434/tpwj2026.08.01

JOURNAL HOME PAGE

https://patonpublishinghouse.com/eng/journals/tpwj

Received: 30.04.2026
Received in revised form: 16.06.2026
Accepted: 27.07.2026

DOI: https://doi.org/10.37434/tpwj2026.08.02

MICROSTRUCTURE AND PHASE COMPOSITION OF JOINTS OF CAST AND WROUGHT NICKEL SUPERALLOYS PRODUCED BY FRICTION WELDING

I.V. Ziakhor, A.M. Levchuk

E.O. Paton Electric Welding Institute of the NASU
11 Kazymyr Malevych Str., 03150, Kyiv, Ukraine

ABSTRACT

For domestic manufacturers of aviation gas turbine engines (GTEs), the development of efficient technologies for welding nickel superalloys remains an important challenge, particularly for friction welding of "disk–blade" (blisk-type) components. The paper presents the results of a study on the formation of dissimilar joints between the cast VZhL12U alloy and the wrought EI698VD alloy produced by friction welding. Experimental methods were used to investigate the influence of friction welding process parameters and postweld heat treatment (HT) conditions on the joint microstructure and the nickel morphology of strengthening phase particles, including carbides and the γ′-phase. The experiments were carried out on superalloy specimens with a diameter of 24 mm. A hybrid friction welding technology was applied with varying durations of rotation braking during the forging stage in the range of t_{br} = 0.3–3.0 s. It was established that an increase in t_{br} significantly affects structural and phase transformations in the thermomechanically affected zone (TMAZ) of the joints. In particular, at t_{br} = 3.0 s, both the secondary dispersed γ′-phase particles and the thermally stable primary eutectic γ'_{eut}-phase on the side of the cast VZhL12U alloy dissolved during the forging stage. A heat treatment mode was determined that ensures restoration of the γ′-phase particle morphology on the side of the EI698VD alloy and eliminates regions of reduced microhardness within the joint zone. The phenomenon of an anomalous coarsening of dispersed γ′-phase particles in the TMAZ of the VZhL12U alloy after a three-stage HT (according to the specifications for EI698VD alloy) was also observed.

KEYWORDS: nickel superalloys, friction welding, joints, microstructure, heat treatment, γ′-phase, carbides, microhardness

INTRODUCTION

The use of heat-resistant nickel superalloys ensures the necessary operational characteristics of critical parts in gas turbine engines (GTE) [1]. The use of welded assemblies in the design of aircraft GTEs necessitates the development of methods for high-quality welding of parts made from nickel superalloys.

Nickel superalloys are nickel-chromium-based γ-solid solution matrices alloyed with molybdenum, tungsten, and niobium [2–4]. The formation of the strengthening γ′-phase is mainly provided by aluminium, titanium, and tantalum. The microstructure, in particular, the size of structural elements, the morphology of the γ′-phase, and the MeC and $Me_{23}C_6$-type carbides determine the operational characteristics of nickel superalloys.

To produce permanent joints in nickel superalloys, fusion welding [5] and pressure welding [6–11] methods are used. The production of defect-free joints of nickel superalloys using fusion welding methods is not a significant problem for alloys with a total aluminium and titanium content not exceeding 4 wt.%. However, in more heavily alloyed nickel superalloys, welds are prone to cracking [12–14].

Friction welding (FW) in its various process variations — conventional, inertia, combined, orbital, and linear — is increasingly being used for the permanent joining of high-alloy nickel superalloys [15–21]. A number of publications present the results of studies on changes in the microstructural characteristics of nickel superalloy joints produced by inertia friction welding (IFW) [15–17].

The study [15] presents the results of a comparison of the microstructure, mechanical properties, and residual stresses in welded joints produced by IFW for three superalloys: forged Inconel 718, cast U720Li, and powder RR1000. It was found that, unlike the U720Li and RR1000 alloys, FW of the Inconel 718 alloy results in the formation of a region free of precipitates of the strengthening γ′-phase, which causes a significant decrease in hardness near the joint line. To improve the level of mechanical properties of the joints and reduce welding stresses, postweld heat treatment (HT) was performed — either complete (in accordance with the technical requirements for the specific alloy) or partial (corresponding to one of the stages of the complete HT of the alloy). In the latter case, this ensures a certain reduction in welding stresses (to a level that is safe in terms of operational reliability), partial restoration of the microstructure and morphology of the strengthening phases in the joint zone.

In [16], the structure of dissimilar joints between the nickel superalloys U720Li and IN718, produced by IFW, was investigated. The study was conducted on joints in both as-welded and postweld heat-treated (HT) conditions. The results showed that IFW enables the production of dissimilar joints between the U720Li and IN718 alloys without micropores or microcracks, as well as without significant migration of chemical elements across the joint line. However, significant changes in the microstructure and distribution of strengthening phase particles were observed on both sides of the joint line. The 720Li alloy, with a high volume fraction of the γ′-phase ($Ni_3(Al,Ti)$), exhibits a wider heat-affected zone unlike the IN718 alloy, which is strengthened primarily by the γ″-phase (Ni_3Nb). It was found that the U720Li alloy exhibits a slight decrease in hardness near the joint line in the state after IFW, which is caused by the depletion of the γ′-phase, whereas the IN718 alloy is characterized by the presence of a region free of γ″-phase precipitates. A comparison of the joints in their state after IFW and HT, intended to relieve stresses, shows that the IN718 alloy remains in an overaged condition after heat treatment. In the U720Li alloy, the hardness distribution is mainly determined by the distribution of the tertiary and reprecipitated γ′-phase, while the γ″-phase in the alloy completely dissolved during the IFW process and did not reprecipitate during cooling.

The study in [17] investigated the effect of the IFW process parameters for nickel superalloys on the temperature in the contact zone and the solidification process of the billets. It was established that mechanical energy depends primarily on the initial rotational speed, and a relatively high axial pressure increases the efficiency of converting mechanical energy into effective welding heat. The influence of axial pressure, initial rotational speed, and the flywheel's moment of inertia on the penetration depth was determined, and the technological principles for optimizing IFW parameters were established, taking into account changes in temperature profiles. The results show that axial pressure has a more pronounced effect on the width of the high-temperature zone than rotational speed during the final stage (rapid upsetting) of the IFW process.

The results of microstructural examinations of the RR1000 powder superalloy during IFW are presented in [18]. Significant microstructural changes were observed within 2 mm from the joint line (JL). In this region, the hardness profile is influenced by changes in grain size, volume fraction, and particle size of the γ′-phase. At greater distances from the JL, only negligible microstructural changes are observed, but variations in hardness do occur. In [19], the fatigue strength of FW joints made of Inconel 718 and Mar-M247 alloys was investigated. It was found that fracture occurs on the Mar-M247 alloy side outside the JL. Based on the results of studies on the weldability of five different nickel superalloys [20], it was determined that to produce high-strength joints, the FW process parameters must ensure a high upsetting rate of the billets at a relatively low temperature in the contact zone.

Research results on the linear FW of the IN738 and CMSX486 alloys [21] revealed the presence of alloying element liquation and the formation of continuous oxide films in the joint zone, which negatively affects the mechanical properties of welded joints. Gleeble thermomechanical simulation showed that oxides form as a result of local oxidation of liquid-state regions that form on the contacting surfaces of the alloys.

The available literature lacks sufficient information on joint formation in nickel superalloys used in the construction of domestically produced aviation GTEs. In [22], an assessment was conducted of the thermal-deformation conditions for the joint formation in the EI698VD alloy during FW. Calculations established that the EI698VD alloy can reach the melting temperature in the contact zone at the heating stage. The ways to optimize the FW technology for the EI698VD alloy and methods for minimizing the width of the phase transformation zone in the joints were proposed. The results of studies on the heating, deformation, and microstructural formation processes in FW of the EP741NP and VZhL12U alloys are presented in [23]. The minimum pressure values required to ensure the upsetting of the billets and the range of heat treatment parameters within which defect-free joints can be formed were determined.

The SE "Ivchenko-Progress" and PJSC "Motor Sich" took on a relevant task of developing an effective technology for pressure butt welding of cast blades made of the VZhL12U alloy to a forged disk made of the EI698VD (KhN73MBTYu-VD) alloy. The importance of producing welded bladed disks for domestic GTEs necessitates comprehensive research to address this challenge. Issues that have not been sufficiently studied include determining the regularities of microstructure formation and phase composition in joints between the VZhL12U and EI698VD alloys, as well as determining the effect of the technological parameters of the FW process and the postweld heat treatment (HT) mode on changes in the microstructure, morphology of strengthening phases, hardness values, and mechanical properties of the joints.

AIM OF THE WORK

The study is aimed at identifying the regularities of microstructure formation in the joints of the cast VZhL12U and forged EI698VD nickel superalloys, produced by FW under various process parameters, determining the characteristics of microstructural and phase transformations in the joints under various postweld heat treatment (HT) modes for the development of an effective FW technology for bladed disks of GTEs.

RESEARCH OBJECT

The research is focused on the formation of permanent joints in cast and forged nickel super alloys during FW.

Table 1. Chemical composition of the alloys under study, wt.%

Alloy	Ni	Cr	Ti	Al	W	Mo	Nb	Co	V	Mn	Si	Hf	C
EI698VD	Base	14.4	2.74	1.69	0.05	2.98	2.04	–	0.05	0.08	0.20	–	0.05
VZhL12U		9.7	4.5	5.4	1.4	3.1	0.8	14.0	0.8	0.01	0.03	–	0.18

Table 2. Phase characteristics of the alloys under study [21, 22]

Alloy	Total γ′-phase content, %	Solidus temperature, $T_{solidus}$	Temperature limit of dissolving the γ′-phase, T_{solvus}, °C	Recrystallization temperature, T_{recr}, °C	Deformation temperature		Hot plastic deformation capacity
					Start	End	
EI698VD	25.0	1320	1030	1050–1100	1160	1000	Good
VZhL12U	65.0	1273	1220	–	–	–	Very poor

SUBJECT OF RESEARCH

The research examines macrostructure, microstructure, and microhardness in the joint zone of the VZhL12U cast alloy and the EI698VD forged alloy, produced by FW with controlled rotational braking.

RESEARCH METHODOLOGY

Experimental studies on FW were conducted on the VZhL12U and EI698VD alloy specimens with a diameter of 24 mm. The chemical composition and phase characteristics of the alloys are given in Tables 1 and 2.

The EI698VD alloy specimens after a three-stage HT are delivered meeting the following technical specifications: first stage — quenching at 1100 °C, holding for 8 h, second stage — hardening from 1000 °C, holding for 4 h; third stage — aging at 775 °C, holding for 16 h. In all cases, cooling in air is performed. The VZhL12U alloy specimens are delivered as cast, without homogenization.

The experimental welding was performed in the MST2001 laboratory machine [24]. The machine's hydraulic drive provides a three-stage cycle pattern for applying axial force — conditioning, heating, and forging in the range of 10–200 kN. After the modernization of the braking system, the MST2001 machine enables the implementation of combined FW technology with controlled rotational braking (Figure 1). During the experiments, the FW process parameters were set within the following ranges: circumferential speed — V = 1 m/s, heating pressure — P_h = 100–200 MPa, forging pressure — P_f = 200–400 MPa, heating time — t_h = 10–30 s, forging time — t_f = 10 s, rotational braking time — t_{br} = 0.3–3.0 s.

The FW mode parameters were recorded by a PC-based operating system using an ADZ-SML-20.0-1 pressure sensor and an SR18-25-S Megatron upsetting sensor. Mechanical tensile tests of welded joint specimens were performed using a TsDM-10 testing machine. The presence of surface defects (cracks, delamination) in the joint area was determined by visual inspection of the joint surface at ×10 magnification, as well as using an MMR4 microscope. The geometry of the welded joints and the presence of defects were determined by macro- and microscopic examination of polished sections. Optical and electron microscopy were performed on sections prepared using chemical and electrolytic methods for structural characterization, as well as ion polishing and etching in a JEOL JFC-1100 Ion Sputter installation. Microstructural examinations were conducted using a Neophot-32 light microscope, a JSM-35CA scanning electron microscope (SEM), JAMP-9500F Auger microprobe from JEOL, and micro-X-ray spectral analysis (MXRA) using an INCA-450 analyzer from OXFORD INSTRUMENTS with a probe diameter of approximately 1 μm [25]. Microhardness measurements of the metal in the heat-affected zone were performed using a LECO M-400 microhardness tester at loads of 1.0–5.0 N.

EXPERIMENTAL RESULTS

MICROSTRUCTURE OF THE BASE METAL (BM) IN THE VZhL12U AND EI698VD ALLOYS

The microstructure of the VZhL12U cast alloy in its as-delivered state (Figure 2, *a*) consists of an austenitic matrix (γ-phase), which is a solid solution of chromium, cobalt, molybdenum and tungsten in a nickel matrix, and

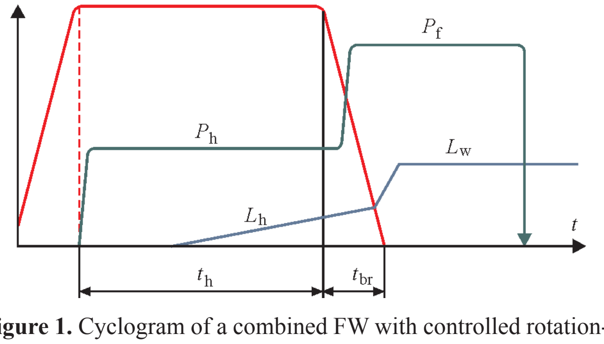

Figure 1. Cyclogram of a combined FW with controlled rotational braking: n — rotational frequency; P_h, P_f — pressure during heating and forging; L_h, L_w — upset distances during heating and welding; t_h — heating time; t_{br} — rotational braking time

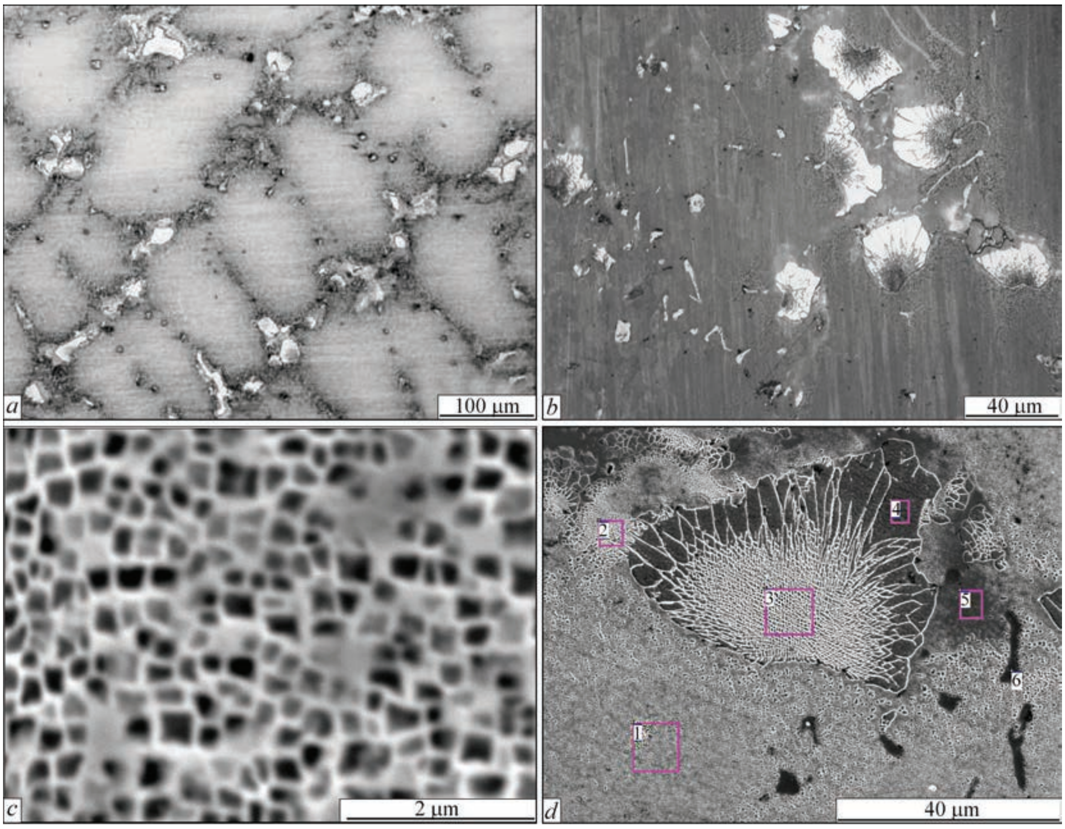

No.	C	O	Al	Ti	V	Cr	Mn	Fe	Co	Ni	Nb	Mo	W
1	1.04	0.23	3.80	3.26	0.79	10.76	0.22	0.45	14.95	59.61	0.56	3.24	1.09
2	1.37	0.42	3.99	5.73	0.67	8.35	0.13	1.25	13.25	60.94	0.76	2.80	0.35
3	1.36	0.31	3.90	5.27	0.66	9.04	0.20	1.05	13.39	60.83	0.79	2.45	0.67
4	1.12	0	4.91	7.59	0.12	3.31	0	0.46	10.18	69.93	0.93	1.09	0.29
5	0.93	0	3.59	4.41	1.0	10.61	0	0.51	14.42	59.11	0.73	3.90	0.68
6	15.65	0	0.07	35.06	1.34	1.27	0.26	0.32	1.35	0.31	21.30	16.74	6.32

Figure 2. Microstructure of BM of the VZhL12U alloy (*a*, *b*), optical microscopy; γ′-phase precipitation (*c*); microstructure and chemical composition (wt.%) of structural elements (*d*); SEM

particles of the strengthening γ′-phase — a solid solution based on the intermetallic compound Ni_3(Al, Ti) and MeC-type carbides. Alongside the cubic γ′-phase precipitates typical of nickel superalloys, which are dispersed within the γ-phase matrix, the VZhL12U alloy BM microstructure contains particles of the primary eutectic γ'_{eut} phase, which are located in the interdendritic regions (Figure 2, *b*). An increased content of titanium and aluminium is observed in the γ'_{eut} phase particles (spectrum 4, Figure 2, *d*). The irregularly shaped γ′-phase particles are significantly larger in size (10–50 μm) than the dispersed γ′-phase precipitates located within the dendrites (Figure 2, *c*). During heating, the $\gamma'_{eut.}$-phase is thermally stable practically up to the $T_{solidus}$ of the VZhL12U alloy. A distinctive feature of the VZhL12U alloy BM in its as-delivered state is an uneven distribution of dispersed γ′-phase particles within the dendrites. As a result of dendritic liquidation, the γ′-phase particles in the central part of the dendrites have dimensions of 300–400 nm, whereas those in the peripheral part have dimensions of 500–600 nm. Complex MeC carbides (where Me is Ti, Ni, Mo, W) in the form of discrete polyhedral particles are located predominantly within the dendrites, whereas carbides in the form of script-like particles are found between the axes of the dendrites (Figure 3).

The BM of forged specimens of the EI698VD alloy reveals a fibrous structure (Figure 4). The microstructure of the EI698VD alloy is equiaxed, with an average grain size of 35–40 μm (Figure 4, *b*). The fine structure of the alloy is shown in Figure 4, *c*. The γ′-phase precipitates exhibit a bimodal distribution: the primary γ′-phase particles, which form during quenching from a temperature of 1000 °C, have dimensions of 0.25–0.3 μm, whereas the particles of the secondary γ′-phase, which form during ageing at 775 °C, have dimensions of approximately 0.03–0.04 μm.

MICROSTRUCTURE OF THE JOINT BETWEEN THE VZhL12U AND EI698VD ALLOYS IN THE STATE AFTER FW

The macro- and microstructural examination of the joints was carried out on two joint specimens (Figure 5) produced by the combined FW process with different rotational braking times t_{br}, namely: t_{br1} = 0.3 s (joint 1) and t_{br2} = 3.0 s (joint 2). The increased forg-

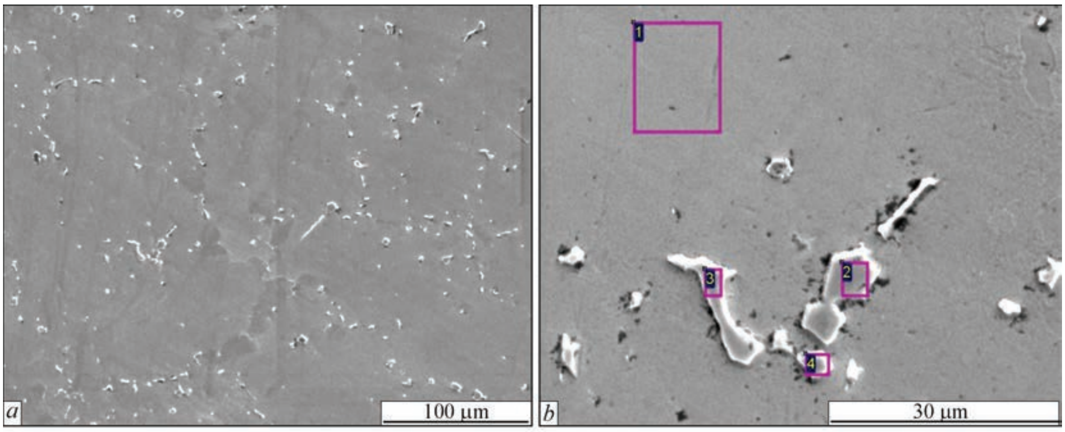

No.	C	Al	Ti	V	Cr	Co	Ni	Nb	Mo	W
1	0.78	5.44	2.56	0.81	8.54	12.54	66.01	0.34	1.95	0.75
2	11.48	0.15	42.09	2.43	0.99	1.07	5.26	15.53	10.86	10.13
3	7.46	1.05	16.54	1.52	5.50	8.35	39.82	7.66	7.61	4.47
4	7.99	0.91	21.92	1.54	4.53	7.98	34.32	8.13	6.57	6.10

Figure 3. Microstructure (*a*) and chemical composition (wt.%) of the structural elements of the VZhL12U alloy (*b*), SEM

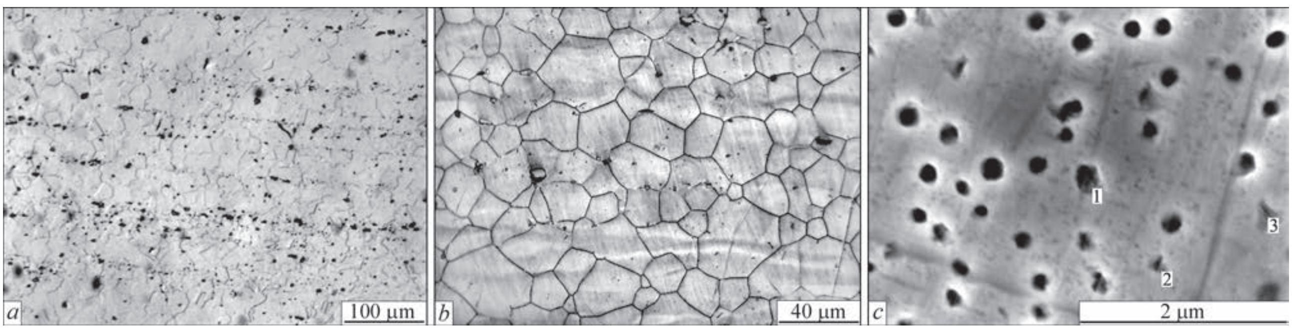

Figure 4. Microstructure of BM of the EI698VD alloy (*a*, *b*), γ′-phase precipitation (*c*)

ing pressure P_f was applied simultaneously with the start of rotational braking (see Figure 1). The set values for the other process parameters of the FW process were as follows: $V = 1$ m/s, $P_h = 200$ MPa, $P_f = 400$ MPa, $t_h = 20$ s, $t_f = 10$ s. As the hydraulic drive of the MST2001 machine ensures a pressure rise from P_h to P_f in approximately 0.4 s, for joint 1 the set value of P_f was applied to non-rotating billets, which is characteristic of conventional FW. For joint 2, the forging pressure was applied to billets rotating at a frequency that gradually decreased from the set value to 0, which is typical of IFW.

The macro- and microstructures of the joints were investigated at different distances from the axis of the billets (Figure 6): in the peripheral region (section *I–I*) and the central region (section *II–II*). It was found that the macrostructure of the joints depends significantly on the rotational braking time t_{br}. As t_{br} grows from 0.3 to 3 s, the upsetting value (shortening) of the billets at the forging stage rises from 1.4 to 4.2 mm. Depending on the value of t_{br}, the shape of the joint line changes and the amount of burr (metal displaced beyond the cross-section of the billets) increases. At $t_{br} = 0.3$ s (joint 1), the

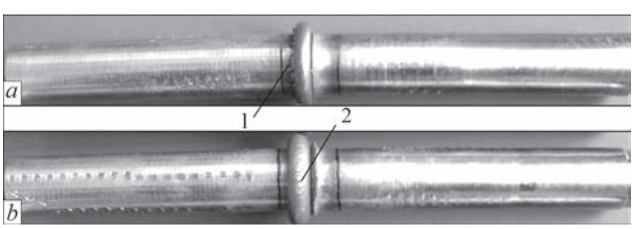

Figure 5. Welded specimens of the EI698VD and VZhL12U alloys: joint 1 (*a*); joint 2 (*b*)

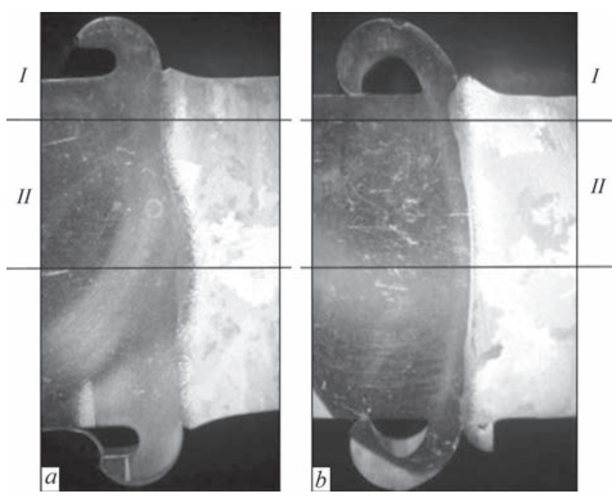

Figure 6. Macrosections of joints between the VZhL12U and EI698 alloys: joint *I* (*a*), joint *II* (*b*)

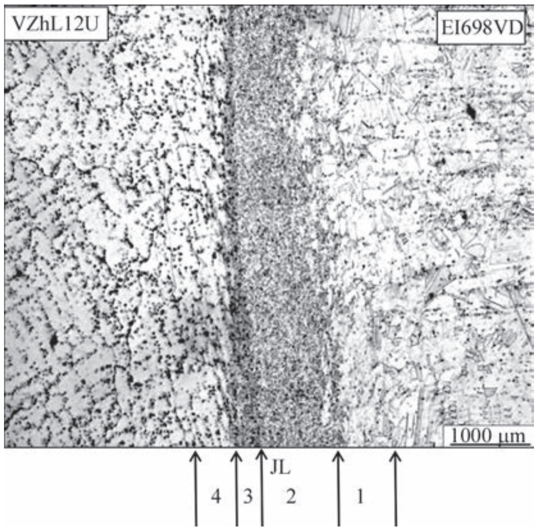

Figure 8. Microstructure of the joint 2, ×25: 1 — TMAZ boundary of the EI698VD alloy; 2 — DRZ of the EI698VD alloy; 3 — DRZ of the VZhL12U alloy; 4 — TMAZ of the VZhL12U alloy; JL — joint line

joint line (JL) is curved (Figure 6, *a*) and the formation of a burr observed predominantly on the side of the EI698VD alloy specimen. The VZhL12U alloy underwent virtually no deformation during the FW process, with the exception of the central part of the cross-section. In this part (cross-section *II–II*), the JL is observed to be concave towards the VZhL12U alloy.

The microstructure of the joint on the VZhL12U alloy side varies across the cross-section of the specimens. In the central part of the cross-section (Figure 7, *a*), there are no visible defects or significant segregation of elements; the joint was formed here at the lowest temperature across the cross-section of the billets. In the peripheral part of the cross-section (Figure 7, *b*), where the maximum temperature is reached during the FW process, the JL with an interlayer is observed; as was revealed by MXRA, this interlayer has an elevated aluminium and titanium content and, in terms of chemical composition, it corresponds to eutectic phases, which are situated along the boundaries of dendrites in the BM of the VZhL12U alloy. The presence of JL with an interlayer of eutectic composition in the peripheral part of the cross-section on the VZhL12U alloy side, experimentally confirms that $T_{solidus}$ of the VZhL12U alloy during the FW process is reached and local regions of the melt are formed that were not displaced beyond the cross-section during forging. The possibility of reaching the melting point in the contact zone during the FW of the EI698VD alloy had previously been established by calculation [22]. Furthermore, in the joint plane of the peripheral part of the cross-section, particles of the γ'_{eut}-phase are observed which did not dissolve during the forging process (Figure 7, *c*).

The macrostructure of the joint produced by combined FW with a braking time of t_{br} = 3.0 s across the entire cross-section of the billets takes the form of an arc curved towards the VZhL12U cast alloy (joint 2, see Figure 6, *b*), although plastic deformation and the formation of a burr during the FW process occur predominantly on the side of the EI698VD alloy specimen. Examination of the welded joint after ion polishing and etching of the sections revealed that the microstructure of the joint consists of a sequence of zones with varying grain sizes (Figure 8). No defects were detected in the joint zone between the EI698VD and VZhL12U alloys. The total width of the dynamic recrystallization zone (DRZ) of the joint varies over the cross-section of the billets and ranges from 1300 to 1800 μm. Since the high-temperature strength of the EI698VD alloy is significantly lower than that of the VZhL12U alloy, the width of the DRZ of the EI698VD alloy is considerably larger than that of the VZhL12U alloy.

The average grain size in the DRZ of the EI698VD alloy ranges from 14 to 20 μm, while in the DRZ of the VZhL12U alloy it ranges from 10 to 15 μm. In the thermomechanical affected zone (TMAZ) of the EI698VD alloy, a necklace-like structure is observed (Figure 9), showing that the formation of fine recrystallized grains along the boundaries of the austenitic BM grains experienced significant thermomechanical effect. Analysis of the joint microstructure reveals a change in the texture orientation of the rolled material BM in the joint zone of the EI698VD alloy (Figure 10, *a*). The fine structure of the joint on the EI698VD alloy side is

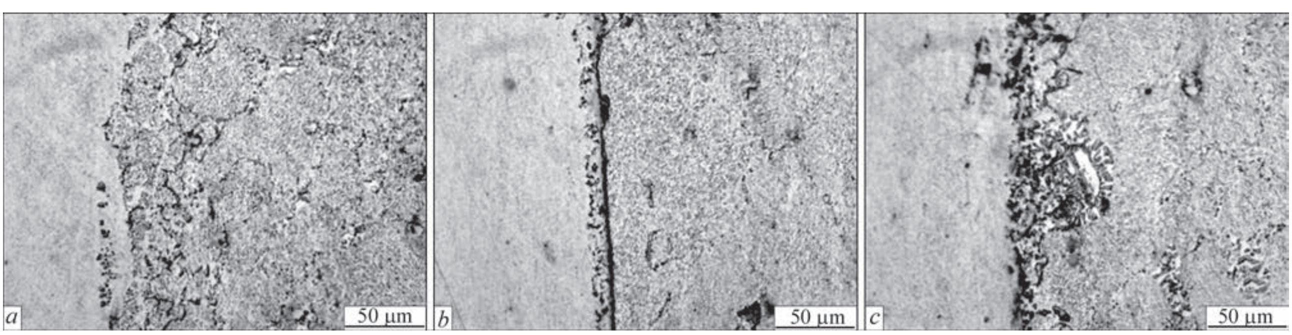

Figure 7. Microstructure of joint 1 on the VZhL12U alloy side in the central (*a*) and peripheral parts of the cross-section (*b*, *c*): *b* — continuous interlayer with an increased content of carbide-forming elements; *c* — precipitation of the eutectic γ'_{eut}-phase in the joint plane

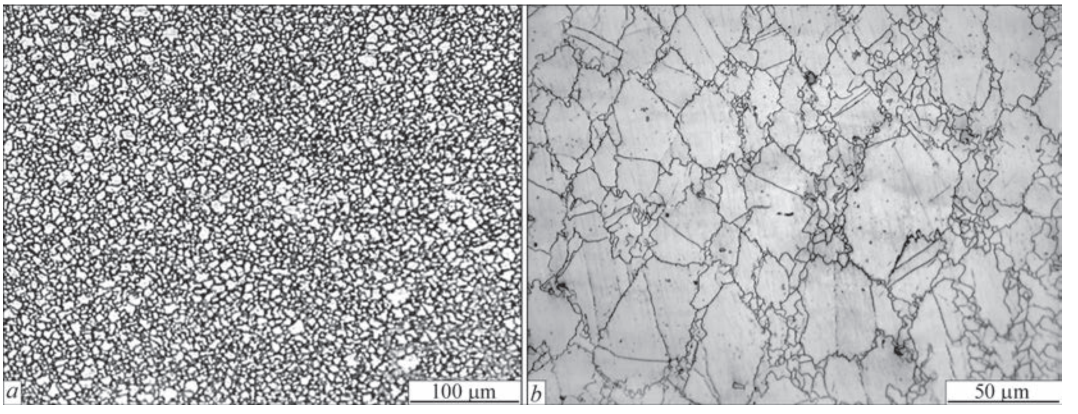

Figure 9. Microstructure of different sections of the joint on the EI698VD alloy side: DRZ (*a*), TMAZ (*b*)

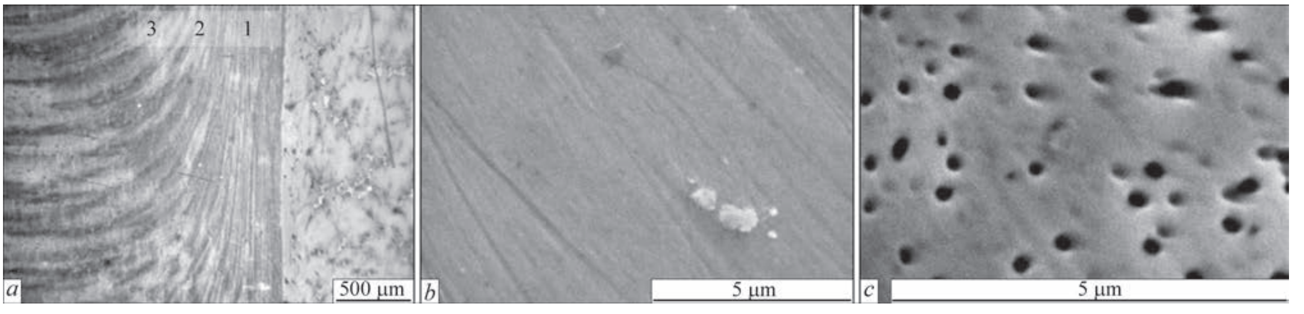

Figure 10. Microstructure of the joint (*a*), fine structure on the EI698VD alloy side in the DRZ (*b*), HAZ (*c*)

shown in Figure 10, *b*, *c*. In the DRZ and TMAZ, the γ′-phase particles (primary and secondary) are completely dissolved (Figure 10, *b*). In the heat-affected zone (HAZ), complete dissolution of the dispersed particles of the secondary γ′-phase and partial dissolution of the primary γ′-phase are observed (Figure 10, *c*).

It was established that, at a rotational braking time of t_{br} = 3.0 s, the microstructure and morphology of phase precipitates in the joint zone on the VZhL12U alloy side significantly changes. The cast dendritic structure of the VZhL12U alloy in the DRZ and TMAZ experiencing plastic deformation during the combined FW process, transformed into a fibrous structure, which is typical of wrought alloys (Figure 11). The thermally stable particles of the primary eutectic γ'_{eut} phase in the DRZ are completely dissolved, while the carbide phases with a script-like morphology are refined and more evenly distributed within the austenitic matrix. Metal with such a structure is expected to exhibit better strength, ductility and toughness compared to the cast dendritic structure of the VZhL12U alloy BM.

The results of the carried out studies showed that an increase in t_{br} at the forging stage significantly affects the structural and phase transformations in the joint zone and TMAZ of both alloys. Since, during FW of joint 2, the forging pressure was applied to the billets rotating at a frequency that gradually decreases from a set value to 0 over a time t_{br} = 3.0 s, the conditions for joint formation characteristic of the IFW process were realized in the FW process [17, 18]. This type of FW is characterized by a gradual decrease in temperature in the contact zone at the final stage of braking, accompanied by an increase in the upsetting rate. The effect of particle dissolution — both of the secondary dispersed γ′-phase and the thermally stable primary γ'_{eut}-phase from the VZhL12U cast alloy indicates the predominant role of plastic deformation in the formation of the microstructure and phase composition of the joint zone in nickel superalloys.

MICROSTRUCTURE OF THE JOINT BETWEEN THE VZhL12U AND EI698VD ALLOYS AFTER HT

The effect of the postweld HT conditions on the microstructure and microhardness distribution in the joint zone of the EI698VD and VZhL12U alloys was investigated. Based on the results of examining the fine metal structure in the joint zone, it was found that the microhardness distribution on the EI698VD alloy side is determined by the presence and morphology of secondary γ′-phase particles. Since secondary γ′-phase particles in the DRZ, TMAZ and HAZ on the side of the EI698VD alloy are completely dissolved (see Figure 10, *b*, *c*), a significant reduction in microhardness (Figure 12, *a*) is observed in the joint zone on the side of the EI698VD alloy in the state after FW. The microhardness profile on the VZhL12U alloy side has no regions with reduced values compared to the BM results, indicating the reprecipitation of γ′-phase particles during the cooling of the joints.

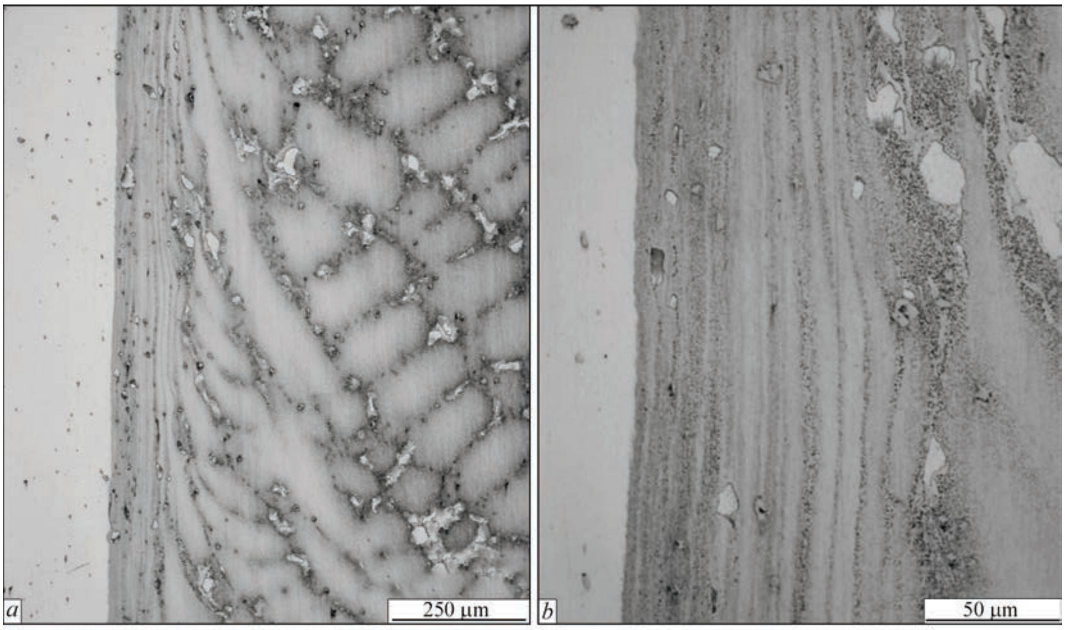

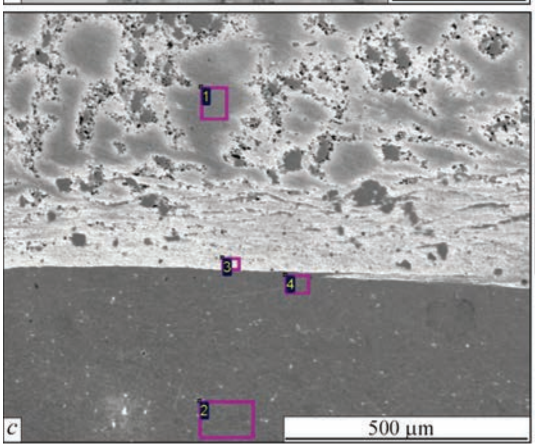

No.	Al	Ti	V	Cr	Fe	Co	Ni	Mo	W
1	4.73	2.62	0.68	9.26	0	13.46	66.32	2.93	1.26
2	1.51	3.02	0	15.42	0	0	77.31	2.74	0
3	5.35	5.94	0.60	5.40	0	11.41	68.34	2.96	1.17
4	1.17	2.53	0	13.22	0.67	0	78.09	4.32	0

Figure 11. Microstructure of the joint 2 on the VZhL12U alloy side: general view of the wrought dendritic structure (*a*), fibrous structure without particles of the eutectic γ'_{eut}-phase in the joint plane (*b*), MXRA results in different regions of the joint zone (*c*)

A single-stage HT treatment was carried out, namely ageing at t_h = 775 °C, holding at τ = 16 h to restore the precipitation of the secondary γ'-phase on the EI698VD alloy side. The nature of the change in microhardness in the joint zone is shown in Figure 12, *b*. During single-stage HT, a decrease in the microhardness in the BM of the EI698VD alloy was observed due to its overageing and the coagulation of the secondary γ'-phase particles.

After three-stage HT in accordance with the technical specifications for the EI698VD alloy (first quenching from 1100 °C, holding for 8 h; second quenching from 1000 °C, holding for 4 h; ageing at 775 °C, holding for 16 h), an increase in microhardness is achieved in the joint zone to the level of the BM of the EI698VD alloy (Figure 12, *c*), which indicates the restoration of the grain structure and particle morphology of the primary and secondary γ'-phase.

Research has revealed an anomalous coarsening of the dispersed γ'-phase particles (Figure 13, *a*, *b*) in the DRZ of the VZhL12U alloy after a three-stage HT in accordance with the technical specifications for the EI698VD alloy. The HT conditions for the VZhL12U alloy are heating to a temperature of 1100 °C with a holding for 8 h are; during this process, the particles of phase precipitates must not dissolve or increase in size, as the temperature at which the dispersed γ'-phase is completely dissolved is T_{solvus} = 1220 °C (see Table 2). This is evidenced by the unchanged microstructure and fine structure of the VZhL12U alloy BM, as well as the unchanged morphology of the primary γ'_{eut}-phase in the HAZ after three-stage HT of joint 2. Only in the joint zone, which has a fine-grained, dynamically recrystallized structure, an increase in the particle size of the dispersed γ'-phase to 2–4 µm is observed, and its dimensions are comparable to those of the γ-phase grains (austenitic matrix). In this context, the microhardness values on the VZhL12U alloy side correspond to those of BM (see Figure 12, *c*). The revealed anomalous coarsening of the dispersed γ'-phase particles during HT is probably related to the significant accumulated

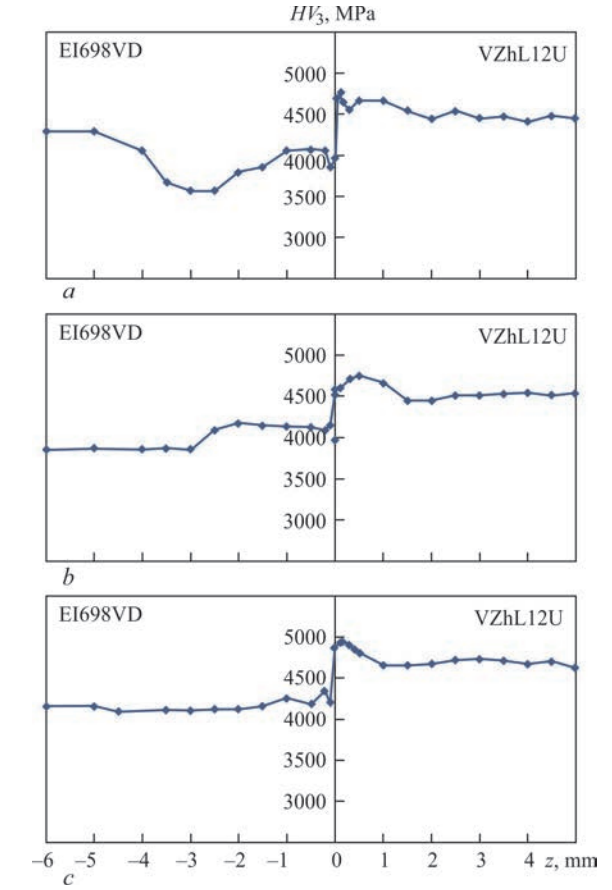

Figure 12. Microhardness distribution in the joint zone of the EI698VD+VZhL12U alloys in the state after FW (*a*), after single-stage (*b*) and three-stage HT (*c*)

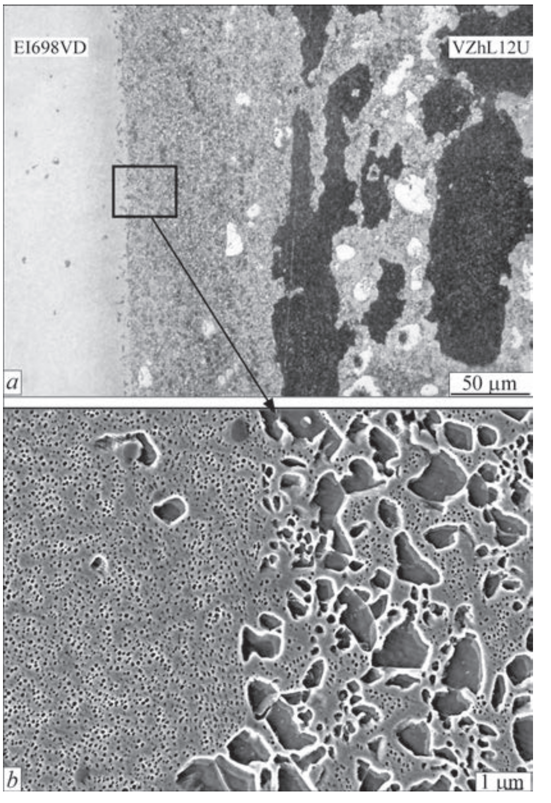

Figure 13. Microstructure (*a*) of the joint; fine structure in the DRZ of the VZhL12U alloy after three-stage HT (*b*)

deformation energy in the DRZ of the VZhL12U alloy and will be the subject of further research.

CONCLUSIONS

1. The macro- and microstructure of dissimilar joints in the VZhL12U cast alloy and the EI698VD forged alloy, produced using a combined FW process with controlled rotational braking, were investigated. It was found that as the rotational braking time t_{br} at the forging stage increased from t_{br} = 0.3 to 3.0 s, the microstructure of the metal and the morphology of the strengthening phases in the dissimilar joints changed significantly. The cast dendritic structure of the VZhL12U alloy in the joint zone at t_{br} = 3.0 s, under the influence of plastic deformation during the combined FW process, transformed into a fibrous structure characteristic of wrought alloys.

2. It was established that at t_{br} = 0.3 s, along the JL on the VZhL12U alloy side, an interlayer of γ_{eut} particles composition is observed in the peripheral part of the billet cross-section; this experimentally confirms that during the FW process, the VZhL12U alloy reaches its solidus temperature and local molten regions are formed, which is not displaced beyond the cross-section during forging.

3. In the joint plane, on the EI698VD alloy side, the γ′-phase particles (primary and secondary) are completely dissolved. It was established that the distribution of microhardness in the joint zone on the side of the EI698VD alloy is determined by the presence and morphology of particles of the secondary highly dispersed γ′-phase.

4. Microstructural and phase transformations in dissimilar joints of the VZhL12U and EI698VD alloys was determined under various postweld HT conditions. At a single-stage HT (ageing at t_h = 775 °C, holding time τ = 16 h), which was carried out to restore the precipitation of the secondary γ′-phase in the EI698VD alloy, a decrease in the microhardness of the BM of the EI-698VD alloy was observed due to overageing and the coagulation of secondary γ′-phase particles.

5. After three-stage HT in accordance with the technical specifications for the EI698VD alloy, an increase in microhardness is achieved in the joint zone to the level of the BM of the EI698VD alloy, indicating the restoration of the grain structure and particle morphology of the primary and secondary γ′-phases. The microhardness values on the VZhL12U alloy side correspond to those of the base metal.

6. An anomalous coarsening of the dispersed γ′-phase particles in the DRZ of the VZhL12U alloy was observed after three-stage HT in accordance with the technical specifications for the EI698VD alloy. This phenomenon is probably related to the significant accumu-

lated deformation energy in the DRZ of the VZhL12U alloy and will be the subject of further research.

REFERENCES

1. Sims, C.T., Stoloff, N.S., Hagel, W.C. (1987) *Superalloys II*. New York, John Wiley & Sons.
2. Pollock, T.M., Tin, S. (2006) Nickel-based superalloys for advanced turbine engines: Chemistry, microstructure and properties. *J. of Propulsion and Power*, 22(**2**), 361–374. DOI: https://doi.org/10.2514/1.18239
3. Reed, R.C. (2008) *The superalloys: Fundamentals and applications*. New York, Cambridge University Press.
4. Das, N. (2010) Advances in nickel-based cast superalloys. *Transact. of the Indian Institute of Metals*, **63**, 265–274. DOI: https://doi.org/10.1007/s12666-010-0036-7
5. Henderson, M.B., Arrell, D., Hoebel, M. et al. (2004) Nickel-based superalloy welding practices for industrial gas turbine applications. *Sci. and Technol. of Welding and Joining*, 9(**1**), 13–21. DOI: https://doi.org/10.1179/136217104225017099
6. Bhamji, I., Preuss, M., Threadgill, P.L., Addison, A.C. (2010) Solid state joining of metals by linear friction welding: A literature review. *Mater. Sci. and Technol.*, **27(1)**, 2–12. DOI: https://doi.org/10.1179/026708310X520510
7. Preuss, M., Threadgill, P. (2010) *Solid state welding of aeroengine materials*: Encyclopedia of Aerospace Engineering. Eds by R. Blockley, W. Shyy. DOI: https://doi.org/10.1002/9780470686652.eae222
8. Ajay, V., Babu, N.K., Ashfaq, M. et al. (2021) A review on rotary and linear friction welding of inconel alloys. *Transact. of the Indian Institute of Metals,* **74**, 2583–2598. DOI: https://doi.org/10.1007/s12666-021-02345-z
9. Li, W., Vairis, A., Preuss, M., Ma, T. (2016) Linear and rotary friction welding review. *Inter. Materials Reviews*, 61(**2**), 71–100. DOI: https://doi.org/10.1080/09506608.2015.1109214
10. Zyakhor, I.V., Zavertanny, M.S., Chernobaj, S.V. (2014) Linear friction welding of metallic materials (Review). *The Paton Welding J.*, **12**, 25–31. DOI: https://doi.org/10.15407/tpwj2014.12.06
11. Raab, U., Levin, S., Wagner, L., Heinze, C. (2015) Orbital friction welding as an alternative process for blisk manufacturing. *J. of Materials Processing Technology*, **215**, 189–192. DOI: https://doi.org/10.1016/j.jmatprotec.2014.06.019
12. Maly, A.B., Butenko, Yu.V., Khorunov V.F. (2005) Weldability of high-alloyed heat-hardenable nickel-base alloys (Review). *The Paton Welding J.*, **5**, 19–22.
13. Yushchenko, K.A., Savchenko, V.S., Chervyakov, N.O., Zvyagintseva, A.V. (2004) Yushchenko K.A., Savchenko V.S., Chervyakov N.O. and Zvyagintseva A.V. Character of formation of hot cracks in welding cast heat-resistant nickel alloys. *The Paton Welding J.*, **8**, 34–38.
14. Pinchuk, N.I., Ryazantsev, N.K. (2004) Effect of primary structure of cast heat-resistant nickel alloys on formation of hot cracks during welding. *The Paton Welding J.*, **2**, 17–24.
15. Preuss, M., Withers, P.J., Baxter, G.J. (2006) A comparison of inertia friction welds in three nickel base superalloys. *Mater. Sci. and Eng. A*, **437**, 38–45. DOI: https://doi.org/10.1016/j.msea.2006.04.058
16. Huang, Z.W., Li, H.Y., Preuss, M. et al. (2007) Inertia friction welding dissimilar nickel-based superalloys alloy 720Li to In718. *Metallurgical and Materials Transact. A*, **38**, 1608–1619. DOI: https://doi.org/10.1007/s11661-007-9194-6
17. Wang, F.F., Li, W.Y., Li, J.L., Vairis, A. (2014) Process parameter analysis of inertia friction welding nickel-based superalloy. *Inter. J. Adv. Manuf. Technol.,* **71**, 1909–1918. DOI: https://doi.org/10.1007/s00170-013-5569-6
18. Preuss, M., Pang, J.W.L., Withers, P.J., Baxter, G.J. (2002) Inertia welding nickel-based superalloy. Pt 1. Metallurgical characterization. *Metallurgical and Materials Transact. A,* **33A**, 3212-3224. DOI: https://doi.org/10.1007/s11661-002-0307-y
19. Tra, T.H., Sakaguchi, M. (2016) High cycle fatigue behavior of the IN718/M247 hybrid element fabricated by friction welding at elevated temperatures. *J. of Science: Advanced Materials and Devices*, 1(**4**), 501–506. DOI: https://doi.org/10.1016/j.jsamd.2016.08.009
20. Taysom, B.S., Sorensen, C.D., Nelson, T.W. (2021) Strength in rotary friction welding of five dissimilar nickel-based superalloys. *Welding J. 100*, **9**, 302S–308S. DOI: https://doi.org/10.29391/2021.100.027
21. Amegadzie, M.Y., Ola, O.T., Ojo, O.A. et al. (2012) On liquation and liquid phase oxidation during linear friction welding of nickel-base IN 738 and CMSX 486 superalloys. In: *Proc. of 12th Inter. Symp. on Superalloys (Superalloys 2012), Seven Springs Mountain Resort, PA*. 587–594. DOI: https://doi.org/10.7449/2012/Superalloys_2012_587_594
22. Kuchuk-Yatsenko, S.I., Zyakhor, I.V., Velikoivanenko, E.A., Rozynka, G.F. (2009) Calculation of thermal-deformation conditions of formation of friction welded joints on heat-resistant alloy EI698VD. *The Paton Welding J.,* **7**, 7–11.
23. Ziakhor, I.V., Zavertannyi, M.S., Levchuk, A.M., Kapitanchuk, L.M. (2020) Peculiarities of formation of dissimilar nickel-base alloy joints in friction welding. *The Paton Welding J.*, **8**, 34–40. DOI: https://doi.org/10.37434/tpwj2020.08.06
24. Zyakhor, I.V. (2001) Modern equipment for friction welding. *The Paton Welding J.,* **7**, 48–52.
25. Zadorozhniuk, O.M., Kapytanchuk, L.M., Smiyan, O.D., Butkova, E.I. (2013) New possibilities for metallographic investigation of base metals and welded joints. *Sovremennaya Elektrometallurgiya*, **2**, 36–40 [in Russian].

ORCID

I.V. Ziakhor: 0000-0001-7780-0688,
A.M. Levchuk: 0000-0002-0361-7394

CONFLICT OF INTEREST

The Authors declare no conflict of interest

CORRESPONDING AUTHOR

I.V. Ziakhor
E.O. Paton Electric Welding Institute of the NASU
11 Kazymyr Malevych Str., 03150, Kyiv, Ukraine
E-mail: zyakhor2@ukr.net

SUGGESTED CITATION

I.V. Ziakhor, A.M. Levchuk (2026) Microstructure and phase composition of joints of cast and wrought nickel superalloys produced by friction welding. *The Paton Welding J.*, **08**, 13–22.
DOI: https://doi.org/10.37434/tpwj2026.08.02

JOURNAL HOME PAGE

https://patonpublishinghouse.com/eng/journals/tpwj

Received: 02.04.2026
Received in revised form: 14.04.2026
Accepted: 28.07.2026

DOI: https://doi.org/10.37434/tpwj2026.08.03

PHYSICAL MODELING OF STRUCTURE FORMATION OF THE WELD METAL DURING HEAT TREATMENT OF TRAM TRACK JOINTS

I.V. Krivtsun, R.S. Hubatyuk, O.S. Prokofiev, S.V. Rymar, E.O. Panteleimonov, V.A. Kostin, S.G. Hryhorenko, V.V. Zhukov, I.O. Goncharov, G.V. Kuzmenko

E.O. Paton Electric Welding Institute of the NASU
11 Kazymyr Malevych Str., 03150, Kyiv, Ukraine

ABSTRACT

The results of physical modeling on model samples of structure formation of the weld metal during heat treatment of welded joints of tram rails are presented. Model samples in the form of rods were cut out of real welded joints of the head of rails of R65 type made of steel of K76F grade. The joints were made by automatic arc welding by the consumable guide using flux-cored filler welding wire of ANPM-3 brand. Sections of thermokinetic diagrams of the decomposition of supercooled austenite during continuous cooling of the metal of the weld made by arc welding and its zone of fusion with the base metal of the rail were constructed for the first time, which allowed us to determine changes in the metal structure and its hardness at different cooling rates. Physical modeling on model samples allowed establishing the parameters of heat treatment of welded rail joints, which improve the properties of the metal, increase its hardness and remove residual stresses. Heat treatment will have a positive effect on improving the operational properties and increasing the reliability and service life of welded rail joints, which is important during construction and repair of tram tracks.

KEYWORDS: welded joints, tram rails, heat treatment, physical modeling, thermokinetic diagrams, reliability increase

INTRODUCTION

Scientific-research work performed at PWI is a development of the theoretical and experimental studies in the field of the technology of induction heat treatment of welded butt joints of rails [1–5], and it is aimed at increasing the operational properties of tram rail tracks due to improvement of the structural homogeneity and formation of the required microstructural composition of the metal of a weld made by arc welding, residual stresses relieving and hardness equalization.

Electric arc welding of rails is usually performed using the following processes: coated stick electrode, submerged-arc, gas-shielded, flux-cored wire, electroslag welding, etc [6]. Manual arc welding with stick electrodes is the simplest, but the least advanced and a low-productivity method, where the welded joint quality entirely depends on welder's qualifications [7]. It is mainly applied for bath welding of the crane and tram rails [8].

In order to improve the welding quality and productivity, semi-automatic bath welding with rail preheating to prevent cold cracking is used, by which railway tracks, in particular metro tracks, can be welded [8].

Investigations performed at PWI [9] show that cold cracks initiate in the HAZ metal in the case of electric arc welding of the rails without application of their preheating to a temperature above 250 °C.

A method of closed-arc welding of high-strength rail steels with high-carbon electrodes with preheating and postweld heat treatment is known [10]. This is a combination of the methods of automatic gas-shielded consumable electrode welding of the railway rail base and narrow-gap electroslag welding of its web and head [10].

In Japan advancement of the technology and welding consumables and application of heat treatment allowed a significant improvement of welded joints quality and successful application of electric arc welding in the construction of the high-speed railway lines [11]. The rail welding process includes deposition of the root bead with through penetration, multipass welding of the base, continuous welding from the base to the head and multipass welding of the rail web [7]. Standard rails from carbon steel are welded with low-carbon welding wire of 800–1100 MPa class, which produces a weld with bainitic structure. For high-strength rails high-carbon welding wire is used to produce a pearlitic structure of the weld metal with an improved wear and abrasion resistance of the weld metal [7, 11]. The weld width is ensured at the level of 20 mm, and the HAZ width is 100 mm. Weld metal hardness is close to that of the rail base material of *HV* 390, but lower hardness zones are present on the weld sides. Heat treatment of the welded joint allows reducing the hardness gradient and shifting the lower hardness zones up to 60 mm from the weld center [11].

PWI developed the technology of automatic electric arc bath welding with a consumable nozzle (AAW-

CN) [12, 13] based on application of self-shielded flux-cored wire fed through a flat consumable nozzle. This method allows performing welding into a nominal gap of 12–16 mm between the rail ends with the possibility of conducting welding also into 8–22 mm gap [13]. Automation and mechanization of this process increased the operation productivity 2–3 times, while providing a stable welding quality and acceptable mechanical characteristics of the joints [12, 13]. Brinell hardness of *HB* 2600–3200 MPa with ultimate strength of 800–900 MPa was obtained for weld metal in the welded joint of R65 rails [12]. Breaking load during static bend testing with the deflection of 16–22 mm was equal to 1500–1650 kN. The developed all-purpose equipment is mobile. The technology allows welding the rail tracks of industrial enterprises, trams and crane tracks, and in the future — performing operational repairs on the railways [7]. The technology provides an acceptable quality of the welded joints of rails and currently does not use postweld heat treatment.

In this work research is performed of the possibility of heat treatment application in the AAW-CN method to achieve an even greater improvement of the quality of the welded joints of tram tracks.

AAW-CN [12, 13] produces a relatively wide weld with a heterogeneous metal composition, which forms as a result of interaction of the filler wire metal with the rail metal. After welding, the rail weld width along the rail height can vary in the range of 15–40 mm in different rail regions, and the HAZ width varies in the range of 20–75 mm (smaller values are observed in the rail head, medium ones — in its neck, and greater ones — in the base). For heat-hardened rails the weld center is characterized by a lowering of the metal hardness, and its near-weld zone — by 10 % increase. His percentage is lower in non-heat-hardened rails. A relatively large width of the weld with a lower hardness in the wheel-rail contact zone may lead to rail dipping, and increased hardness of the near-weld zone may lead to cracks and metal spalling. It results in deterioration of the welded joint performance during the rail track operation. The welded joints are also characterized by internal residual stresses. Modern requirements to the track reliability necessitate an improvement of the quality of rail welded joints and reduction of the impact of the above-mentioned negative post-welding factors. Correctly selected heat-treatment modes improve the mechanical properties of the welded joints and equalize the metal hardness [14, 15]. In order to weaken the influence of the zones of internal residual stresses arising during welding and to improve the metal structure of the zones of welded joints of rails having a complex profile, the technology of the rail induction heat treatment by high-frequency currents is the most optimal at the modern state of technology development. This technology ensures a high speed of local heating of the welded joint metal [16–20].

Theoretical and practical research is relevant and important, which should be aimed at studying the metal structure formation in the rail welded butt joints after their heat treatment and establishing substantiated treatment modes, which have a positive impact of the kinetics of the structural transformations in the metal [21–24]. For this purpose, it is necessary to plot parts of thermokinetic diagrams of the alloy of the filler wire metal with the rail metal in the specified temperature range of austenitic transformation of the metal, at different cooling rates.

THE OBJECT

of study is formation of the weld metal structure during heat treatment of the arc-welded joints of tram track rails.

THE AIM

of the work is determination of the necessary modes of heat treatment of the rail welded joints, made by AAW-CN method. For this purpose, it is necessary to solve the following tasks: establish the kinetics of phase transformations during cooling of the welded joint metal with determination of the influence of the cooling rates on formation of the final microstructure in the welded joint metal. Such studies of the AAW-CN method and the above-mentioned alloy were conducted for the first time and they are based on the experience of works [1–5, 25], carried out at PWI in order to develop the technology of heat treatment of the rail welded joints made by flash-butt welding.

As a rule, tram girder rails of various grades are currently used in the tram tracks in Ukraine. They are applied in the curvilinear sections and within the roadway, and rails of R65 type laid in the straight sections outside the roadway and in the high-speed sections of the tram track. These tracks are made from related high-carbon rail steels of grades M76 and K76F, respectively. Wire of ANPM-3 brand is used as the welding consumable for AAW-CN.

The work is aimed at creating a basis for development of the technology and induction equipment for heat treatment of arc-welded joints of rails.

RESEARCH MATERIALS AND METHODS

include: metallographic methods of studying the crystalline structure of the metal, using light microscopy; dylatometric studies with construction of parts of thermokinetic diagrams of supercooled austenite decomposition; durometric studies with measurement of the weld metal hardness; thermoelectrometry and

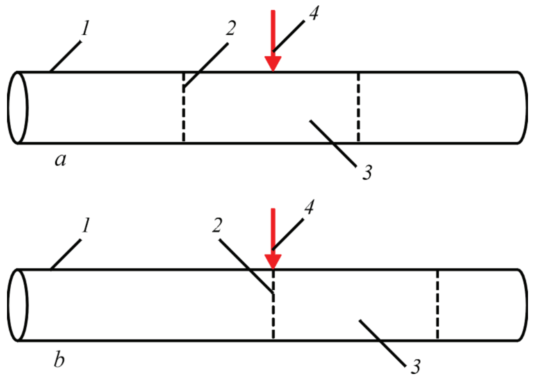

Figure 1. Schematic of two types of samples for conducting a dilatometric study: *a* — welded metal in the sample center (type I); *b* — fusion zone in the sample center (type II); *1* — cylindrical metal sample; *2* — fusion line; *3* — welded joint zone; *4* — contact points of dilatometer probes

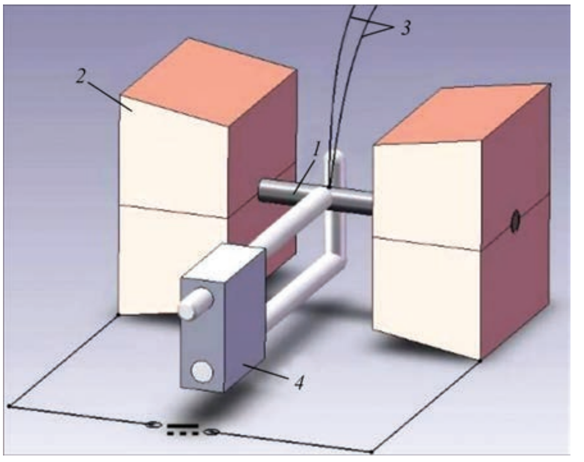

Figure 2. Schematic of Gleeble 3800 system for simulation [1] of the thermo-deformation state of metal materials: *1* — metal sample; *2* — cooled copper clamps; *3* — thermocouple; *4* — dilatometer

pirometry methods; methods of physical modeling of weld metal heat treatment on small model samples [26], cut out of the actual rail welded joints.

The main investigation results can be applied in municipal transport and utility companies for construction and repair of tram rail tracks.

DILATOMETRIC STUDIES

In order to assess the influence of the thermal cycle of induction heat treatment on formation of the final structure of the HAZ metal in welded joints of K76F rail steel, made by AAW-CN method, research of model samples was conducted in the Gleeble 3800 system for simulation of the welding processes and thermomechanical treatment [27]. For this purpose, two types of model samples I and II 6 mm in diameter and 86 mm in length were cut out of the actual rail welded joint. Samples were ground and chemically etched in 4 % alcohol solution of nitric acid (Nital) to reveal the weld metal and the zones of its fusion with the rail base metal. In samples of type I their central part (area of study) coincided with the deposited metal of the weld, in type II the central part (area of study) coincided with the zone of fusion of the deposited and base metal of the rail (Figure 1). The weld metal proper is an alloy of the metal of ANPM-3 filler wire and rail base metal.

Table 1 gives the composition of the high-carbon rail steel K76F of R65 type rail used in the studies and metal of the weld produced flux-cored welding wire of ANPM-3 grade.

In order to study the kinetics of austenite decomposition, heating of the model samples was conducted under vacuum ($5.0\cdot10^{-4}$ mbar) by passing current due to Joule heat. The sample was placed horizontally and a change in the sample geometrical parameters was determined using a high-precision linear displacement sensor (linear variable differential transformer (LVDT) with a variable transfer ratio). The dimensions of the contact surface of the sensor probe with the sample were equal to 0.5–1.0 mm. Accelerated cooling of the sample occurred through application of cooling copper clamps due to heat conductivity. The thermal cycle was assigned by a program based on controlling the sample temperature in time, using a thermocouple of 0.9 mm diameter welded to it (Pt–Pt/Rh 10 % alloy). The clamps moved freely relative to each other along the longitudinal axis, which allowed avoiding thermal stresses (Figure 2).

Studies of welded joints on model samples were conducted by different thermal cycles of the process. The thermal cycles included the heating stage, isothermal holding stage in the austenitic region at the normalizing temperature and the cooling stage. The normalizing temperature was the same for all the modes of sample heat treatment, and it was equal to 900 °C. The average rate of sample heating up to the specified temperature was equal to 8 °C/s. After weld metal heating up to its transformation in the austenitic region, the samples were held for 70 s and cooled in keeping with the specified thermal cycle modes. To study the transformation thermokinetics of supercooled austenite of the weld metal, five thermal cycles were selected, which differed by the cooling rate v in

Table 1. Composition of high-carbon rail steel K76F and metal of the weld made by AAW-CN using ANPM-3 welding wire, wt.%

Material	Fe	C	Si	Mn	S	P	Cr	Ni	Cu	V	Mo	Al
K76F steel	97.737	0.80	0.32	0.96	0.010	0.010	0.03	0.04	0.033	0.051	0.008	0.001
ANPM-3 metal	94.937	0.30	0.40	1.20	0.015	0.015	0.50	1.40	0.033	0.100	0.350	0.750

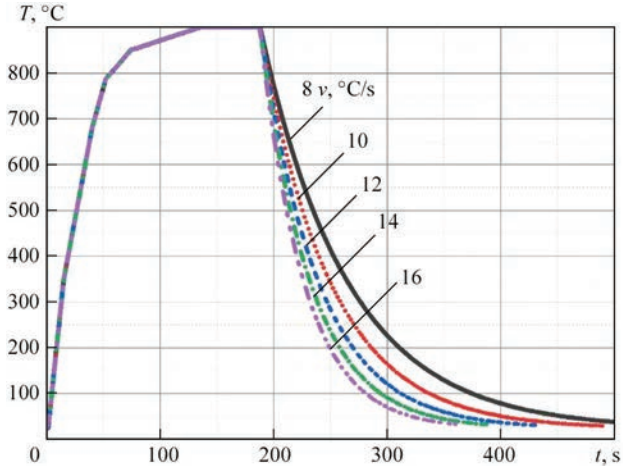

Figure 3. Thermal cycles in time (t) during a dilatometric study

the temperature range of 800–500 °C, and were equal to 8, 10, 12, 14 and 16 °C/s for each type of model samples, respectively (Figure 3).

The nature of sample cooling was non-linear, and it was assigned by Newton–Richman law, which corresponds to natural cooling of the metal [1, 28]:

$$T(t) = T_{o,s} + (T_{\max} - T_{o,s})e^{-rt},$$

where T is the sample temperature at moment of time t; $T_{0,s}$ is the ambient temperature; $T_{\max}$ is the maximal heating temperature, which is the initial cooling temperature; e is the natural logarithm base; r is the constant associated with material heat capacity (positive value).

Preparation of samples I and II with different locations of the weld zone relative to its center (Figure 1) is dictated by the task of studying austenite decomposition, both in the weld metal (Figure 1, *a*), and in the metal of the fusion zone (Figure 1, *b*). The complex geometry of the fusion zone and the fact that the measured width of the fusion line is equal to 0.4–0.5 mm and is smaller than the size of the contact surface of the sensor probe with the sample resulted in penetration into the dilatometer measurement zone of both the fusion line metal proper and the metal adjacent to the fusion line — cast weld metal and rail base metal.

Obtained parts of thermokinetic diagrams of supercooled austenite decomposition for the weld metal (samples of type I) and for the fusion zone metal (samples of type II) have a similar shape (Figure 4).

Based on the part of thermokinetic diagram for the metal of K76F steel welded joint made with ANPM-3 wire, it was determined that during heating of the samples at the rate of 8 °C/s the polymorphous α→γ transformation for samples of type I starts at the temperature of 715.2 °C (A_{c1}), and ends at the temperature of 884.6 °C (A_{c3}) and for type II these values are 733.0 °C (A_{c1}) and 870.4 °C (A_{c3}), respectively.

For weld metal (of type I samples) the start of the high-temperature (pearlitic) transformation falls within the temperature range of 600–630 °C and rises with a drop in the cooling rates: 16–8 °C/s. This transformation finishes at the temperature of 405 °C. In the case of the fusion zone metal (of type II samples) a certain increase in the temperature of the start of the high-temperature transformation is observed, compared to the weld metal. it is equal to 616–657 °C for the cooling rates of 16–8 °C/s, and it completes at temperatures of 545–553 °C for the above-mentioned rates. The temperatures of the start and end of the high-temperature transformation differ considerably for samples of type I and II, being equal to 195–225 °C and 71–104 °C, respectively, and for type I samples the high-temperature transformation zone is much longer than a similar zone for type II samples.

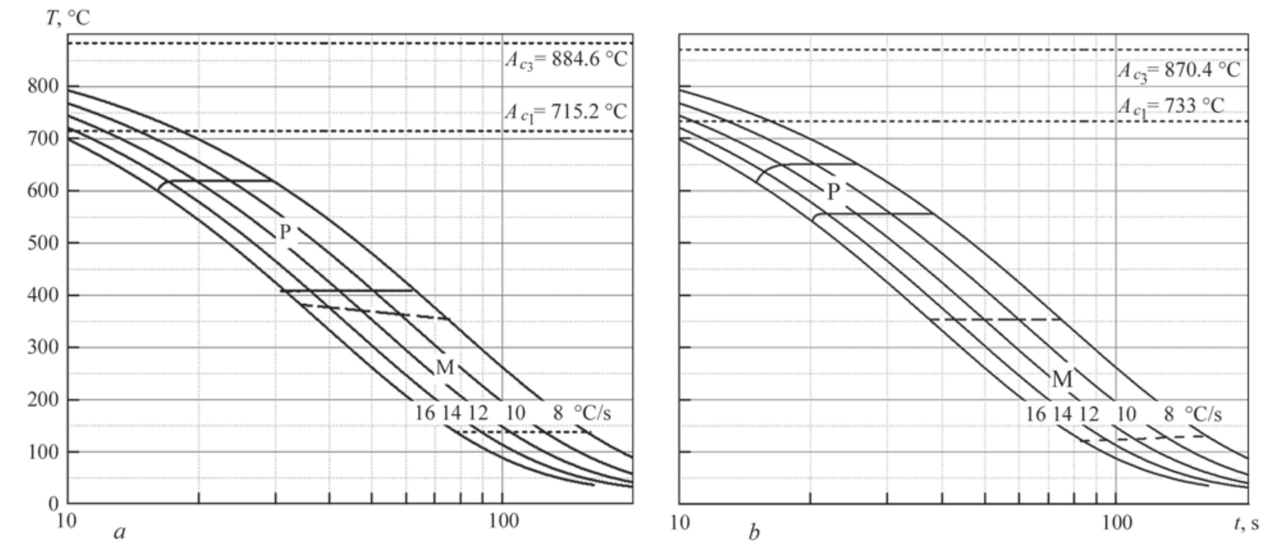

Figure 4. Sections of thermokinetic diagrams of supercooled austenite decomposition during continuous cooling of the metal of a K67F steel welded joint, made by AAW-CN using ANPM-3 wire: *a* — type I of model samples (weld metal); *b* — type II of model samples (fusion zone metal)

The start of the low-temperature (martensitic) transformation in type I samples falls within the temperature range of 369–351 °C, and it decreases with the drop in cooling rates — 16–8 °C/s. The low-temperature transformation completes at the temperature of 145 °C. For type II samples the temperature of the start of the low-temperature transformation is equal to 346 °C, and the temperature of the end of this transformation falls within the range of 122–140 °C, and it rises with the drop in the cooling rate of 16–8 °C/s, respectively. The difference in the temperatures of the start and end of the low-temperature transformation for the specified cooling rates is similar for samples of types I and II, being equal to 224–206 °C.

Such differences in the transformation pattern for the considered parts of the thermokinetic diagrams are probably associated with different chemical composition by carbon and alloying element content of the weld and fusion zone metal.

Increase in the metal volume in the region of the high-temperature (pearlitic) transformation is insignificant compared to its increase in the region of the low-temperature (martensitic) transformation and it is equal to 1–5 % of the latter.

During performance of the dylatometric tests the austenitization (normalizing) temperature was selected to be 900 °C. It was determined, however, that polymorphous transformation of model samples of type I finishes at the temperature of 884.6 °C (A_{c3}). It is obvious that this austenitization temperature may be insufficient for a complete dissolution of the primary metal structure and for the diffusion processes to proceed fully. Therefore, it is recommended to increase the austenitization temperature for type I samples by approximately 30–50 °C, so as to guarantee the transition of the metal into the austenitic region. The differences in the austenitization temperatures of type I and II samples may also lead to a certain change in the pattern of temperature transformations.

In the case of heat treatment of the rail welds by an inductor enclosing the rail, the metal region under the inductor center (in the axial direction of the rail), which corresponds to type I samples, will have a higher temperature than that at the inductor edges — in the zone of the weld metal fusion with the base metal of the rail, which corresponds to type II samples. Thus, the condition of ensuring an increased temperature for the weld metal and lower temperature in the zone of the weld metal fusion with the rail base metal can be met owing to the peculiarities of the inductor design (its width) and distribution of the temperature field under it.

MICROSTRUCTURAL AND HARDNESS LEVEL STUDIES

The microstructures of the base metal of a heat-hardened railway rail of R65 type from steel of K76F grade and of the weld metal were studied with a magnification of ×250. The base metal has a finely-dispersed pearlitic structure (sorbite-troostite type) with different degree of dispersity (Figure 5, *a*) with grain size number 7–9 and microhardness *HV* 0.1-2800–3200 MPa in the body of the rail head and up to *HV* 0.1-3510 MPa on the rolling surface. Integral hardness of the base metal is *HRC* 35–37 in the rail head at the depth of 5 mm from the rolling surface, and *HRC* 32–33 at the depth of 20 mm. Local hardness of the metal was measured by Vickers at the load of 0.1 kgf, and integral hardness was measured by Rockwell with TK-2M hardness meter at 150 kgf load.

The weld metal (Figure 5, *b*) has a cast ferritic-pearlitic structure with martensite inclusions. Integral hardness in the weld in the rail head at 5 mm depth from the rolling surface was *HRC* 29, and at 20 mm depth it was *HRC* 31, that is a lower hardness is observed in the weld in the rail head relative to the rail base metal. This is the prerequisite for the possible appearance of dips on the rolling surface in the weld zone during long-term and intensive operation of the tracks.

Metallographic investigations of the model sample metal after dylatometric testing were also conducted. The structural-phase composition of the welded joint metal was determined. Investigations of sample microstructure were conducted in the weld central part (type I samples) and in the fusion line

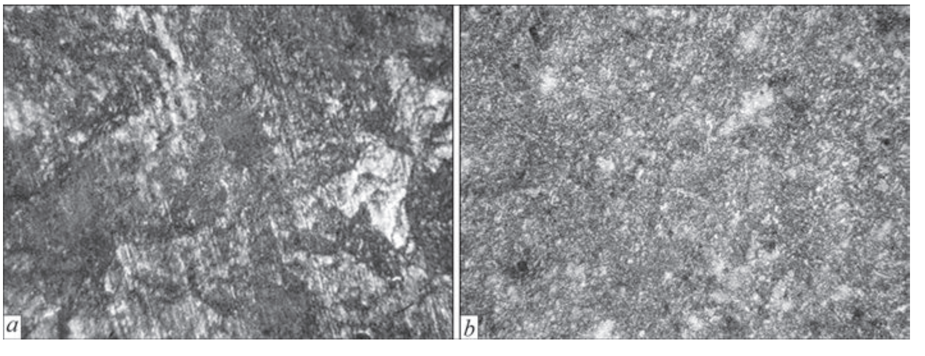

Figure 5. Microstructure of: *a* — base metal of the railway rail head; *b* — weld metal (×250)

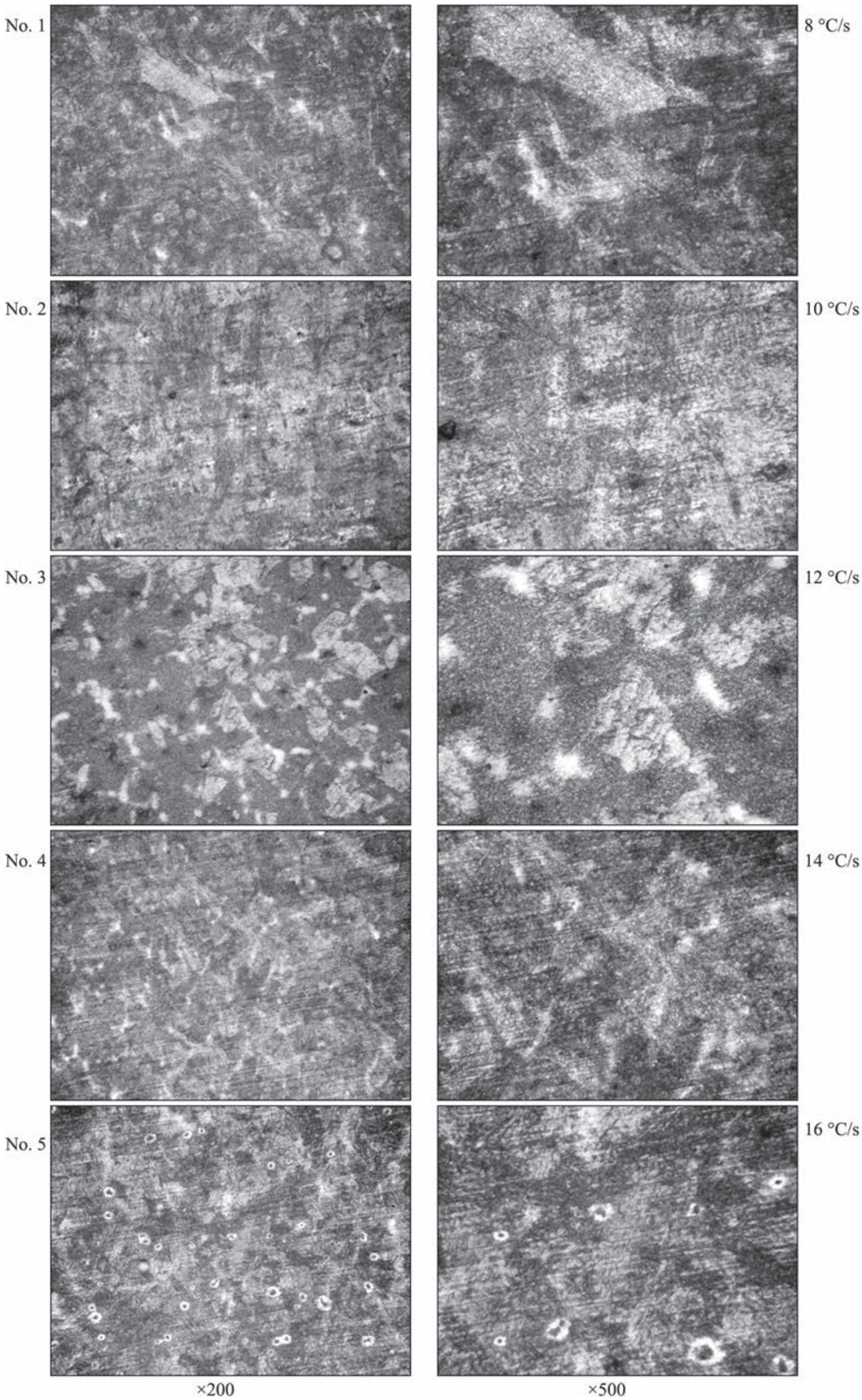

Figure 6. Microstructure of the central zone of the welded joint in type I model samples Nos 1–5, depending on the cooling rate during heat treatment (×200 and ×500)

area (type II samples) at magnification of ×200 and ×500, respectively.

Microstructure (Figure 6) of the studied samples of type I Nos 1–4 with the cooling rate of 8–14 °C/s is a pearlitic structure with microhardness within *HV* 0.1-3230–3840 MPa. Differences are found in sample No. 5 with the cooling rate of 16 °C/s, where an increase in the volume fraction of fine-acicular martensite with microhardness in the range of *HV* 0.1-4160–4510 MPa is observed.

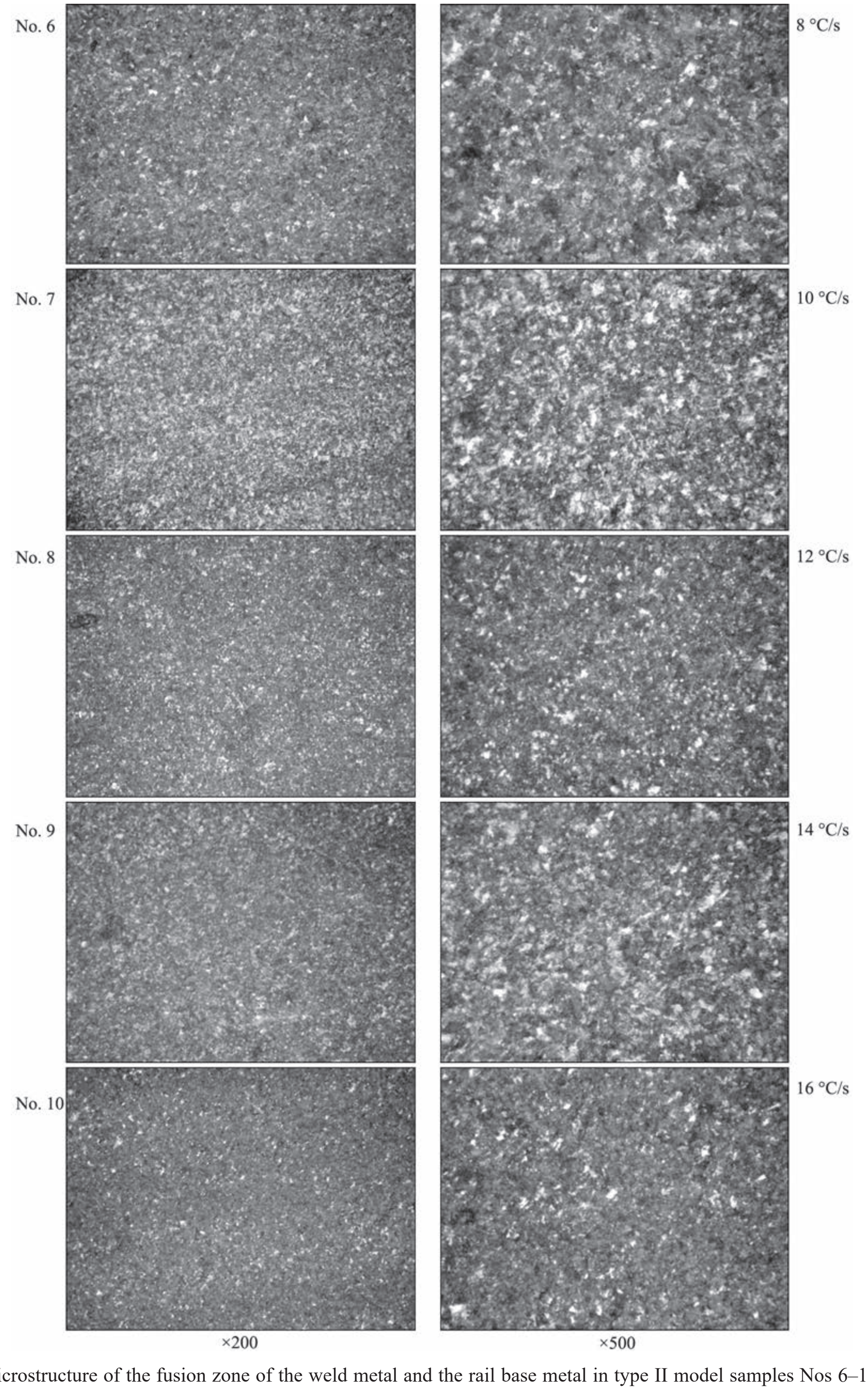

Figure 7. Microstructure of the fusion zone of the weld metal and the rail base metal in type II model samples Nos 6–10 of the first region (region shifted towards the weld metal), depending on the cooling rate during their heat treatment (×200 and ×500)

Investigations of the microstructure of type II samples Nos 6–10 were performed in the zone of the line of fusion of the deposited weld metal and base metal of the rail in two regions: first is shifted by 0.5 mm towards the weld metal (Figure 7), and the second one is shifted by the same distance towards the rail base metal (Figure 8).

The small size of the hardness meter indentation (~24–28 μm) allowed conducting local measurements of microhardness directly within the narrow fusion

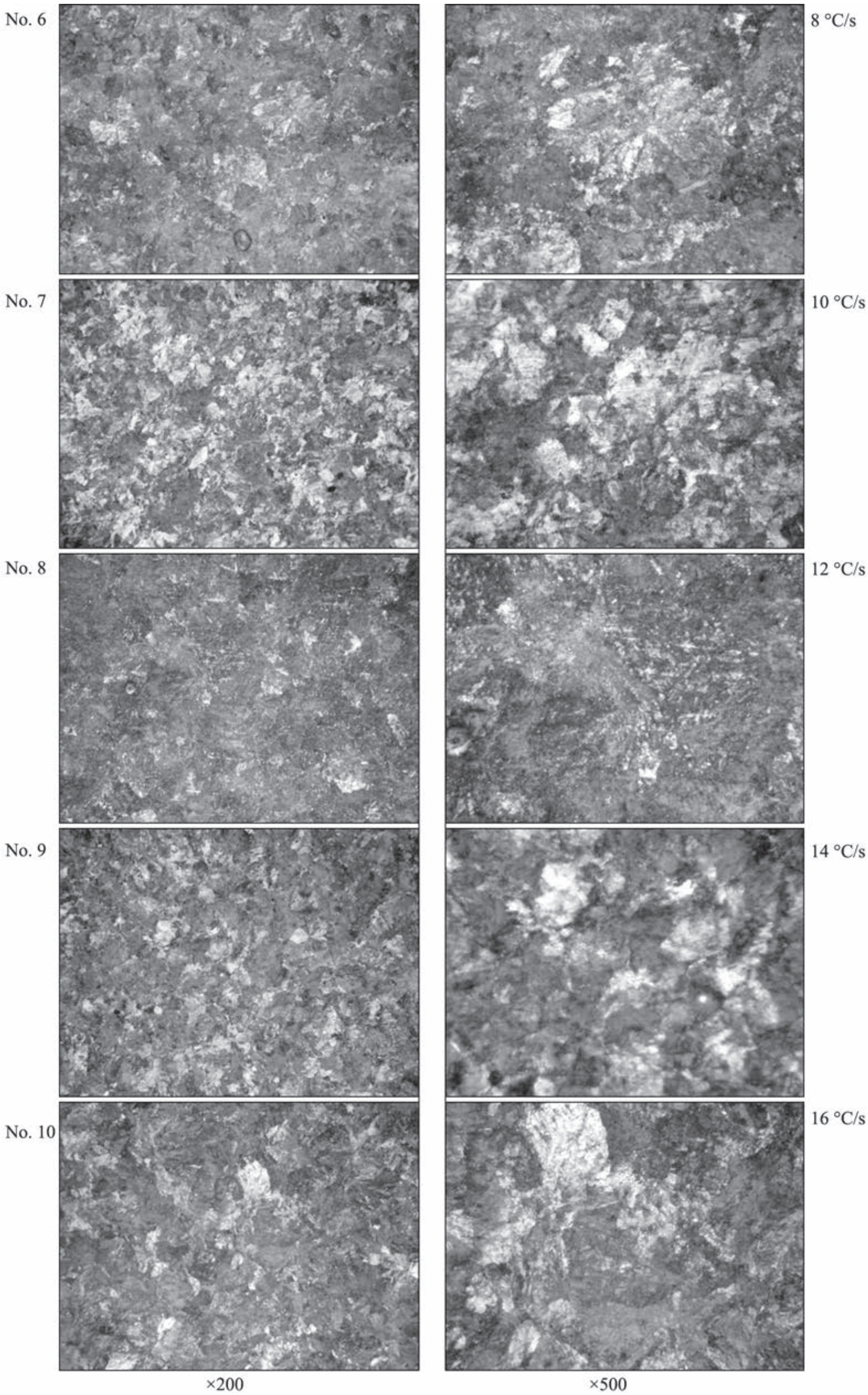

Figure 8. Microstructure of the fusion zone of the weld metal and rail base metal in type II model samples Nos 6–10 of the second region (region shifted towards the rail base metal), depending on the cooling rate during their heat treatment (×200 and ×500)

zone, while maintaining the required step within three diagonals between the indentations.

The microstructure of the studied samples of type II Nos 6–10 of the first region (Figure 7) with the cooling rate of 8–16 °C/s is a mixed ferritic-pearlitic structure with a small fraction of martensite of predominantly tempered type. Microhardness of the dark ferrite-pearlite phase is in the range of *HV* 0.1-2570–2900 MPa, and that of the light martensite phase is *HV* 0.1-4060–4260 MPa. Total microhardness of this region is in the range of *HV* 0.1-3680–3880 MPa. With increase of the cooling rate a tendency to increase in the microhardness of metal in this region is noticeable.

The microstructure of type II samples Nos 6–10 of the second region (Figure 8) is a predominantly pearlitic structure of different degree of dispersity with sites of free ferrite precipitation along the boundaries of former austenite grains. The total microhardness of this region is in the range of *HV* 0.1-3130–3480 MPa. With increase in the cooling rate a tendency to increase in this region microhardness is also observed.

Thus, heat treatment of the weld metal promotes an increase in its hardness the more, the higher the cooling rate.

Investigations of the structure of weld metal and fusion zone showed that application of cooling rates within 8–14 °C/s leads to formation of hardening structures in the weld metal, namely of tempered martensite regions, and at 16 °C/s it leads to formation of regions of fine-acicular martensite. It is anticipated that further rise of the cooling rate will promote an increase in the volume fraction of fine-acicular martensite component in the weld metal. Lowering of the cooling rate below 8 °C/s may lead to structural changes in the area of the fusion line and in the rail base metal, namely to an increase in the volume fraction of free ferrite, change in the pearlite component morphology, and carbide coagulation that will result in a considerable lowering of integral hardness of the metal in this region.

Formation of regions of quenched martensitic structures and presence in them of a fraction of tempered martensite in the welded joint metal after heat treatment is due to the features of the thermokinetic conditions of cooling from the austenite region. Rather high temperatures of the start of low-temperature martensite transformation (martensite start — M_s) are observed for the weld metal (type I samples) — 369–351 °C, and fusion zone metal (type II samples) — 346 °C. The low-temperature transformation is completed (martensite finish — M_f) for samples I and II, respectively, at temperatures of 145 °C and 122–140 °C, respectively (Figure 4). The longer time of the metal staying in the martensite transformation range (M_s–M_f), which is due to a significant difference in the temperatures of its start and finish of 224–206 °C at relatively low cooling rates of 14–8 °C/s, is sufficient for realization of local diffusion processes of carbon redistribution and precipitation from supersaturated solid solution of a certain quantity of finely-dispersed carbide particles in the martensitic matrix. In the case of high temperatures of martensite start M_s, the self-tempering phenomenon is realized in the steels, which consists in relaxation and tempering of the formed martensite without conducting separate stage of its repeated heating [29, 30]. Such an effect of hardening tempering is characteristic for the conditions of martensite formation at higher temperatures [31–33]. Increase in self-tempering intensity can provide an increase in material ductility with a comparatively small lowering of the strength level, which is typical for martensite.

In the studied samples, diffusionless nucleation and growth of martensite takes place. The martensitic structure stays in the temperature range of 350–300 °C for a certain time. Under these conditions, a limited diffusive redistribution of carbon within the martensitic structure becomes possible, predominantly along the dislocations, needle and packet boundaries, leading to partial lowering of supersaturation of the solid solution and precipitation of finely-dispersed transition carbide phases. It results in reduced tetragonality of the crystalline lattice of martensite and partial relieving of internal stresses. Thus, martensite forms in the weld metal, which underwent self-tempering at the initial stages. By its phase state and defect structure it corresponds to tempered martensite of low-temperature type, formed under the conditions of continuous cooling after austenitization, and differs fundamentally from martensite tempered by the classical high-temperature modes.

Presence of a fraction of hardening, predominantly self-tempered martensitic structures in the weld metal is not an obstacle in welded joints of tram tracks with relatively low loads on them, and low speeds of the rolling stock, unlike the modern high-speed railway tracks, where presence of the martensite component in the weld metal is not allowed.

Performed research showed that conducting the heat treatment of the welded joint metal of rails from K76F steel, produced by AAW-CN method with ANPM-3 welding wire with austenitization temperature of 930–950 °C and holding for 70 s at this temperature, ensures the weld metal transition into the austenitic region with formation of the pearlite component with individual regions of tempered martensite during its cooling with the rate in the range of 8–14 °C/s, which promotes an improvement of the metal structure of the welded joint.

Performance of induction heat treatment can increase the reliability of welded joints of tram track rails made by arc welding, which is important for construction and repair of the tram tracks.

Further research should be aimed at mechanical testing of the heat-treated welded joints of the actual rails.

CONCLUSIONS

1. Parts of thermokinetic diagrams of supercooled austenite decomposition during continuous cooling of metal of the weld, made by AAW-CN process with ANPM-3 wire and of the zone of its fusion with K76F steel were constructed for the first time. This allowed establishing the kinetics of phase transformations during cooling of the welded joint metal with determination of the influence of the cooling rates on formation of the final microstructure in the joint metal.

2. The modes of heat treatment of welded joints of heat-hardened rails of R65 type from K76F steel of tram tracks, welded by AAW-CN process by ANPM-3 wire were determined. In order to conduct heat treatment, it is necessary to achieve the temperature of weld metal austenitization of 930–950 °C at the heating rate of 8 °C/s with holding for 70 s at this temperature to produce a homogeneous austenitic structure and subsequent accelerated cooling in the range of 8–14 °C/s. It results in formation of the pearlitic metal structure in the welded joint with individual regions of tempered martensite.

3. The results of physical modeling on model samples of structure formation in the weld metal during heat treatment of the welded joints of tram rails showed that the process of heat treatment of the rail welded joint increases the quality characteristics of the joint metal, improves its structural homogeneity, increases its hardness and relieves the residual stresses. This can promote an extension of the operational life of welded joints of tram track rails.

REFERENCES

1. Krivtsun, I., Hubatiuk, R., Rymar, S. et al. (2025) Physical simulation of structural transformations in the welded joint of high-carbon rail steel. *Materials Research Express*, 12(**7**), 1–18. DOI: https://doi.org/10.1088/2053-1591/ade039
2. Krivtsun, I., Rymar, S., Hubatiuk, R. et al. (2024) Physical modelling of high-frequency induction heat treatment of welded joints of railway rails using inverter frequency converters. In: *Proc. of the IEEE 7th Inter. Conf. on Smart Technologies in Power Engineering and Electronics (STEE-2004), Kyiv, Ukraine, 24–26 September, 2024*. NTUU "Igor Sikorsky Kyiv Polytechnic Institute". DOI: https://doi.org/10.1109/STEE63556.2024.10747962
3. Gubatyuk, R.S., Rymar, S.V., Kostin, V.A. et al. (2021) The simulation of the process of heat treatment of welded joints of high-strength railway rails. In: *Proc. of the III Inter. Conf. on Advanced Technologies in Materials Science, Mechanical and Automation Engineering (MIP: III Engineering-III-2021)*, 2402(**1**), 070026. 070026-1–070026-7. American Institute of Physics, USA. DOI: https://doi.org/10.1063/5.0071364
4. Hubatyuk, R.S., Rymar, S.V., Prokofiev, O.S. et al. (2021) Modeling of the process of induction heat treatment of welded joints from rail high-strength steels. *The Paton Welding J.*, **9**, 27–38. DOI: https://doi.org/10.37434/tpwj2021.09.05
5. Hubatyuk, R.S., Rymar, S.V., Prokofiev, O.S. et al. (2021) Simulation of electromagnetic and thermal fields in the process of induction heating on small specimens with the presence of welded joint of high-strength railway rails. *The Paton Welding J.*, **1**, 40–44. DOI: https://doi.org/10.37434/tpwj2021.01.08
6. Gubatyuk, R.S. (2019) Heat treatment of welded joints of high-strength railway rails (Review). *The Paton Welding J.*, **2**, 41–48. DOI: https://doi.org/10.15407/tpwj2019.02.07
7. Ziakhor, I.V., Antipin, E.V., Didkovsky, O.V. et al. (2023) Modern technologies of welding railway rails (Review). *Avtomatychne Zvaryuvannya*, **5**, 5–17 [in Ukrainian]. DOI: https://doi.org/10.37434/as2023.05.01
8. Dahl, B., Mogart, B., Greford, B., Ulander, B. (1995) *Repair of rails on-site by welding*. ESAB Group, Goteborg, Sweden.
9. Poznyakov, V.D., Kiriakov, V.M., Gajvoronsky, A.A. et al. (2010) Properties of welded joints of rail steel in electric arc welding. *The Paton Welding J.*, **8**, 16–20.
10. Okumura, M., Karimine, K., Uchino, K, Yourioka, N. (1995) Development of field fusion welding technology for rail-road-rails. *Nippon Steel Technical Report*, **65**, 41–49.
11. Saita, K., Karimine, K., Ueda, M. et al. (2013) Trends in rail welding technologies and our future approach. *Nippon Steel and Sumitomo Metal Technical Report*, **105**, 84–92.
12. Kuzmenko, G.V., Kuzmenko, V.G., Galinich, V.I., Taganovsky, V.M. (2012) New technology of electric arc bath welding of rails on tram and crane tracks. *The Paton Welding J.*, **5**, 33–36.
13. Bajic, D., Kuzmenko, G.V., Samardzic, I. (2013) Welding of rails with new technology of arc welding. *Metalurgiya*, 52(**3**), 399–402.
14. Golovin, G.F., Zimin, N.V. (1979) *Technology of heat treatment of metals using induction heating*. Leningrad, Mashinostroyeniye.
15. Nesterov, D.K., Sapozhkov, V.E., Levchenko, N.F. et al. (1990) Heat treatment of rail steel using induction heating. *Metallovedeniye i Termicheskaya Obrabotka Metallov*, **8**, 30–34.
16. Lai, Z.Y., Lei, X.W., Zhang, Z.M. et al. (2023) Improvements in welding continuous cooling transformation diagram of high-strength low-alloy steel weld. *Materials Science and Technology*, 39(**17**), 2690–2698. DOI: https://doi.org/10.1080/02670836.2023.2215644
17. Minamoto, S., Tsukamoto, S., Kasuya, T. et al. (2022) Prediction of continuous cooling transformation diagram for weld heat affected zone by machine learning. *Science and Technology of Advanced Material*, **2**, 402–415. DOI: https://doi.org/10.1080/27660400.2022.2123262
18. Yu, S., Wang, Y., Zhang, Z. (2025) Monitoring process parameters and predicting rail steel welded joint microstructure and mechanical property of three-wire fusion nozzle electroslag welding. *Welding in the World*, **69**, 1229–1240. DOI: https://doi.org/10.1007/s40194-025-01962-2
19. Ma, R., Liu, X., Lv, Q., Wang, X. (2022) Effect of laser shock peening on fatigue properties of U75VG rail flash-butt welding joints. *Optics and Laser Technology*, **149**, 107889. DOI: https://doi.org/10.1016/j.optlastec.2022.107889
20. Pismenny, A.S. (2005) *Induction heating for welding and related technologies*. Ed. by B.E. Paton. Kyiv, PWI.
21. Xie, H., Leng, W., Li, M. et al. (2024) Preparation and wear properties of high-silicon high-vanadium wear-resistant alloy with nano-pearlite matrix and carbides composite structure. *J. of Materials Research and Technology*, **28**, 199–215. DOI: https://doi.org/10.1016/j.jmrt.2023.11.279
22. Masoumi, M., Tressia, G., Centeno, D.M.A., Goldenstein, H. (2021) Improving the mechanical properties and wear resistance of a commercial pearlitic rail steel using a two-step heat treat-

ment. *Metallurgical and Materials Transact. A*, **52**, 4888–4906. DOI: https://doi.org/10.1007/s11661-021-06432-0
23. Aglan, H., Ahmed, S., Prayakarao, K., Fateh, M. (2013) Effect of preheating temperature on the mechanical and fracture properties of welded pearlitic rail steels. *Engineering*, 11(**5**), 837–843. DOI: https://doi.org/10.4236/eng.2013.511101
24. Babachenko, O.I., Kononenko, H.A., Podolskiy, R.V. (2020) Justification of the choice of thermo-kinetic parameters of the cooled K76F steel to increase hardness across the rail head section. *Metals Science and Heat Treatment of Metals*, **4**, 30–37. DOI: https://doi.org/10.30838/J.PMHTM.2413.241120.30.688
25. Grigorenko, G., Kostin, V., Zhukov, V., Zuber, T. (2016) Peculiarities of structural transformations in HAZ metal of rail steel M76 joint produced by flash-butt welding. *J. of Physical Science and Application*, 5(**6**), 54–65. DOI: https://doi.org/10.17265/2159-5348/2016.05.009
26. Savitsky, M.M., Gubatyuk, R.S., Rymar, S.V. et al. (2006) *Method of physical modulation of the process of high-frequency heat treatment of a metal sample*. UA Pat., No. a201902347. Kyiv, PWI. Publ. 19.05.2021.
27. Grigorenko, G.M., Kostin, V.A. (2013) Modern possibilities of modeling austenite transformations in welds in low-alloy steels. *Sovremennaya Elektrometallurgiya*, **1**, 33–39 [in Russian].
28. Konstantinov, S.M. (2005) *Heat transfer*: A textbook for students of higher technical schools of the Ministry of Education and Science of Ukraine, NTUU "Igor Sikorsky Kyiv Polytechnic Institute". Kyiv, Politekhnika.
29. Bhadeshia, H.K.D.H., Honeycombe, R.W.K. (2017) *Steels: Microstructure and properties*. 4th Ed. Amsterdam, Oxford, Elsevier Butterworth-Heinemann.
30. Krauss, G. (2015) *Steels: Processing, structure, and performance*. 2nd Ed. ASM International, Materials Park, Ohio, 704. DOI: https://doi.org/10.31399/asm.tb.spsp2.9781627082655
31. Matsuda, H., Mizuno, R., Funakawa, Y. et al. (2013) Effects of auto-tempering behaviour of martensite on mechanical properties of ultra high strength steel sheets. *J. of Alloys and Compounds*, 577(**1**), S661–S667. DOI: https://doi.org/10.1016/j.jallcom.2012.04.108
32. Ramesh Babu, S. (2021) *The onset of martensite and auto-tempering in low-alloy martensitic steels*: Academic Dissertation of the Doctoral Training Committee of Technology and Natural Sciences of the University of Oulu, Finland. DOI: https://doi.org/10.13140/RG.2.2.20200.80644
33. Rupinen, M.C., Peterson, N.E., Clarke, A.J., Speer, J.G. (2024) Quantitative modeling of autotempering effects in martensitic steels, *Scripta Materialia*, **243**, 115998. DOI: https://doi.org/10.1016/j.scriptamat.2024.116001

ORCID

I.V. Krivtsun: 0000-0001-9818-3383,
R.S. Hubatyuk: 0000-0002-0851-743X,
O.S. Prokofiev: 0000-0003-4643-6611,
S.V. Rymar: 0000-0003-0490-4608,
E.O. Panteleimonov: 0000-0002-5569-9141,
V.A. Kostin: 0000-0002-2677-4667,
S.G. Hryhorenko: 0000-0003-0625-7010,
V.V. Zhukov: 0000-0002-3358-8491,
I.O. Goncharov: 0000-0003-2915-0435,
G.V. Kuzmenko: 0000-0001-6764-5389

CONFLICT OF INTEREST

The Authors declare no conflict of interest

CORRESPONDING AUTHOR

S.V. Rymar
E.O. Paton Electric Welding Institute of the NASU
11 Kazymyr Malevych Str., 03150, Kyiv, Ukraine
E-mail: elmag@paton

SUGGESTED CITATION

I.V. Krivtsun, R.S. Hubatyuk, O.S. Prokofiev, S.V. Rymar, E.O. Panteleimonov, V.A. Kostin, S.G. Hryhorenko, V.V. Zhukov, I.O. Goncharov, G.V. Kuzmenko (2026) Physical modeling of structure formation of the weld metal during heat treatment of tram track joints. *The Paton Welding J.*, **08**, 23–33.
DOI: https://doi.org/10.37434/tpwj2026.08.03

JOURNAL HOME PAGE

https://patonpublishinghouse.com/eng/journals/tpwj

Received: 24.12.2025
Received in revised form: 30.03.2026
Accepted: 29.07.2026

DOI: https://doi.org/10.37434/tpwj2026.08.04

THE INFLUENCE OF THE BASIC FEED DIRECTION OF THE GRINDING TABLE ON THE ABRASIVE WEAR RESISTANCE OF GROUND OVERLAY WELDS

M. Szymura[1], **O. Konoreva**[2], **O. Ganushchak**[2]

[1]Silesian University of Technology
Konarskiego Street 18A, 44-100 Gliwice, Poland
[2]E.O. Paton Electric Welding Institute of the NASU
11 Kazymyr Malevych Str., 03150, Kyiv, Ukraine

ABSTRACT

The article presents the results of the tests on the resistance to metal-mineral abrasive wear performed on hardfacing layers deposited using self-shielded flux-cored wire Fe–Cr–C (Fe15), with different weld bead orientations towards the basic feed direction of the grinding table. The significance of the above-mentioned effect was determined using a completely randomized design. The scope of the tests also included roughness measurements, surface topography studies, microscopic metallographic examinations, and microhardness measurements of the hardfacing layer.

KEYWORDS: surfacing, hardfacing, abrasion, grinding, flux-cored wire

INTRODUCTION

Wear processes limit the service life of machine and equipment parts. Welding technologies enable the application of abrasion-resistant layers and coatings [1–11].

Machining is often used in surfacing processes (the production of new components and the refurbishment of worn ones). This processing is performed both before (preparing the surface for hardfacing) and after (ensuring the desired dimensional and shape accuracy). The choice of machining method for hardfacing layers depends primarily on their machinability [3, 12–18].

Hardfacing layers with a chromium cast iron structure (alloys from the Fe14, Fe15, and Fe16 groups, according to EN 14700) are subjected to machining in industrial applications (e.g., overlay welds on guides in vertical ball-race mills) or for research purposes (e.g., to prepare their surfaces for determining abrasive wear resistance in accordance with ASTM G 65). Hardfacing using the above-mentioned alloys can be performed usually without or, less frequently, with preheating. In both cases, the hardfacing layers are difficult to machine. Cracks occur in hardfacing layers deposited without preheating, which means that grinding is the typical processing method in the industrial practice [12, 18, 19].

The properties of the ground surface layer are primarily the result of mechanical and thermal interactions occurring during the grinding process. Improper selection of grinding conditions can cause structural changes in the material and unfavorable geometrical changes in the surface structure, resulting in reduced operational properties of the machined part. One factor that can affect durability under abrasive wear conditions is the directionality of the component's surface structure [20–22].

Research [23] shows that the grinding process of laser-surfaced composite layers can lead to degradation of their surface (cracks, broken WC particles).

Research [24] on the effect of finishing on laser-surfaced layers of cobalt alloy (Stellite 21) shows that overlay welds subjected to grinding and burnishing have higher abrasion resistance in the pin-on-disc test than welds subjected to grinding alone. The same applies to their roughness and hardness.

The publications [12, 19, 25–29] are devoted to the abrasive wear resistance of hardfacing layers with a chromium cast iron structure. Most often, they focus on determining the abrasion resistance of the selected hardfacing layers according to the ASTM G 65 standard. In these studies, when grinding samples to achieve the appropriate dimensional and shape accuracy in accordance with the aforementioned standard, the direction of the basic feed motion was parallel to the direction of the beads, or its orientation was not specified. Therefore, an attempt was made to determine the effect of the direction of the basic feed motion in grinding hardfacing layers on their abrasive wear intensity.

The article presents the results of the tests on the resistance to metal-mineral abrasive wear of hardfacing layers deposited using self-shielded flux-cored wire Fe–Cr–C (Fe15), with different weld bead orientations towards the basic feed direction of the grinding table. The significance of the above-mentioned effect was determined using a completely randomized

Table 1. Chemical composition of the weld deposit of the surfacing material and hardness after surfacing [30]

Chemical composition of weld deposit, wt. %					Hardness of the third layer of the overlay weld, *HRC*
Fe	C	Cr	Si	Mn	
Rest	5.0	27.0	1.5	1.5	58–64

Table 2. Parameters of arc hardfacing using self-shielded flux-cored wire Hardface HC-O

Welding current, A	Arc voltage, V	Polarity	Electrode feed rate, m/min	Travel speed, cm/min	Heat input*, kJ/mm
~400	29.0	DDEP	4.3	50	1.114
*Heat input calculated in accordance with EN 1011-1, for $k = 0.8$					

design. The scope of the tests also included roughness measurements, surface topography studies, microscopic metallographic examinations, and microhardness measurements of the hardfacing layer.

OBJECTIVE OF THE STUDY

This study aimed at determining the effect of a selected grinding parameter (basic feed direction) on the abrasive wear resistance of chromium cast iron overlays. The data obtained can be used to optimize the grinding process and the utilization of the area of the overlay components (e.g., sheets overlaid with a wear-resistant layer).

TEST MATERIALS

For arc surfacing, a 2.8 mm diameter HARDFACE HC-O flux-cored wire from Welding Alloys was used, providing a high-alloy chromium cast iron Fe–Cr–C (Fe15) deposit. The chemical composition of the filler metal and the hardness after surfacing, as provided by the manufacturer, are presented in Table 1 [30]. HARDFACE HC-O wire is recommended for, among other things, protecting surfaces exposed to intense metal-mineral abrasive wear under moderate impact loads. The base material used was 300×200×15 mm plates cut from S355JR non-alloy steel sheet according to EN 10025-2.

TESTS

ABRASIVE WEAR RESISTANCE TESTS

The tests, aimed to identify the significance of the influence of the basic feed direction in the grinding process on the abrasive wear resistance of ground overlay welds were conducted using a completely randomized design. This made it possible to determine how significantly one input factor influenced the output factor [32]. The assumed significance level of influence was α = 0.05. The following values were assumed for the angle between the basic table feed direction and the bead deposition direction: 0°, 30°, 45°, 60°, 90°. For each angle value, six metal-mineral abrasion resistance tests were performed. 30 samples were hardfaced. Technological parameters for these tests are presented in Table 2. Hardfacing process was carried out in one layer. In accordance with the adopted assumptions and the randomization concept, the 30 samples were assigned consecutive natural numbers from 1 to 30 based on the order of their deposition — from earliest to latest. Then, a sequence of random numbers was obtained using a computer random number generator [31]. Using a generated sequence of numbers, marked overlay weld samples were randomly assigned to the appropriate values of the tested factor. The measurement scheme of the completely randomized design with account of the assumptions and assignment is shown in Figure 1 [32]. The individual samples with the abrasion-resistant overlay weld were sampled for specimens having dimensions of 75×25 mm, arranged so that the direction of the beads was parallel to the longer side of the sample. The location of cracks in the hardfacing layer of the samples was random. Cracks occurred in all samples. The cut samples were subjected to peripheral grinding with a grinding wheel on a flat surface grinding machine, using production values of the adjustable variables. During the grinding process, the grinding wheel performed a main motion at a constant rotational speed, a rectilinear periodic longitudinal feed during the transition, and a periodic infeed during the

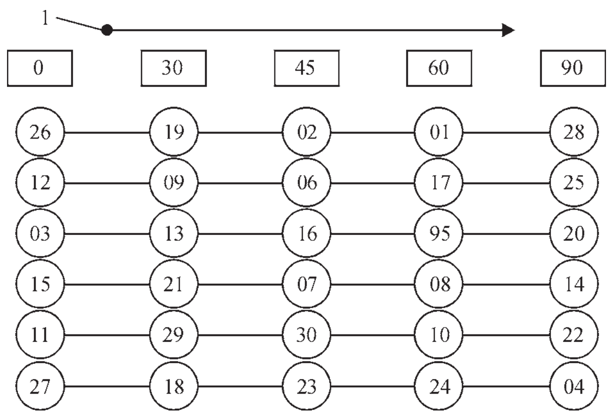

Figure 1. Scheme of measurements in a completely randomized design; 1 — the angle between the direction of abrasive particle movement and the direction of the basic feed movement

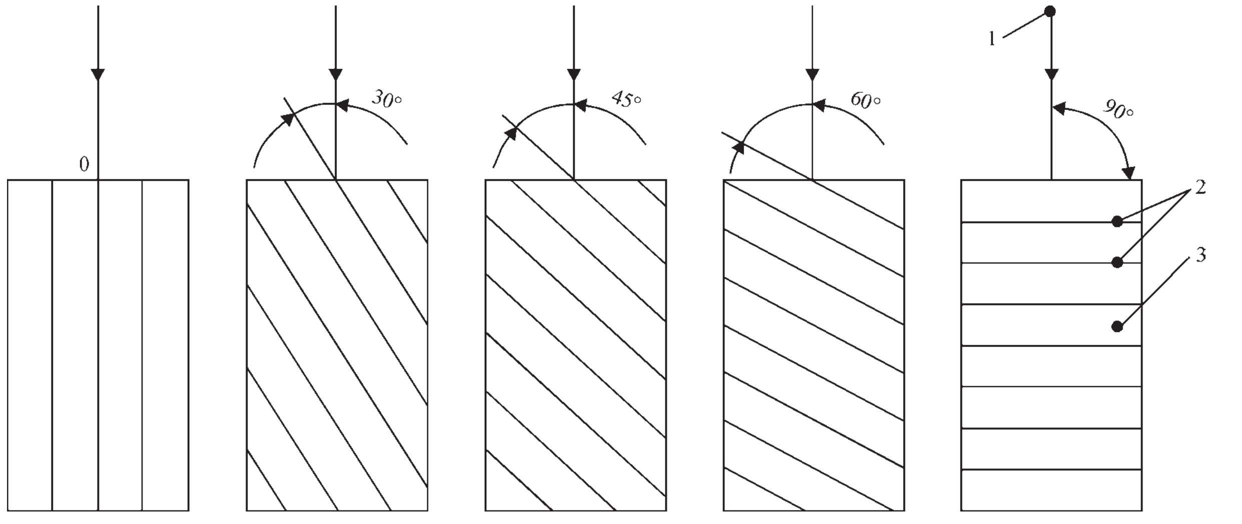

Figure 2. Alignment of samples with ground overlay welds relative to the direction of the primary feed motion and the direction of the abrasive particle movement; 1 — direction of the abrasive movement; 2 — direction of the primary feed motion; 3 — sample with ground weld deposits

infeed. The table on which the samples were mounted performed rectilinear and reciprocating motions. The samples were positioned so that the angle between the longer side of the sample and the direction of the feed movement of the basic table was: 0°, 30°, 45°, 60° and 90° (Figure 2).

The tests concerning the resistance of the deposited layer to the metal-mineral type of abrasive wear were performed in accordance with the ASTM G 65 standard, procedure A. During the test, the abrasive flow rate was 302 g/min. The samples were subjected to a constant force of 130 N. The rubber lined wheel rotated at a rate of 200 rpm, whereas the lineal abrasion amounted to 4309 m. Flame-dried quartz sand with spherical grain and a granularity of 100÷300 μm was used as the abrasive material. To determine the abrasive wear resistance of the overlay welds, the mass loss and density of the overlay weld were measured. Before and after the test, the samples were weighed using a laboratory balance, with an accuracy of up to 0.0001 g. The mean density of the weld was determined using a laboratory balance based on three density measurements of the surfacing layer of one sample, weighed in the air and liquid. The volume loss was determined using the sample mass loss values and the average measured density of the overlay weld according to formula (1). The obtained results are presented in Table 3.

$$V_l = \frac{M_l}{\rho} 1000, \qquad (1)$$

where V_l — volume loss, mm^3; M_l — mass loss, g; ρ — density, g/cm^3.

Table 3. Test results for the metal-mineral abrasive wear resistance of ground overlay welds

The angle between the direction of movement of the abrasive particles and the direction of the basic feed motion, °	Volume loss of the overlay weld, mm^{3*} (mass loss of overlay weld, g)						
	1	2	3	4	5	6	Mean value for individual levels
0	24.1387 (0.1767)	20.9830 (0.1536)	23.0731 (0.1689)	18.1279 (0.1327)	20.2317 (0.1481)	23.9065 (0.1750)	21.7435 (0.1592)
30	25.6960 (0.1881)	23.2917 (0.1705)	21.6661 (0.1586)	27.1031 (0.1984)	24.5676 (0.1798)	24.9447 (0.1826)	24.5440 (0.1797)
45	22.7589 (0.1666)	22.7316 (0.1664)	26.2834 (0.1924)	21.3246 (0.1561)	19.9995 (0.1464)	23.4010 (0.1713)	22.7498 (0.1665)
60	22.4311 (0.1642)	20.3000 (0.1486)	26.0375 (0.1906)	24.4119 (0.1787)	21.7617 (0.1593)	23.8381 (0.1745)	23.1301 (0.1693)
90	25.3408 (0.1855)	28.4965 (0.2086)	24.3982 (0.1786)	20.4503 (0.1497)	24.4939 (0.1793)	26.0512 (0.1907)	24.8718 (0.1821)
In relation to all results							23.4080 (0.1714)
*The loss of the volume of hardfacing layer was identified using formula (1). The measured density of the hardfacing layer is 7.3202 g/cm^3							

Table 4. Table of the analysis of variance

Source of variation	Sum of squares SS	Degrees of freedom DF	Mean square MS	Value of the test F
Between treatments	$SS_{Trt} = \sum_{i=1}^{K} r_i \bar{y}_i^2 - N\bar{y}^2 = 40.28516$	$fDF_{Trt} = K - 1 = 4$	$MS_{Trt} = \frac{SS_{Trt}}{K-1} = 10.0713$	$F = \frac{SS_{Trt}}{SS_E} = 2.0281$
Error (within treatments)	$SS_E = \sum_{i=1}^{K}\sum_{j=1}^{r_i} y_{ij}^2 - \sum_{i=1}^{r_i} r_i \bar{y}_i^2 = 124.14857$	$DF_E = N - K = 25$	$MS_E = \frac{SS_E}{N-K} = 4.9659$	–
Total	$SS_T = \sum_{i=1}^{K}\sum_{j=1}^{r_i} y_{ij}^2 - N\bar{y}^2 = 164.43372$	$DF_T = N - 1 = 29$	–	–

Note. r_i — number of measurements of the input factor at a given level; N — total number of measurements of the input factor; $\bar{y}_i$ — means of measurement results in the i-th line; $\bar{y}$ — mean of all measurements; y_{ij} — value of the j-th resultant factor at level i; K — number of variability levels of the test factor.

Table 5. Roughness measurement results for the surface of the ground overlay welds

The angle between the longer side of the sample and the direction of the basic feed motion,	Measurement along the sample		Measurement across the sample	
	Mean *Ra*, µm	Mean *Rz*, µm	Mean *Ra*, µm	Mean *Rz*, µm
0	0.108	0.862	0.154	0.945
30	0.182	1.109	0.164	1.104
45	0.159	0.996	0.148	1.203
60	0.161	1.116	0.180	1.096
90	0.204	1.284	0.129	0.888

The Table of the analysis of variance (Table 4) was made in accordance with the completely randomized design.

ROUGHNESS MEASUREMENT AND SURFACE TOPOGRAPHY TESTING

A Mitutoyo Surftest SJ-210 contact profilometer was used to measure the roughness parameters of the ground overlay weld surfaces. Roughness *Ra* and *Rz* measurements were taken along and across the samples in the areas where the cracks were not present. The mean results are presented in Table 5. Surface topography studies were performed using a Zeiss LSM 5 Exciter confocal microscope. The surface profilogram of ground sample no. 26 is shown in Figure 3, and the 3D image of the ground overlay weld surface of the same sample is shown in Figure 4.

MICROSCOPIC METALLOGRAPHIC TESTS

To determine the quality of the ground surface layer, microscopic metallographic examinations were performed. The metallographic examinations of sample number 26, whose angle between the longer side of the sample and the feed direction of the basic table is 0°, were performed on transverse and longitudinal metallographic sections using a light microscope. The results of the microscopic metallographic examinations are presented in Figures 5, *a* and 5, *b*.

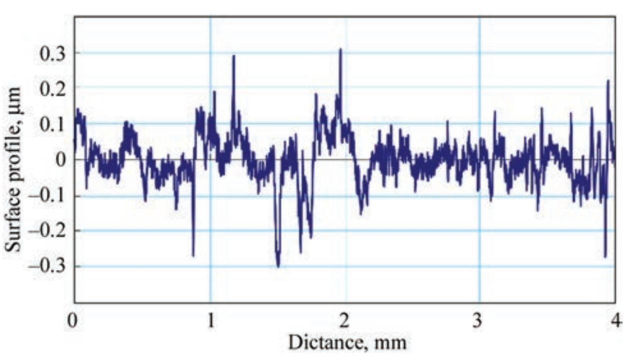

Figure 3. Profilogram of the surface of the ground overlay weld

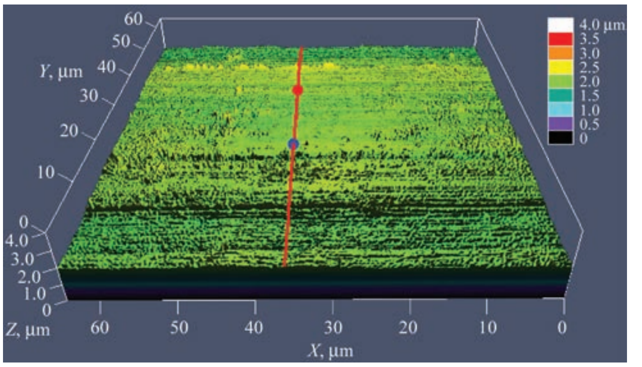

Figure 4. Surface topography of the ground overlay weld face

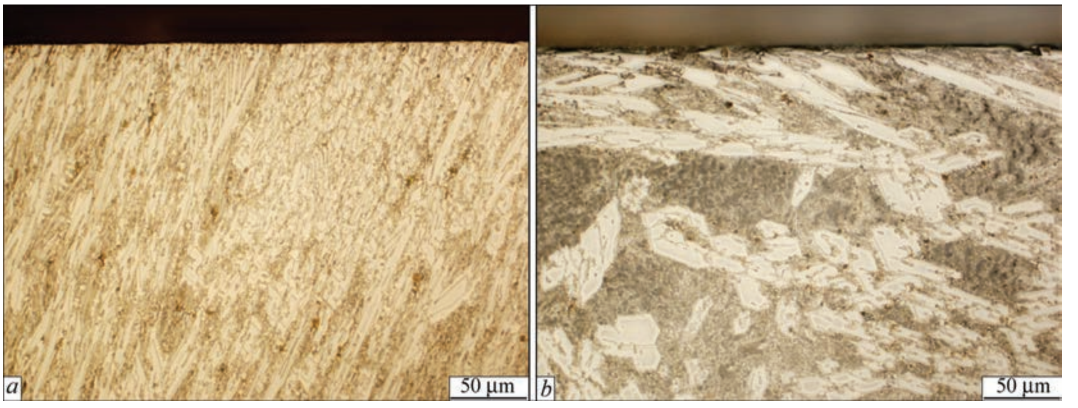

Figure 5. Microstructure of the ground overlay weld: *a* — on the transverse section; *b* — on the longitudinal section

HARDNESS MEASUREMENTS

Microhardness measurements of the surface layer were performed on the cross-sectional surface of sample no. 26 using the Vickers method. The first measurement was taken at a distance of 0.04 mm from the overlay weld face, and subsequent measurements were made every 0.04 mm. The microhardness measurement results are presented in Figure 6.

ANALYSIS OF TEST RESULTS

The tests carried out on ground hardfacing layers with self-shielded Fe–Cr–C (Fe15) flux-cored wire showed that, regardless of the direction of the basic table feed motion in the grinding process relative to the direction of the abrasive movement in the abrasive wear resistance test, the hardfacing layer is characterized by high abrasion resistance. The average volume loss of the overlay weld, determined based on ASTM G 65 for individual values of the basic motion direction angles, is in the range of 21.7435÷24.8718 mm^3. The effect significance test was conducted using a completely randomized

design. The F-test value calculation based on the statistical analysis of the test results (Table 4) is less than the critical value $F_{0.05;\,4;\,25}$ of the Fisher–Snedecor F-test [32]. This allows us to state that for the assumed significance level and the calculated numbers of degrees of freedom, the direction of the basic feed motion relative to the direction of movement of the abrasive particles has no significant effect on the resistance to metal-mineral abrasive wear of the ground overlay welds.

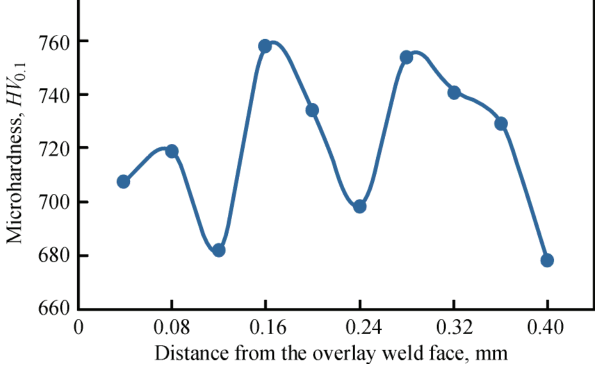

Figure 6. Results of *HV*0.1 microhardness measurements on the cross-sectional surface of the ground overlay weld

Roughness measurements taken on the face of the ground overlay welds demonstrate low surface roughness, typical for very precisely ground surfaces. The mean *Ra* roughness parameter values for the samples range from 0.108 to 0.204 µm and *Rz* roughness parameter from 0.862 to 1.284 µm. The lowest *Ra* and *Rz* parameter values were obtained during roughness measurements parallel to the direction of the primary table feed motion, while the highest values were obtained perpendicularly. The analyzed surface geometric structure is random, with noticeable microgrooves parallel to the direction of the primary feed motion. The height differences between the profile peaks and valleys range from approximately 2.5 to 6.0 µm.

In the ASTM G65 abrasive wear resistance test, cracking and fragmentation of the abrasive particles may occur and their impact on the test sample may be uneven. [33, 34]. The microgroove arrangement on the surface of ground overlay welds does not cause accelerated wear of the layers due to the abrasive's tendency to enlarge the microgrooves. The hardfacing layers exhibit uniform wear regardless of the abrasive particle's feed angle.

Based on microscopic metallographic examination, the hardfacing layer has a structure composed of large chromium carbides in an austenitic matrix. The metallographic examinations revealed no welding defects in the deposited layers.

In the case of turning of overlay welds with the structure of high-alloy chromium cast irons, degradation (cracking, deformation) of chromium carbides may occur due to the impact of the cutting edge on the cut material [16]. In the case of grinding of composite welds (Ni–WC), the matrix may crack and the tungsten carbide particles may crack, too [23]. The conducted tests did not reveal any degradation of chromium carbides or the matrix due to grinding.

The microhardness measured on the cross-sectional surface of the overlay weld is in the range of 678÷758 *HV*0.1. No hardness reduction was observed in the area of the face of the ground layer.

CONCLUSIONS

Based on the research conducted, the following conclusions can be drawn:

1. For the assumed significance level ($\alpha = 0.05$) and the calculated degrees of freedom, the direction of the primary feed motion relative to the direction of the abrasive particles has no significant effect on the resistance to metal-mineral abrasive wear of the ground overlay welds.

2. Layers welded with self-shielded Fe–Cr–C (Fe15) flux-cored wire are characterized by high abrasion resistance. The mean weld volume loss determined based on ASTM G 65 for individual values of the primary feed motion angle ranges from 21.7435 to 24.8718 mm^3. The lowest mean volume loss occurred for the parallel direction of abrasive movement in relation to the primary feed motion of grinding, whereas the highest value was recorded for the perpendicular orientation to the direction of the abrasive.

3. The tested layers are characterized by mean *Ra* roughness parameter values for the samples ranging from 0.108 to 0.204 µm and *Rz* roughness parameter values from 0.862 to 1.284 µm. This corresponds to a very precise grinding process. The microhardness measured on the cross-sectional surface of the overlay weld is in the range of 678÷758 *HV*0.1.

REFERENCES

1. Li, M., Li, M., Ma, D. et al. (2025) Effect of in situ (Ti, Mo)C on the microstructure and properties of FeMoSi/γ-(Ni, Fe) composite coatings by PTA cladding. *Materials Today Communications*, **49**, 113785. DOI: https://doi.org/10.1016/j.mtcomm.2025.113785
2. Łatka, L., Płatek, K., Szala, M. et al. (2024) Comparative study of metal-mineral abrasive wear resistance of hardfacing layers produced through different methods. *Quarterly Tribologia*, 307(**1**), 89–98. DOI: https://doi.org/10.5604/01.3001.0054.4658
3. Maksymov, S.Y., Babinets, A.A., Lentyugov, I.P., Osin, V.V. (2025) Welding and technological properties of sparsely alloyed flux-cored wires for strengthening and repair of parts by arc surfacing. *The Paton Welding J.*, **7**, 18. DOI: https://doi.org/10.37434/tpwj2025.07.03
4. Mirijanashvili, Z., Dadianidze, G., Tsagareishvili, O. et al. (2024) Obtaining wear-resistant coatings by surfacing with powder core welding wire. *The Paton Welding J.*, **10**, 26. DOI: https://doi.org/10.37434/tpwj2024.10.04
5. Poloczek, T., Lont, A., Górka, J. (2023) The structure and properties of laser-cladded inconel 625/TiC composite coatings. *Materials*, 16(**3**), 1265. DOI: https://doi.org/10.3390/ma16031265
6. Ryabtsev, I.O., Babinets, A.A., Ryabtsev, I.I., Lentyugov, I.P. (2025) Methods for increasing the fatigue life of deposited parts. *The Paton Welding J.*, **7**, 23. DOI: https://doi.org/10.37434/tpwj2025.07.04
7. Som, O.I. (2025) Iron-based binder alloy for plasma transferred-arc surfacing of composite alloys reinforced with cast tungsten carbides. *The Paton Welding J.*, **8**, 68. DOI: https://doi.org/10.37434/tpwj2025.08.09
8. Szala, M., Szafran, M., Macek, W. et al. (2019) Abrasion resistance of S235, S355, C45, AISI 304 and Hardox 500 steels with usage of garnet, corundum and carborundum abrasives. *Tribologia*, 284(**2**), 105–111. DOI: https://doi.org/10.12913/22998624/113244
9. Trembach, B., Dmitriiev, O., Kulahin, K. et al. (2025) Hybrid optimization of hardfacing conditions and the content of exothermic additions in the core filler during the flux-cored arc welding process. *Eng.*, 7(**1**), 23. DOI: https://doi.org/10.3390/eng7010023
10. Trembach, B., Krbata, M., Haibadulov, B. et al. (2026) Optimisation of elemental transfer efficiency in Fe–C–Cr–Ti–Cu hardfacing by self-shielded flux-cored wire: A synergistic taguchi–ANOVA–FD–PCA–GRA approach. *Eng.*, 7(**3**), 139. DOI: https://doi.org/10.3390/eng7030139
11. Turyk, E., Grigorenko, S.G., Ryabtsev, I.A. (2019) Mechanized surfacing of the end face of screw coils of a screw conveyor operating under abrasion conditions in a corrosive environment. *Welding Technology Review*, 91(**11**), 19–25. DOI: https://doi.org/10.26628/wtr.v91i11.1082
12. Czupryński, A., Kik, T., Melcer, M. (2018) Comparison of abrasion resistance of wear plates. *Welding Technology Review*, 90(**5**), 28–36. DOI: https://doi.org/10.26628/wtr.v90i5.893
13. Korzhyk, V., Grynyuk, A., Babych, O. et al. (2025) Obtaining functionally-graded metal-matrix materials Ti–6Al–4V+WC in the process of 3D printing by the method of additive plasma-arc deposition. *The Paton Welding J.*, **8**, 29. DOI: https://doi.org/10.37434/tpwj2025.08.03
14. Łyczkowska, K., Adamiec, J., Dolata, A. et al. (2021) Regeneration of aluminum matrix composite reinforced by SiCp and GCsf using gas tungsten arc welding technology. *Materials*, 14(**21**), 6410. DOI: https://doi.org/10.3390/ma14216410
15. Prokopov, V.G., Fialko, N.M., Sherenkovskaya, G.P. et al. (1993) Effect of coating porosity on the process of heat transfer with gas-thermal deposition. *Powder Metallurgy and Metal Ceramics*, 32(**2**), 118–121. DOI: https://doi.org/10.1007/BF00560034
16. Ren, X.J., James, R.D., Brookes, E.J., Wang, L. (2001) Machining of high chromium hardfacing materials. *J. of Materials Processing Technology*, 115(**3**), 423–429. DOI: https://doi.org/10.1016/S0924-0136(01)01029-9
17. Sydorets, V., Korzhyk, V., Khaskin, V. et al. (2017) Electrical characteristics of the equipment for the hybrid plasma-MIG welding. In: *Proc. of 58th Inter. Scientific Conf. on Power and Electrical Engineering of Riga Technical University (RTUCON), Riga, Latvia, 2017*, 1–6. DOI: 10.1109/RTUCON.2017.8124811
18. Szymura, M., Różański, M. (2019) The influence of positioning deposited beads direction to resistance on grind wear plates' abrasive wear. *Welding Technology Review*, 91(**5**), 11–17. DOI: https://doi.org/10.26628/wtr.v91i5.1030
19. Klimpel, A., Górka, J., Czupryński, A. (2006) Comparison of chromium cast iron deposits of wear plates. *J. of Achievements in Materials and Manufacturing Engineering*, 18(**1–2**), 387–390.
20. Grzesik, W. (2015) Wpływ topografii powierzchni na właściwości eksploatacyjne części maszyn. *Mechanik*, 88(**8–9**), 587–593. DOI: https://doi.org/10.17814/mechanik.2015.8-9.493

21. Kaczmarek, J. (1990) Analiza zmian i prognozowanie chropowatości powierzchni obrobionej w różnych odmianach szlifowania płaszczyzn. *Trybologia*, **3**, 22–25.
22. Packeisen, A., Theisen, W. (1999) Turning and grinding of hard alloys. *Advanced Engineering Materials*, 1(**1**), 35–48.
23. Dai, Q., Liu, L., You, F., Luo, C. (2022) Grinding performance of laser cladding WC/Fe coatings by different adding methods of WC particles. *Machines*, 10(**10**), 910. DOI: https://doi.org/10.3390/machines10100910
24. Uddin, M., Santifoller, R., Hall, C., Schlaefer, T. (2023) Effect of combined grinding-burnishing process on surface integrity, tribological, and corrosion performance of laser-clad stellite 21 alloys. *Advanced Engineering Materials*, 25(**8**), 2201332. DOI: https://doi.org/10.1002/adem.202201332
25. Mucha, T., Bartkowiak, K. (2011) Zastosowanie napawanych płyt trudnościeralnych w naprawach maszyn podstawowych górnictwa odkrywkowego. *Welding Technology Review*, 83(**10**), 73–76.
26. Poloczek, T., Czupryński, A. (2019) The analysis of the abrasive and erosive wear resistance of abrasion-resistant sheets. *Bulletin of the Institute of Welding*, **3**, 29–34. DOI: https://doi.org/10.17729/ebis.2019.3/2
27. Szymura, M., Czupryński, A. (2020) The effect of a welding technology on the abrasive wear resistance of joints in abrasion-resistant plates. *Bulletin of the Institute of Welding*, **64**, 49–60. DOI: https://doi.org/10.17729/ebis.2020.5/6
28. Szymura, M., Gąsiorek, G., Czupryński, A. et al. (2023) Comparison of wear resistance of overlay welded layers and thermal sprayed coatings in real conditions. *Materials*, 16(**22**), 7215. DOI: https://doi.org/10.3390/ma16227215
29. Szymura, M., Ochodek, V. (2023) Comparison of abrasive wear resistance of arc-sprayed and HVOF-sprayed coatings as well as overlay welds made using self-shielded flux-cored wire. In: *Proc. of 32nd Inter. Conf. on Metallurgy and Materials, Czech Republic, EU, May 17–19, 2023*, 492–499. DOI: https://doi.org/10.37904/metal.2023.4723
30. (2025) *Welding Alloys Company Catalog*. WA Consumables. Hardfacing.
31. RANDOM.ORG (2025) *Integer Sequence Generator*. https://www.random.org/sequences/?min=1&max=30&col=1&format=html&rnd=new
32. Kukiełka, L. (2002) *Podstawy badań inżynierskich*. Wydawnictwo Naukowe PWN, 40–42, 248.
33. Nahvi, S.M., Shipway, P.H., McCartney, D.G. (2009) Particle motion and modes of wear in the dry sand–rubber wheel abrasion test. *Wear*, 267(**11**), 2083–2091. DOI: https://doi.org/10.1016/J.WEAR.2009.08.013
34. Wang, Z., Sun, L., Wang, D. et al. (2024) Abrasive wear properties of wear-resistant coating on bucket teeth assessed using a dry sand rubber wheel tester. *Materials*, 17(**7**), 1495. DOI: https://doi.org/10.3390/ma17071495

ORCID

M. Szymura: 0000-0003-4571-4042,
O. Konoreva: 0000-0002-1597-6968,
O. Ganushchak: 0000-0003-4392-6682

CONFLICT OF INTEREST

The Authors declare no conflict of interest

CORRESPONDING AUTHOR

M. Szymura
Silesian University of Technology,
Department of Welding
Konarskiego Street 18A, 44-100 Gliwice, Poland
E-mail: mich.szymura@gmail.com

SUGGESTED CITATION

M. Szymura, O. Konoreva, O. Ganushchak (2026)
The influence of the basic feed direction of the grinding table on the abrasive wear resistance of ground overlay welds.
The Paton Welding J., **08**, 34–40.
DOI: https://doi.org/10.37434/tpwj2026.08.04

JOURNAL HOME PAGE

https://patonpublishinghouse.com/eng/journals/tpwj

Received: 29.04.2026
Received in revised form: 20.05.2026
Accepted: 31.07.2026

DOI: https://doi.org/10.37434/tpwj2026.08.05

CORROSION RESISTANCE OF MAGNETRON-SPUTTERED FeAl SYSTEM COATINGS

N.V. Vigilianska, K.V. Yantsevych O.V. Volos, V.G. Zadoya, B.T. Tkachenko

E.O. Paton Electric Welding Institute of the NASU
11 Kazymyr Malevych Str., 03150, Kyiv, Ukraine

ABSTRACT

The paper studies the electrochemical behaviour of FeAl-coatings with different aluminium content deposited by magnetron sputtering in various aggressive environments. The coatings were applied using a modified VU-1B vacuum installation with two targets of iron and aluminium. The coatings were deposited to stainless steel 08Khl8N10T with a thickness of 3 μm. The produced coatings predominantly consist of the FeAl intermetallic phase. The electrochemical behaviour of the coatings was studied in a potentiodynamic mode with 3 % sodium chloride and 10 % sulphuric acid solutions at a temperature of 18–20 °C. The corrosion current of magnetron FeAl-coatings is by an order of magnitude higher in a sodium chloride solution than in sulfuric acid, indicating better corrosion resistance in the latter. It has been shown that the coatings containing 55 at.% aluminium (Fe55Al) exhibit higher corrosion resistance compared to Fe40Al-coatings and even surpass that of 12Khl8N10T stainless steel. The improved resistance of Fe55Al-coatings is attributed to the presence of a single FeAl intermetallic phase and the absence of the α-Fe phase, the presence of which in Fe40Al-coatings corresponds to increasing corrosion processes. The obtained results demonstrate the suitability of using magnetron-sputtered Fe55Al-coatings as a protective layer for components operating in aggressive environments.

KEYWORDS: magnetron sputtering, coating, corrosion resistance, electrolyte

INTRODUCTION

One of the relevant areas for improving the service properties of products is the development of new materials, particularly those based on intermetallics [1]. FeAl-based intermetallics are among the promising intermetallic systems, distinguished by a range of unique physicochemical, mechanical and protective properties. These materials have a lower density unlike many other heat-resistant steels and alloys and can successfully replace expensive nickel-based intermetallic systems, namely Ni–Al and Ni–Ti. The high anticorrosion characteristics of iron aluminide-based materials ensure their resistance in various aggressive environments [2]. However, iron aluminides have not yet found widespread application in industry as structural materials due to the lack of a relatively simple and cost-effective method for their production. In this regard, iron-aluminium intermetallics (FeAl) represent a promising material for the development of protective coatings.

To produce FeAl-based coatings, thermal spraying methods are utilized, namely: plasma arc, detonation, electric arc, and high-velocity oxy-fuel spraying [3–7]. One method for depositing FeAl-based coatings in the form of thin films is magnetron sputtering [8–12]. This method of forming FeAl intermetallic coatings provides the formation of dense films with enhanced protective properties (wear resistance, resistance to high-temperature oxidation, and corrosion resistance).

THE AIM OF THE WORK

was to study the electrochemical behaviour of FeAl intermetallic coatings, produced by magnetron sputtering, in various aggressive environments.

RESEARCH OBJECTS AND EXPERIMENTAL PROCEDURE

Magnetron FeAl-coatings were deposited using a modified VU-1BS vacuum installation equipped with a direct-current magnetron sputtering module consisting of two magnetrons (Figure 1).

A target combining iron and aluminium components was installed on the first magnetron, and an aluminium target on the second one. The coatings were deposited on 08Kh18N10T steel. The composition of the coating was analyzed using a JUMP 9500 F Auger spectrometer. Electrochemical studies of the coat-

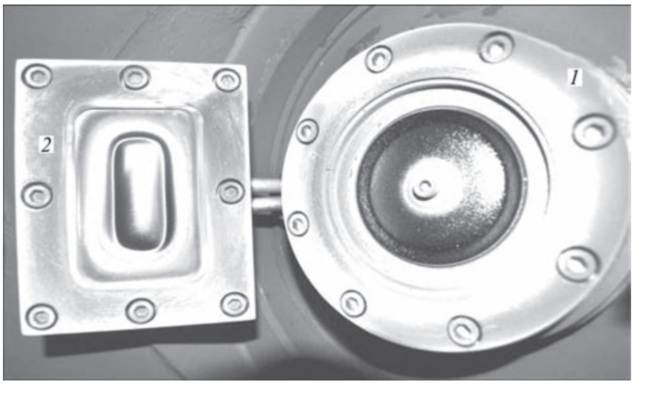

Figure 1. Layout of magnetrons in the vacuum chamber of the VU-1BS installation: *1* — magnetron made of a complex target (Al + Fe); *2* — magnetron made of an aluminium target

Table 1. Deposition parameters and characteristics of FeAl-coatings

Coating system	Magnetron power, W		Deposition rate, nm/min		Coating thickness, µm	Chemical composition of coatings (aluminium content), at.%	Phase composition of coatings
	P_{Fe}	P_{Al}	V_{Fe}	V_{Al}			
Fe40Al	830	1040	24	29	3	39.6	FeAl, α-Fe
Fe55Al	830	700	24	19.6	3	54.6	FeAl

Table 2. Results of electrochemical testing of coatings

Specimens	Electrolyte					
	3 % NaCl			10 % H_2SO_4		
	E_{st}, V	E_{corr}, V	i_{corr}, A/cm^2	E_{st}, V	E_{corr}, V	i_{corr}, A/cm^2
Fe40Al	–0.36	–0.32	$2.6 \cdot 10^{-6}$	–0.30	–0.26	$4.9 \cdot 10^{-5}$
Fe55Al	–0.34	–0.30	$1.2 \cdot 10^{-6}$	–0.24	–0.22	$1.4 \cdot 10^{-5}$
12Kh18N10T	–0.20	–0.18	$1.6 \cdot 10^{-6}$	–0.20	–0.22	$6.8 \cdot 10^{-5}$

$E_{st.}$ — stationary potential, V.

ings were carried out in model 10 % H_2SO_4 and 3 % NaCl solutions at a temperature of 18–20 °C [13]. To study the corrosion mechanism of steel with coatings in aggressive solutions, the voltammetry method was used in a potentiodynamic mode using a P-5827M potentiostat at a scan rate of 2 mV/s [13]. Potentials were measured relative to a saturated silver chloride reference electrode. Based on the data from polarization measurements, the potential (E_{corr}) and corrosion current (i_{corr}) were determined for coated steel [14].

EXPERIMENTAL RESULTS AND DISCUSSION

The coating deposition modes and their characteristics are given in Table 1. It was established that coatings with a dense structure are formed on the surface of the specimens, without any visible delamination from the substrate (Figure 2). According to the X-ray diffraction (XRD) data, the diffraction patterns of the Fe40Al and Fe55Al specimens exhibit distinct (110) and (200) reflections corresponding to the FeAl phase. The diffraction pattern of the Fe55Al specimen also contains an Fe (110) reflection. This can be explained by the fact that the aluminium content in the coating is 15.0 % lower than the lower limit of the compositional range of 47.3–54.0 at.% Al, within which the B2–FeAl phase is formed (Figure 3).

A study of the kinetics of electrode potentials showed that the electrode potentials of specimens with protective coatings stabilize after 20–30 min during immersion in electrolytes. The stationary potential of Fe40Al- and Fe55Al-coatings in a salt solution stabilizes at –0.36 and –0.34 V, and in a 10 % sulphuric acid solution at –0.30 and –0.24 V, respectively. Typ-

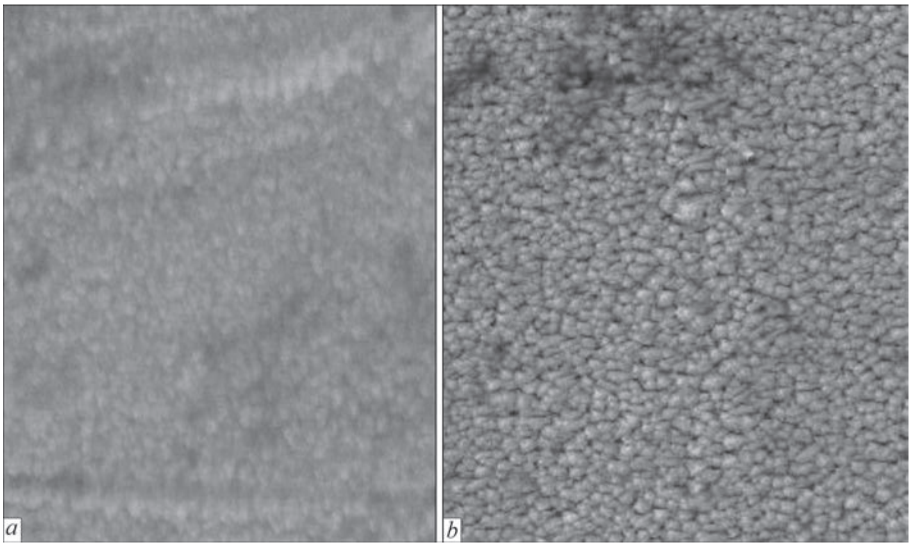

Figure 2. Surface microstructure (×10000) of FeAl-coatings, deposited on 08Khl8N10T steel: *a* — Fe40Al; *b* — Fe55Al

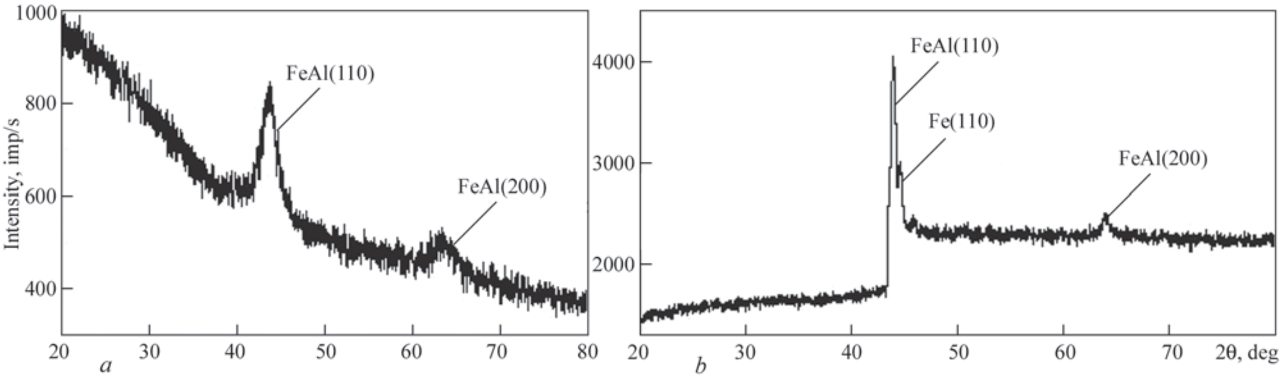

Figure 3. X-ray diffraction patterns: *a* — Fe55Al-coating; *b* — Fe40Al-coating

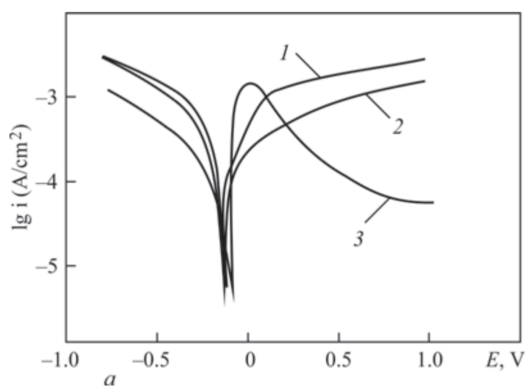

Figure 4. Polarization curves of magnetron FeAl-coatings in 10 % H_2SO_4 (*a*) and in 3 % NaCl solutions (*b*) at 20 °C at a potential scan rate of 2 mW/s: *1* — Fe40Al; *2* — Fe55Al; *3* — 08Khl8N10T steel

ical polarization curves of the coated specimens are shown in Figure 4.

Analysis of the polarization curves (Figure 4) showed that the shape of the curves and the nature of the electrochemical behaviour of coatings with different aluminium content are approximately the same for both salt and acid electrolytes. The corrosion process runs under cathodic control. The results of electrochemical tests of magnetron coatings in various electrolytes are given in Table 2.

It has been found that the resistance of coatings in a salt electrolyte is by an order of magnitude higher than in an acid electrolyte, which is determined by different pH values. It has been established that the corrosion resistance of coatings in electrolyte solutions depends mainly on their phase composition, specifically on the presence of the α-iron phase in the phase composition of the Fe40Al-coating, which accelerates the corrosion damage of the coating and reduces its resistance in aggressive electrolytes. Thus, the resistance of the Fe40Al-coating in a salt solution is 2.2 times lower than that of the Fe55Al-coating. In a more aggressive environment (in a sulphuric acid solution), the resistance of the Fe40Al-coating is 3.5 times lower than that of the Fe55Al coating.

The results of electrochemical tests showed that the Fe40Al system coatings are slightly inferior to 12Kh18N10T stainless steel in terms of corrosion resistance by a factor of 1.6 in a 3 % NaCl solution and by a factor of 2.5 in a 10 % H_2SO_4 solution. In turn, Fe55Al system coatings surpass stainless steel by a factor of 1.3 and 4.8 in a saline environment and in a sulphuric acid solution, respectively. Thus, it has been established that FeAl magnetron-sputtered coatings with an aluminium content of 55 % and a thickness of 3 μm can be used in aggressive environments (e.g., a 3 % NaCl solution) to protect the surfaces of machine parts and mechanisms. Electrochemical studies have shown that FeAl-coatings produced by magnetron sputtering are comparable in strength to plasma-sprayed FeAl-coatings in a salt electrolyte [7].

CONCLUSIONS

A 3 μm thick FeAl-coating was produced by the magnetron sputtering method with varying aluminium content, which was controlled by adjusting the deposition process parameters.

It has been shown that the corrosion resistance of FeAl-coatings depends both on the type of corrosive environment and on their phase composition. It has been established that coatings of the Fe40Al system exhibit lower corrosion resistance under the studied conditions compared to Fe55Al-coatings, which is attributed to the presence of the α-Fe phase. The obtained results make it possible to recommend coatings of the Fe55Al system, produced by magnetron sputtering, for the protection of surfaces of machine parts and mechanisms operating in environments exposed to salt electrolytes.

REFERENCES

1. Zamanzade, M., Barnoush, A., Motz, C. (2016) A review on the properties of iron aluminide intermetallics. *Crystals,* 6(**1**), 10. DOI: https://doi.org/10.3390/cryst6010010
2. Palm, M., Stein, F., Dehm, G. (2019) Iron aluminides. *Annual Review of Mater. Research*, **49**, 297–326. DOI: https://doi.org/10.1146/annurev-matsci-070218-125911
3. Guilemany, J.M., Cinca, N. (2007) High-temperature oxidation of Fe–40Al coatings obtained by HVOF thermal spray. *Intermetallics,* 15(**10**), 1384–1394. DOI: https://doi.org/10.1016/j.intermet.2007.04.013
4. Cinca, N., Guilemany, J.M. (2012) Thermal spraying of transition metal aluminides: An overview. *Intermetallics,* **24**, 60–72. DOI: https://doi.org/10.1016/j.intermet.2012.01.020
5. Borisov, Yu.S., Borisova, A.L., Vigilianska, N.V. et al. (2020) Coatings based on Fe–Al intermetallics produced by the methods of plasma and supersonic air-gas plasma spraying. *The Paton Welding J.*, **7**, 29–37. DOI: https://doi.org/10.37434/tpwj2020.07.04
6. Senderowski, C., Bojar, Z. (2008) Cas detonation spray forming of Fe-Al coatings in the presence of interlayer. *Surface Coatings Technology*, 202(**15**), 3538–3548. DOI: https://doi.org/10.1016/j.surfcoat.2007.12.029
7. Vihilianska, N.V., Gryshchenko, O.P., Iantsevitch, C.V. et al. (2022) Corrosion strength of plasma coatings based on composite powders with FeAl intermetallic. *The Paton Welding J.,* **12**, 35–39. DOI: https://doi.org/10.37434/tpwj2022.12.05
8. Cherif, S.M., Boussigne, K., Roussigne, Y. (2007) Growth and magnetic study of sputtered Fe/Al multilayers. *Materials Science and Engineering,* 138(**1**), 16–21. DOI: https://doi.org/10.1016/j.mseb.2006.12.009
9. Borisov, Yu.S., Kuznetsov, M.V., Tkachenko, B.T. et al. (2017) Investigation of process of formation of structure and properties in magnetron nanolayer FeAl-coatings. *The Paton Welding J.,* **8,** 24–29. DOI: doi.org/10.15407/tpwj2017.08.04
10. Stönner, T., Hanžel, D., Baretzky, B. et al. (1998) Characterization and oxidation of magnetron sputtered Fe–Al intermetallic alloys. *Hyperfine Interactions,* **112**, 155–160. DOI: https://doi.org/10.1023/A:1011017517588
11. Billard, A., Sanchette, F. (2001) Main features of magnetron sputtered aluminium-transition metal alloy coatings. *Surface and Coatings Technology,* **142–144**, 218–224. DOI: https://doi.org/10.1016/S0257-8972(01)01197-5
12. Liu, Z., Gao, W., Wang, F. (1998) Oxidation behaviour of FeAl intermetallic coatings produced by magnetron sputter deposition. *Scripta Materialia,* 39(**11**), 1497–1502. DOI: https://doi.org/10.1016/S1359-6462(98)00360-1
13. (2003) *ASM Handbook, Corrosion: Fundamentals, Testing and Protection*. Vol. 13A, 1135. ASM International.
14. Sahnenko, M.D., Vyed, M.V., Yaroshok, T.P. (2005) *Fundamentals of the theory of corrosion and protection of metals*. Kharkiv, NTU KhPI [in Ukrainian].

ORCID

N.V. Vigilianska: 0000-0001-8576-2095,
K.V. Yantsevych: 0000-0002-3975-7727,
O.V. Volos: 0000-0002-9073-2840,
V.G. Zadoya: 0000-0002-1286-985X,
B.T. Tkachenko: 0009-0008-6734-4242

CONFLICT OF INTEREST

The Authors declare no conflict of interest

CORRESPONDING AUTHOR

N.V. Vigilianska
E.O. Paton Electric Welding Institute of the NASU
11 Kazymyr Malevych Str., 03150, Kyiv, Ukraine
E-mail: pewinataliya@gmail.com

SUGGESTED CITATION

N.V. Vigilianska, K.V. Yantsevych, O.V. Volos, V.G. Zadoya, B.T. Tkachenko (2026) Corrosion resistance of magnetron-sputtered FeAl system coatings. *The Paton Welding J.*, **08**, 41–44.
DOI: https://doi.org/10.37434/tpwj2026.08.05

JOURNAL HOME PAGE

https://patonpublishinghouse.com/eng/journals/tpwj

Received: 10.02.20266
Received in revised form: 23.03.2026
Accepted: 28.07.2026

DOI: https://doi.org/10.37434/tpwj2026.08.06

IMPROVEMENT AND EXPERIMENTAL RESEARCH OF THE MAGNETOSTRICTION METHOD OF ULTRASONIC TESTING USING SMALL-APERTURE TRANSDUCERS

V.P. Babak[1], **I.V. Bohachev**[1], **O.L. Dekusha**[1], **S.I. Kovtun**[1], **Y.V. Kuts**[1,2], **S.V. Sozonov**[1]

[1]General Energy Institute of the NASU
172 Antonovych Str., 03150, Kyiv, Ukraine.
[2]National Technical University of Ukraine "Igor Sikorsky Kyiv Polytechnic Institute"
37 Prosp. Beresteiskyi, 03056, Kyiv, Ukraine

ABSTRACT

An analysis of publications on this topic showed an increase in the researchers' interest in in-depth study of the possibilities of magnetostrictive effects as a basis for the development of new methods of ultrasonic non-destructive testing (UNT). It was noted that a new promising direction of research is the creation of UNT methods and tools based on small-aperture magnetostrictive transducers (MST). Such transducers allow testing objects of complex geometry, in dry contact with MST and in a wide range of temperatures of control objects. The article is devoted to the development of UNT tools using MST, the action of which is based on the Joule and Villari effects, and the study of the possibilities of their application in UNT problems. In particular, the features of MST designs, their characteristics, and the peculiarities of signal formation of the emitting and receiving transducers are considered. For experimental tests, an original UNT system with a signal frequency of 0.5 MHz was used, which made it possible to evaluate the capabilities of the developed UNT method on test samples, which were metal plates with defects in the form of holes of different diameters, and by testing defects in welded joints.

KEYWORDS: ultrasonic non-destructive testing, magnetostrictive effects, small-aperture magnetostrictive transducers

INTRODUCTION

Ultrasonic non-destructive testing (UNT) is generally recognized as one of the most informative methods of investigation of the materials and structures [1, 2]. This kind of control is widely used in different industries, power engineering, transport industry, etc. In particular, the UNT methods are an important tool to ensure the reliability and safety of aviation equipment, beginning from development and investigation of aviation material characteristics [3, 4] and up to evaluation of the quality of aviation equipment structural elements in service [5].

Progress in development of information-measurement technologies and digital signal processing allows us to discover new capabilities of this testing method and widen the spheres of its application. All this contributes to the fact that development and introduction of new UNT technologies remains a branch of scientific research, which is growing dynamically. A lot of attention recently has been given to the issue of improvement of UNT methods based on magnetostrictive effects [6–8]. In work [9] a conclusion was made that within this field of study a promising approach is development of a UNT method and means based on small-aperture magnetostrictive transducers (MST).

THE OBJECTIVE

of the article is generalization of the authors' investigations aimed at upgrading the magnetostriction UNT method through optimization of MST design and improvement of the methods of MST signal formation and processing, as well as development of a laboratory stand on this base and conducting experimental research of the capabilities of this method.

ANALYTICAL SECTION OF THE ARTICLE

GENERAL CHARACTERISTICS OF JOULE AND VILLARI EFFECTS

Magnetostriction is understood as deformation of bodies during a change in their magnetic state, which is the most noticeably manifested in bodies of ferromagnetic materials and ferrites. In the case of magnetization of the bodies in an external alternating magnetic field their mechanical deformation develops: tension and compression, leading to generation of ultrasonic oscillations. The modern theory of magnetism provides this explanation of the phenomenon: under the impact of an external magnetic field the magnetic moments of the domains realign, orienting in the direction of the field, which leads to a change in the interatomic distances and distortion of the material crystalline lattice, accordingly.

The physical effect known as the linear magnetostriction effect, was discovered in 1842 by D.P. Joule, a known English physicist [11]. The essence of the Joule effect is illustrated in Figure 1, *a*. If electric current I is passed through an excitation coil, wound on a rod of magnetostriction material of length l and diam-

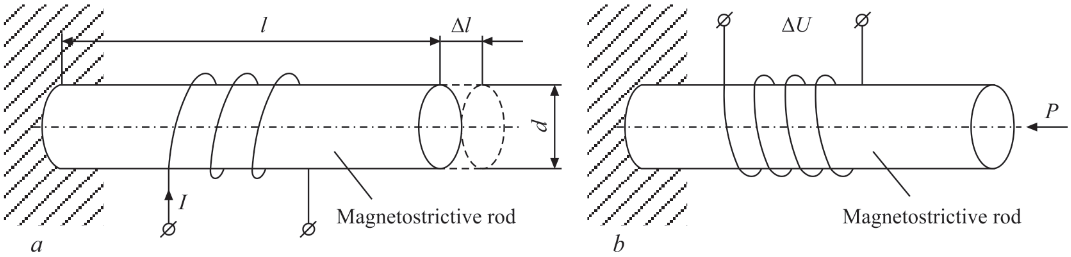

Figure 1. Illustration of the Joule and Villari effects

eter d, a longitudinal magnetic field is induced in the rod, under the impact of which the latter will change its length by value Δl. One of the main characteristics of the magnetostrictive material is the relative magnetostriction $\delta(B)$, which is defined by the following expression:

$$\delta(B) = \Delta l(B)/l, \tag{1}$$

where B is the magnetic induction in the rod.

Magnetostriction converts the alternating magnetic field into mechanical vibrations, which propagate as ultrasonic waves. Ultrasonic vibrations generated in this way can be used for nondestructive testing of materials. When the ultrasonic waves propagate through the material of the control object (CO), they are reflected from the defects or inhomogeneities, such as cracks or pores. The magnetostriction method enables receiving the waves reflected from the inhomogeneities or recording the changes in the acoustic path coefficient and thus detecting defects inside the material.

The magnetic state of the ferromagnetic is determined not only by the magnetic field, but also by external elastic stresses acting on the rod. Magnetoelastic effect, which is called an inverse magnetostrictive effect, occurs as a result of a relationship between the elastic stresses and change in the rod material magnetization. The inverse effect for linear magnetostriction is the magnetoelastic or Villari effect (Figure 1, *b*), which was discovered in 1895 by an Italian physicist E. Villari [9]. The effect is explained by the fact that the action of mechanical stresses in the rod material leads to a change in its domain structure, and, therefore in its magnetization, leading to generation of the electromotive force (EMF) ΔU in the electric coil. This effect is used in MST to receive the ultrasonic waves after their propagation in the CO.

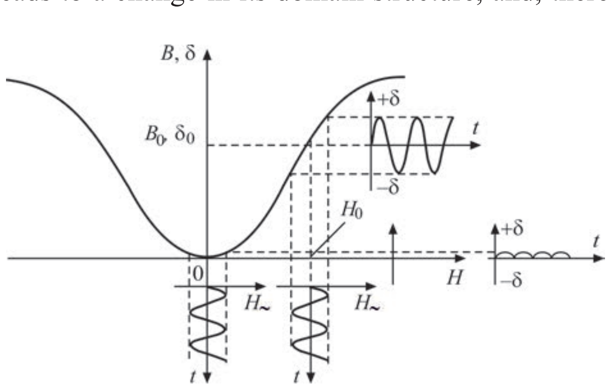

Figure 2. Dependence of the relative magnetostriction on the rod material magnetization

For practical application of the considered effects, we should take into account the nonlinear nature of the dependence between the magnetic induction and mechanical deformation in the magnetostrictive material [16], which requires additional measures for magnetostriction linearization. The latter is implemented by creating a constant magnetic induction in the rod material, which can be performed using permanent magnets or an additional coil, powered by direct current, or due to residual magnetization in the rod material. In the case of simultaneous action of the constant magnetic induction B_0 and variable magnetic induction $B_\sim$ mechanical vibrations arise in the rod, having the same frequency as $B_\sim$ frequency (Figure 2, where H_0 and $H_\sim$ are the intensities of the constant and variable components of the external magnetic field, respectively).

Magnetostriction linearization is aimed at deriving the magnetomechanical dependence of the magnetostrictive material from the quadratic zone, which is in place in the region of value $B_0 = 0$. If $B_0 \gg B_\sim$, there is a relationship close to a linear one between the mechanical and magnetic variables. These are exactly the two effects — Joule and Villari — which form the basis for MST development.

FORMULATION OF THE REQUIREMENTS TO MST AND THEIR IMPLEMENTATION

Different aspects of MST development were considered by the authors in [13–15]. The requirements to MST, their design features, and the associated specifics of MST signal formation, are generalized below.

REQUIREMENTS TO MST

During MST creation, it was necessary to solve a number of problems:

- select the magnetostrictive material for the waveguide;
- ensure a small aperture of the transducer;
- take measures to enhance the electromagnetic conversion coefficient;
- ensure magnetostriction linearization;

- minimize the MST-receiver noise;
- electrically match the converters with the electronic units.

A compromise between providing the best magnetostriction characteristics and the possibilities for MST practical implementation is using permendur 49KF alloy as the core material. This alloy has one of the highest magnetomechanical coupling coefficients among other materials. Other important characteristics of this material have the following values: density — ρ_p = +8200 kg/m^3; Young's modulus (longitudinal elasticity) — Y^Y = 2.0.5·10^{11} Pa; longitudinal wave length – c_l = 5200 m/s; relative magnetic permeability — μ^* = 200; coercive force — H_c = 140 A/m; saturation inductance — B_S = 2.4 T; specific electrical resistance — ρ_{el} = 3.4·10^{-7} Ohm·m; Curie temperature — θ = 980 °C; rational magnetization field — H_m = (0.4–0.6)·10^3 A/m.

In the presented development elastic vibrations of 0.5 MHz frequency are used, for which the wavelength in the permendur is equal to $\lambda_p = c_l/f$ = 5200/500000 = 10.4 mm. By MST aperture we mean its waveguide diameter. This is exactly the parameter which determines the area of the flat region on the CO surface, which is in contact with the MST waveguide, and through which the elastic wave energy is transmitted/received. The core diameter was chosen equal to d = 1 mm, which satisfies the condition $d_c \ll \lambda_p$, and the respective area of the contact region is 0.785 mm^2. This is precisely what gives reason to call such transducers small-aperture ones.

The coefficient of electromagnetic conversion is increased due to the use of a two-section excitation coil with the sections spaced at distance $\lambda_p/2$ (Figure 3), and connected in opposition. In this case, when the MST-emitter coil is powered by a radio pulse signal, the amplitude of the total current signal in the middle part is doubled, leading to a ~2 times increase in the variable component of the magnetic field in the waveguide without any increase in the excitation current amplitude. A negative side effect of such a technique is increase in the radio pulse duration.

Magnetostriction linearization is provided by means of the waveguide magnetization by a permanent magnet (not shown in the Figure). As the electrical coil on the ferromagnetic core is an antenna, the MST-receiver coil is also made of two sections (Figure 3), which reduces the influence of external electromagnetic interference and noise. The noise attenuation effect is explained by an equivalent electrical circuit (Figure 4), which incorporates the series-connected EMFs of the signal U_{s1}, U_{s2} and noise U_{n1}, U_{n2}, arising in the sections of MST-receiver coil and loaded to resistance R_1. The circuit was composed taking into

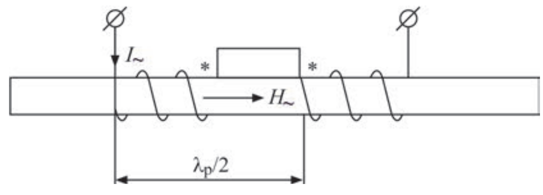

Figure 3. Electrical connection and arrangement of coils on the waveguide

account the opposite connection of the coil sections spaced at a distance of $\lambda_p/2$. The two-section design of the MST-receiver coil provides not only additional increase in the useful signal due to in-phase connection of EMFs U_{s1}, U_{s2}, but also considerable noise suppression due to anti-phase connection of EMFs U_{n1}, U_{n2}.

It was proved experimentally that the use of multilayer MST coils is inefficient. That is why the MST coils are made single-layer and have just a few dozen turns, while their electric impedance can be equal to 1–20 Ohm. Matching of MST low-impedance with the high-impedance of the electronic unit (usually equal to 50–8000 Ohm) is performed using transformers, located in the transducer near the MST coils.

MST DESIGN

The MST design as a whole is similar to the one given in [10–12] (Figure 5). The waveguide dimensions are as follows: 1 mm diameter, 60 mm length. In MST design the absorbing load *7* was introduced in order to prevent the re-reflection of ultrasonic vibrations from the nonworking end of the waveguide. The rest of the structure elements are determined by the requirements to MST considered earlier. Table 1 presents the results of measurement of MST coil parameters.

Measurements were performed using RLC impedance meter UNI-T UT-612. According to the data in Table 1, the impedance magnitude of MST coil does not exceed 4.2 Ohm, i.e. it is a low-impedance load. Transformers are used for matching the transducer to the system electronic units. Small dimensions of the contact region through which the ultrasonic vibrations are applied to the CO, are determined by the waveguide diameter, which allows performing investigations in CO with complex surface geometry.

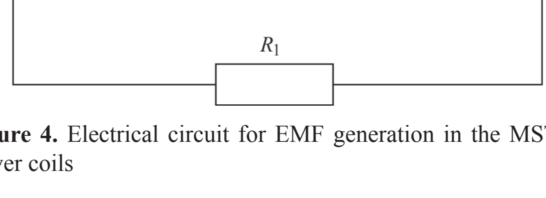

Figure 4. Electrical circuit for EMF generation in the MST-receiver coils

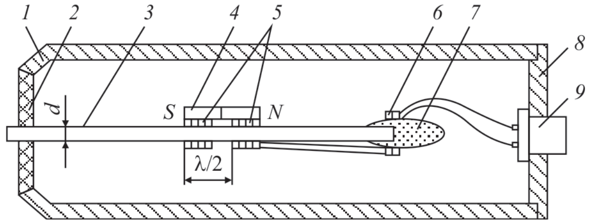

Figure 5. MST design: *1* — case; *2* — ultrasonic mirror; *3* — waveguide; *4* — permanent magnet; *5* — electrical coils; *6* — transformer; *7* — absorbing load, *8* — cover; *9* — connector

Table 1. MST coil parameters

Measurement object	Inductance, μH	Resistance, Ohm
One section of MST coil	12.3	0.38
Two section MST coil	8.2	0.72

GENERATION OF THE MST-EMITTER SIGNAL

Analysis of MST signals was performed to provide more substantiated requirements to the electronic units of the developed equipment. A radio pulse was taken as the excitation signal. The radio signal was obtained from harmonic voltage $\sin(2\pi ft)$, $t \in (-\infty, \infty)$ of 1 V amplitude and frequency $f = 0.5$ MHz, which is represented by the following model:

$$U(t, \tau) = I(\tau)\sin(2\pi ft), \quad \tau, t \in (-\infty, \infty), \tag{2}$$

where t is the carrier signal period ($T = 2$ μs), $I(\tau)$ is the indicator function:

$$I(\tau) = \begin{cases} 1, & \tau \in [0,\ 2T), \\ 0, & \tau \notin [0,\ 2T]. \end{cases} \tag{3}$$

In the discrete representation the signal (2) is provided as samples obtained with a sampling frequency of 64 MHz (128 points per the carrier signal frequency), the sampling period being 15.625 ns, respectively (Figure 6, *a*). The analyzed signal section (2) is limited by the range of $4T = 8$ μs.

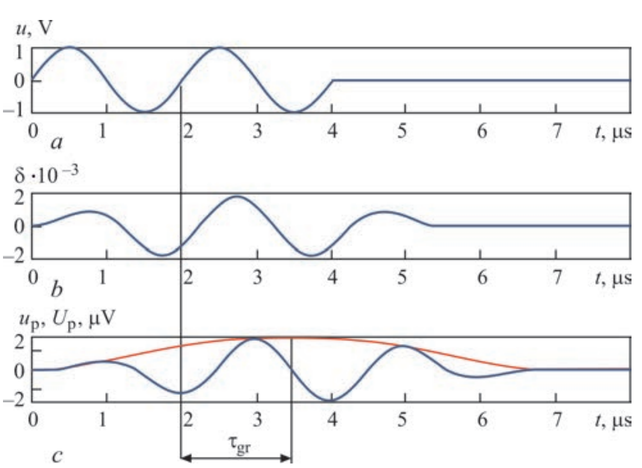

Figure 6. Graphs of MST model signals

Considering that the length of one excitation coil section is equal to $\lambda_p/4$ (i.e., it is comparable with the wavelength in the wave guide), the relative magnetostriction of the waveguide $\delta(t)$ was determined by superposition of the totality of actions of single-turn coils with different spatial positions. In the calculation model it was assumed that the excitation coil has 32 turns, and its length is $\lambda_p/4 = 2.6$ mm. Taking these data into account, and considering that the relative magnetostriction $\delta(t)$ as a function time is simultaneously generated by signals of two sections of the excitation coils (Figure 3), its analytical representation is as follows:

$$\delta(t) = K_{MC}\left[\sum_{g=1}^{32} I\left(t - \frac{T}{128}g\right)\sin\left(2\pi f\left(t - \frac{T}{128}g\right)\right) - \right.$$
$$\left. - \sum_{g=1}^{32} I\left(t - \frac{T}{64}\left(1 + \frac{g}{2}\right)\right)\sin\left(2\pi f\left(t - \frac{T}{64}\left(1 + \frac{g}{2}\right)\right)\right)\right], \tag{4}$$

where K_{MC} is the coefficient of voltage conversion into relative magnetostriction (in the performed model experiments $K_{MC} = 10^{-3}$ V^{-1} was assumed). The graph of $\delta(t)$ function is shown in Figure 6, *b*.

Deformation of MST rod (4) excites a short ultrasonic pulse (wave packet) in the CO, which propagates in it and which is converted into the respective electric signal in the MST-receiver. As this signal is close in shape to $\delta(t)$ function, a narrowband signal model can be used for its analytical representation [18], which in the general and in the digital form is given by the following expression:

$$u[j] = U[j] \cdot \cos(\Phi[j]), \quad j = \overline{1, J}, \tag{5}$$

where j is sample number; $U[j]$ is the signal envelope; $\Phi[j]$ is the signal phase (average frequency of the radio pulse carrier is close to f value).

During propagation of the ultrasonic wave in the CO, its envelope and phase are subject to modulation as a result of heterogeneity of the CO material characteristics and features of its geometry, so that $U[j]$ and $\Phi[j]$ functions acquire an informational content. Moreover, signal delay τ (5) relative to the MST-emitter excitation signal can be an information parameter (2).

MST-RECEIVER SIGNAL GENERATION IN THE ELECTROACOUSTIC CHANNEL

A feature of MST-emitter is the fact that it can be considered as point emitter in the first approximation [16]. During MST interaction with CO various types of waves can be excited in the latter, namely longitudinal, transverse, normal, etc., which have different properties [17]. MST practical application requires correctly taking into account the wave type, their excitation conditions, dispersion, velocity of their propagation in the CO, etc. In order to develop and substantiate the control procedures, it is particularly important to take reckon with the wave dispersion, i.e. dependence of their phase velocity c_{ph} on frequency. By phase velocity we mean the speed of displacement in space of a phase of harmonic vibration [17]. Phase velocity is expressed through frequency f, wave length λ and wave number $k = 2\pi/\lambda$ as follows:

$$c_{ph} = f\lambda = 2\pi f/k = \omega/k. \qquad (6)$$

The wave packet localized in time and space (Figure 6, *b*) propagates with group velocity c_{gr}. In the absence of dispersion $c_{gr} = c_{ph}$. The shorter is the wave packet, the wider its spectrum. In the presence of dispersion, the different frequency components of the wave packet propagate at different velocities, so that $c_{gr} \neq c_{ph}$, which, in particular, occurs when normal waves are used.

Let us consider two cases of propagation of an ultrasonic wave with velocity dispersion and without dispersion in the CO.

1. MST-emitter in the CO may excite the following wave types, which propagate in the CO without velocity dispersion [16]:

- longitudinal wave (tension-compression), propagating in the environment with the velocity of:

$$c_l \cong \sqrt{Y^{\mathrm{Y}}/\rho}\,; \qquad (7)$$

- transverse (shear) wave:

$$c_t \cong \sqrt{G/\rho}\,; \qquad (8)$$

- surface wave (Raleigh) wave:

$$c_R \cong \frac{0.87 + 1.12v}{1 + \mathrm{v}} c_t\,, \qquad (9)$$

where G is the shear modulus; ρ is the substance density, ν is the Poisson's ratio.

For these wave types no dispersion of the velocity is observed.

When these wave types are used in the MST-receiver, the elastic vibrations of the medium conversion into voltage occur in a manner similar to conversion in MST-emitters (only in the reverse direction). In the absence of velocity dispersion, the signal at the output of MST-receiver at discrete times $u_r(t) = u_r[(jT_d)]$, $j = \overline{1, J}$ and its envelope $U_r(t) = U_r[(jT_d)]$, $j = \overline{1, J}$, with the assumed in the model values of $K_{MC} = 10^{-3}$ V and acoustic channel coefficient $K_{ACh} = 1$, are shown in Figure 6, *c* (curves *1* and *2*, respectively). The signal envelope is determined using discrete Hilbert transform (DHT) [19], which is realized by operator $\mathbf{H}_d$. The latter provides the Hilbert-image of sample $\tilde{u}_r[j] = \mathbf{H}_d(u_r[j])$.

Signal envelope estimates for all the sample points are calculated as:

$$U_r[j] = \sqrt{u_r^2[j] + \tilde{u}_r^2[j]},\ j = \overline{1, J} \qquad (10)$$

Analysis of MST-receiver signal and of its envelope leads to the following conclusions:

- Maximal value of signal amplitude increased ~3.4 times.
- Received signal duration increased by one period and is equal to 3T.
- Center of the received signal envelope shifted in time by value $\tau_{sh} \approx 0.75T$ (without taking into account the delay in the transducer waveguides).
- The first and last half-waves of the received signal have a duration increased by value $0.125T$.

Fragment of the Fourier spectrum $X(f)$ of the obtained model of MST-receiver signals is presented in Figure 7 (spectral harmonic interval is 125 kHz). The established features of the model signals of MST-receiver should be taken into account during assessment of the actual signal parameters.

2. MST-emitter can excite normal waves (Lamb waves) in limited environment — plates and spheres. A CO which has two unloaded plane-parallel surfaces and thickness comparable with the length of the transverse wave. Lamb waves have the velocity dispersion [16, 20]. For instance, the propagation velocity of the phase of a harmonically regular symmetric zero-mode wave along the surface is equal to:

$$c_{Ns_0} = \frac{\pi h}{\lambda} \sqrt{Y^{\mathrm{Y}}/\rho} \qquad (11)$$

It is exactly the dependence of velocity c_{Ns_0} on the wave length (and hence, on ultrasonic vibration frequency) which is indicative of the dispersion of these waves velocity. In the wave packet propagating in the CO, vibrations of several components from the range around of the carrying frequency ω are present (Figure 6). In such a wave packet in a sufficiently narrow spectrum and under the condition of minor differences in the phase velocities of its harmonic components and not too large distances, the shape of the envelope wave packet is not distorted as noticeably, while the dispersion properties of the medium affect only the velocity of the envelope displacement in space, which is defined by the group velocity of the wave [17]:

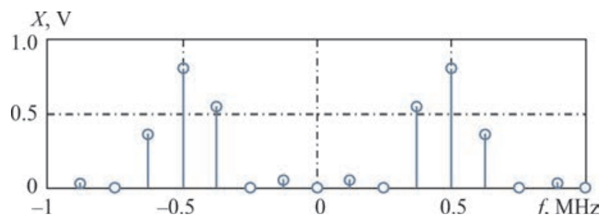

Figure 7. Fragment of the Fourier spectrum of MST-receiver signals

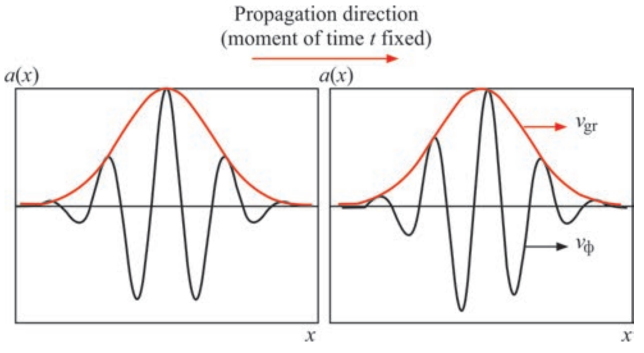

Figure 8. Wave packet propagation in a dispersion medium

$$c_{gr}(\omega) = \frac{d\omega}{dk}. \quad (12)$$

Here, the wave proper "runs" inside the respective phase with phase velocity $c_{ph} = \omega/k$ (6), which corresponds to the carrier signal frequency (Figure 8).

The relationship between the phase and group velocity of the wave packet is derived through differentiation of expression (12) with respect to k taking (6) into account:

$$c_{gr}(\omega) = \frac{d\omega}{dk} = \frac{d(c_{ph}k)}{dk} = c_{ph} + k\frac{dc_{ph}}{dk} = c_{ph} - \lambda\frac{dc_{ph}}{d\lambda}. \quad (13)$$

Relationship (13) confirms the fact that without the dispersion we have $c_{gr} = c_{ph}$. In the case of normal dispersion, i.e. provided the condition $c_{gr} < c_{ph}$ and the wave packet propagation in space ever new maximums and minimums will arise in its "tail" part, which with the change of distance x will move in the direction of its main part.

Unlike the monochromatic wave, the modulated wave (non-monochromatic) is capable of transmitting certain information, and this transmission is carried out with velocity of c_{gr}. This fact should be taken into account in the procedures of processing the MST-receiver signals using the Lamb waves.

EXPERIMENTAL PART

STRUCTURE OF A LABORATORY STAND FOR INVESTIGATION OF THE MAGNETOSTRICTIVE UNT METHOD WITH MST

Figure 9 shows the block-diagram of the laboratory stand for UNT with MST.

The stand provides generation of the MST-emitter signal, initial processing of the MST-receiver signals, extraction, analysis and saving of information parameters of these signals. The stand consists of an emitting and receiving MST fastened in a special holder, a unit for generation and preprocessing of MST signals and a hardware-software module. The first module incorporates: radio pulse signal generator, ensuring excitation of an acoustic wave in MST-emitter; amplifier of MST-receiver signals (sensor) and analog-digital converter (ADC). Digitized data are sent to the hardware-software module, where generation of the informative signal sample, its filtering, assessment of signal parameters, result displaying and their saving are performed.

Appearance of the laboratory stand for UNT with MST and a test sample are shown in Figure 10. The technical specifications are given below.

Main technical characteristics of the laboratory stand

Transducer working frequency, MHz	0.5
Probing pulse frequency, Hz	1–100
Emitter voltage, V	0–10 at 0.5 Ohm load
Probing pulse shape	Radio pulse
Amplifier gain	Up to 5000
ADC resolution	12 bits
ADC input impedance	1 MOhm resistance, 25 pF capacitance
ADC number of channels	2
ADC maximum sampling rate	200 MHz
System power source	230 V, 50 Hz

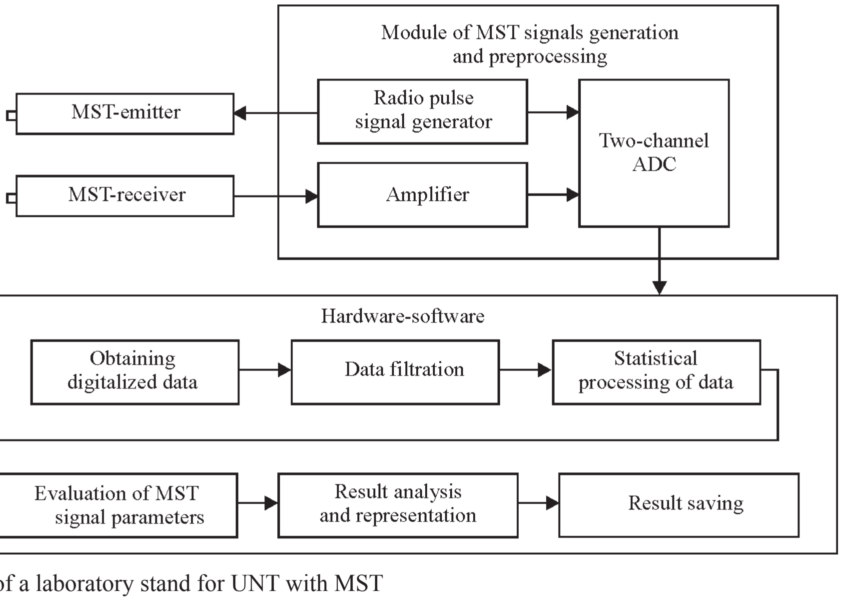

Figure 9. Block-diagram of a laboratory stand for UNT with MST

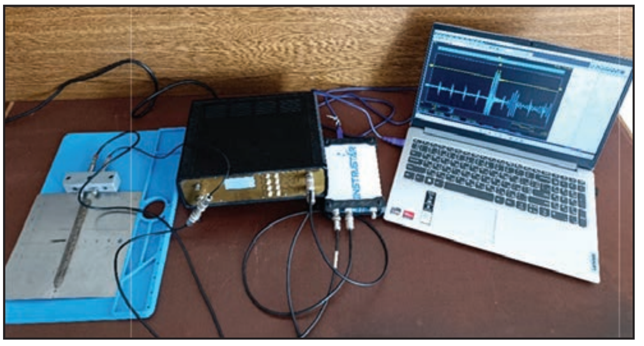

Figure 10. General view of a laboratory stand for UNT with MST

EXPERIMENTAL STUDY OF THE CAPABILITIES OF THE MAGNETOSTRICTIVE UNT METHOD ON TEST SAMPLES

We investigated ultrasonic wave propagation in samples of steel 3 in the form of plates of different thicknesses with the dimensions of 100×50×1 mm, 100×50×2 mm, 100×50×2.5 mm, in order to establish the dependencies between the plate thickness and the characteristics of the measured MST-receiver signal. During testing the signal amplitude was determined in the case of its propagation in the plate to a fixed distance of 25 mm, at which two MST were installed. The fragments of the obtained signals and the dependence of the maximal value of their amplitude on sample thickness are given in Figures 11, 12, respectively.

Analysis of the graph in Figure 12 showed that the measured signal amplitude decreases in proportion to the increase in the studied sample thickness. Such a dependence can be used to assess the corrosion damage of thin-walled cylinders and pipelines.

Investigation of ultrasonic wave propagation was conducted on a test sample made of steel 08kp (rimmed) 200×200×0.5 mm in size (Figure 13), which had artificial defects (holes) of different diameter (1, 2, 3 mm). The shadow UNT method was used [2, 16], with the defect located in the middle between MST-emitter and MST-receiver, spaced at 25 mm.

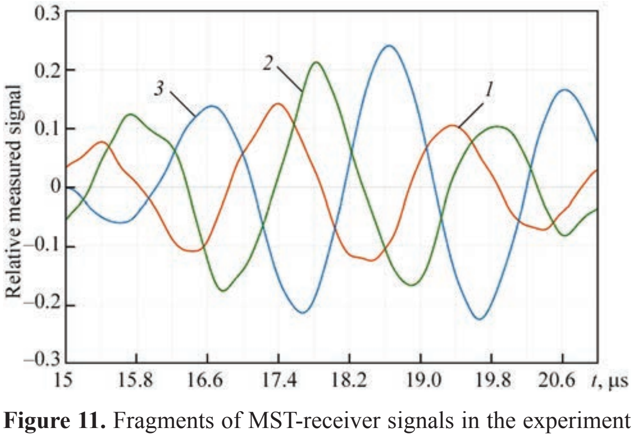

Figure 11. Fragments of MST-receiver signals in the experiment with steel 3 plate of the following thickness: *1* — 2.5; *2* — 2; *3* — 1 mm

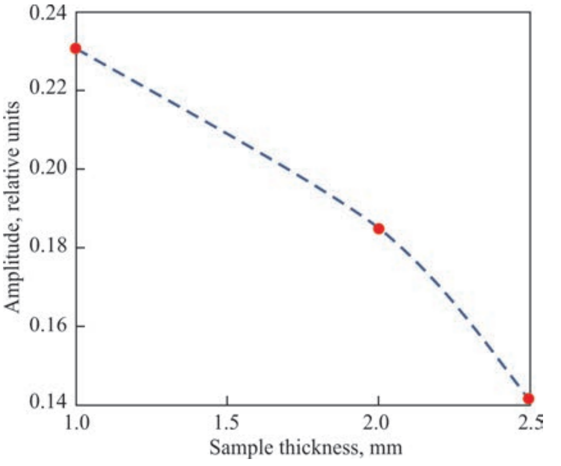

Figure 12. Dependence of maximal amplitude of MST-receiver signal on sample thickness

Fragments of the obtained signals of MST-receiver during testing of the test sample areas with holes of different diameter are given in Figure 14, and Figure 15 is a dependence of the signal amplitude on the holes diameter.

Analysis of the data in Figures 14, 15 showed that the measured signal amplitude decreases in proportion to the increase in the hole diameter (1, 2, 3 mm). This result is important to confirm the possibility of application of the shadow method with the proposed MST in the problem of detection of defects of the type of voids in thin sheets in the case of defect size smaller than the length of the wave in the sample, as well as in the problem of testing thin sheet welds. In this case, the amplitude of the MST-receiver signal, as an informational feature, turned out to be sensitive to defect size.

VERIFICATION OF UNT METHOD USING MST IN THE PROBLEM OF DEFECT CONTROL IN METAL SHEET WELDED JOINTS

Experimental studies were conducted on samples of thin metal sheets with a weld without a defect (Figure 16, *a*) and with a defect (Figure 16, *b*). Shadow

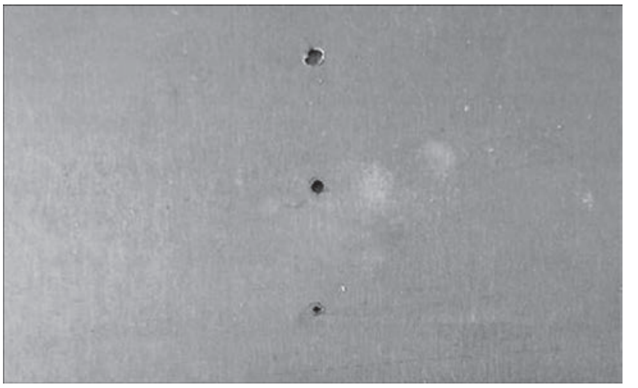

Figure 13. Test sample of steel 08kp (rimmed) with artificial defects — holes of 1, 2, 3 mm diameter

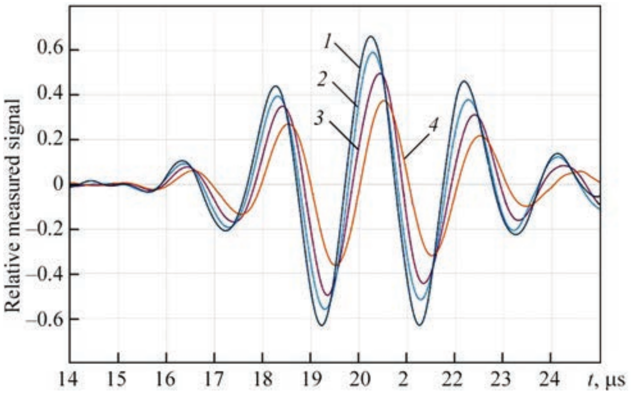

Figure 14. Fragments of MST-receiver signals in a sample of steel 08kp (rimmed) with holes of different diameter: *1* — isotropic; *2* — 1 mm hole; *3* — 2 mm hole; *4* — 4 mm hole

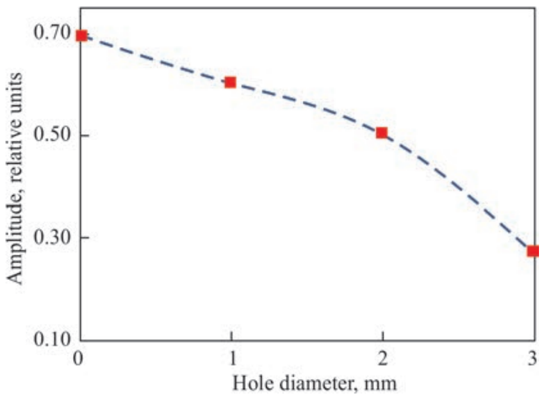

Figure 15. Dependence of signal amplitude of MST-receiver on hole diameter

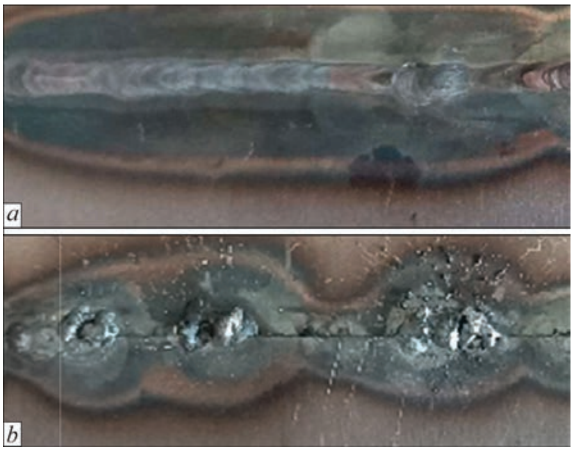

Figure 16. Weld sample: *a* — defectfree section; *b* — defective section

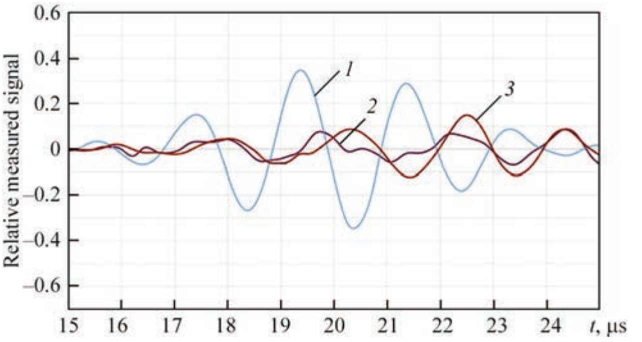

Figure 17. Graphs of MST-receiver signals when testing a welded joint of thin metal sheets; weld samples: *1* — without a defect; *2* — with a defect

UNT method was used. Figure 17 shows fragments of the graphs of MST-receiver signals.

Based on experimental results it was determined that the ultrasonic signal passes through the defect-free section of the weld practically without changing its form and without any additional amplitude reduction. Instead, defects in the weld essentially reduce the received signal amplitude (by more than 2 times), which is a reliable sign of a defect.

Presentation of the results of experimental studies partially includes the materials from [20].

CONCLUSIONS

At present development of innovative UNT methods, materials and products is relevant all over the world, due to introduction and use of new structural materials and manufacturing technologies, need to detect defects in products at early stages of their initiation. The range of promising UNT techniques includes the method based on the use of small-aperture magnetostrictive transducers.

Results of the conducted model and experimental studies led to the following conclusions.

1. The proposed method of direct and reverse conversion of electrical and ultrasonic signals in MST allows increasing the conversion efficiency, but at the same time it leads to ultrasonic signal distortion and its additional delay, which should be taken into account during processing of MST signals and evaluation of their informative parameters, namely amplitude, phase and delay.

2. Experiments using a test sample in the form of a plate from 0.8kp(rimmed) steel with holes of different diameter (1, 2, 3 mm) with application of the shadow UNT method revealed an inverse proportionality between the MST-receiver signal amplitude and hole diameter.

3. Experimental studies were conducted on samples of sheet steel 3 of different thickness (1, 2 and 2.5 mm) which allowed establishing the dependence of the MST-receiver signal during the ultrasonic vibration propagation in the sample on the sample thickness: signal amplitude decreases in inverse proportion to the studied sample thickness.

4. The obtained results when testing samples of sheet material welded joints confirmed the applicability of the UNT method using MST to the problem of defect detection in such welds.

Furtheron it is planned to study the efficiency of the method of UNT with MST for other types of material and different kinds of defects (cracks, lacks of penetration, delamination, etc.), as well as investigate the features of using the signal delay as an informational sign in case of application of Lamb waves to address various UNT problems.

REFERENCES

1. Aquil Ahmad, Leonard J. Bond (2018) *Nondestructive evaluation of materials*. ASM Handbook, Vol. 17, Ninth Edition, American Society for Metals, ASM International.
2. Panasyuk, V.V. (2001) *Fracture mechanics and strength of materials:* Refer. Book. Vol. 5. Non-destructive testing and technical diagnostics. Ed. by Z.T. Nazarchuk. Lviv, PMI [in Ukrainian].
3. Panasyuk, V.V. (2007) *Fracture mechanics and strength of materials:* Refer. Book. Vol. 9. Strength and durability of aviation materials and components. Lviv, Spolom [in Ukrainian].
4. Dzhala, R.M., Dzhala, V.R., Ivasiv, I.B. et al. (2018) *Technical diagnostics of materials and structures:* Refer. Book. Vol. 4. Electrophysical methods of non-destructive testing of defectiveness of structure elements. Ed. by Z.T. Nazarchuk. Kyiv, Prostir-M [in Ukrainian].
5. Kolomiitsev, O.V., Komarov, V.O. (2022) Economical effect and comparison of crack identification in load-bearing element of aircraft wing by methods of non-destructive testing. In: *Proc. of the 10th Inter. Scientific and Practical Conf. on Inter. Scientific Innovations in Human Life, Manchester* [in Ukrainian]. https://sci-conf.com.ua/x-mezhdunarodnaya-nauchno-prakticheskaya-konferentsiya-international-scientific-innovations-in-human-life-13-15-aprelya-2022-goda-manchester-velikobritaniya-arhiv
6. Kim, Y.Y., Kwon, Y.E. (2015) Review of magnetostrictive patch transducers and applications in ultrasonic nondestructive testing of waveguides. *Ultrasonics*, **62**, 3–19. DOI: https://doi.org/10.1016/j.ultras.2015.05.015
7. Vinogradov, S., Fisher, J. (2018) *Review of guided wave testing using magnetostrictive transducers.* 12th ECNDT, Gothenburg, Sweden. https://www.ndt.net/article/ecndt2018/papers/ecndt-0486-2018.pdf
8. Vinogradov, S., Cobb, A., Fisher, J. (2018) New magnetostrictive transducer designs for emerging areas of NDE. *Materials*, **11**, 755. DOI: https://doi.org/10.3390/ma11050755
9. Babak, V.P., Bohachev, I.V., Dekusha, O.L. et al. (2025) Investigation of ultrasonic magnetostriction method of ultrasonic control. Pt 1. Application of magnetostriction effects in measurement and non-destructive testing systems (Review). *Technical Diagnostics and Non-Destructive Testing*, **3**, 5–14 [in Ukrainian]. DOI: https://doi.org/10.37434/tdnk2025.03.01
10. Carlin, B. (1960) *Ultrasonics.* Chapter 4. Magnetostriction. 2nd Ed. Mcgraw-Hill Book Company Inc., 93–125.
11. Babak, V.P., Babak, S.V., Beregun, V.S. et al. (2015*) Information support of monitoring of heat-and-power engineering objects:* Monography. Ed. by V.P. Babak. Kyiv [in Ukrainian].
12. Babak, V.P., Bogachev, I.A. (2016) Small aperture magnetostrictive sensors for non-destructive testing. In: *Proc. of the NDT days 2016, Sozopol, Bulgaria*, 1(**156**).
13. Bohachev, I.V., Babak, V.P., Zaporozhets, A.O. (2022) Novel small-aperture transducers based on magnetostrictive effect for diagnostic systems. *Technical Electrodynamics,* **3**, 69–78. DOI: https://doi.org/10.15407/techned2022.03.069
14. Bohachev, I., Kovtun S., Kuts Y. et al. (2023) Enhanced phase method of signal detection for ultrasonsc magnetostriction defectoscopy of power equipment. *System Research in Energy*, 2(**73**), 72–82. DOI: https://doi.org/10.15407/srenergy2023.02.072
15. Tsapenko, V.K., Kuts, Yu.V. (2010) *Fundamentals of ultrasonic non-destructive testing.* Kyiv, NTUU KPI [in Ukrainian].
16. Crawford, F.S. (1966) *Waves.* Berkeley physics course. Vol. 3. McGraw-Hill.
17. Bendat, J., Piersol, A. (2010) *Random Data. Analysis and Measurement Procedures*. John Willey & Sons.
18. Poularikas, A. (2010) *Transforms and Applications Handbook*. CRC Press LLC.
19. Harb, M.S., Yuan, F.G. (2015) A rapid, fully non-contact, hybrid system for generating Lamb wave dispersion curves. *Ultrasonics,* **61**, 62–70. DOI: https://doi.org/10.1016/j.ultras.2015.03.006
20. Kovtun, S.I., Bohachev, I.V., Dekusha, O.L. et al. (2025) Experimental research of the magnetostrictive method of ultrasonic nondestructive testing. *Bulgarian Society for NDT Inter. J. "NDT Days"*, VIII(**2**), 70–76. https://www.bg-s-ndt.org/journal/vol8.html

ORCID

V.P. Babak: 0000-0002-9066-4307,
I.V. Bohachev: 0000-0001-7781-5767,
O.L. Dekusha: 0000-0003-3836-0485,
S.I. Kovtun: 0000-0002-6596-3460,
Y.V. Kuts: 0000-0002-8493-9474,
S.V. Sozonov: 0000-0002-7584-4529

CONFLICT OF INTEREST

The Authors declare no conflict of interest

CORRESPONDING AUTHOR

Y.V. Kuts
General Energy Institute of the NASU
172 Antonovych Str., 03150, Kyiv, Ukraine
E-mail: y.kuts@ukr.net

SUGGESTED CITATION

V.P. Babak, I.V. Bohachev, O.L. Dekusha, S.I. Kovtun, Y.V. Kuts, S.V. Sozonov (2026) Improvement and experimental research of the magnetostriction method of ultrasonic testing using small-aperture transducers. *The Paton Welding J.*, **08**, 45–53.
DOI: https://doi.org/10.37434/tpwj2026.08.06

JOURNAL HOME PAGE

https://patonpublishinghouse.com/eng/journals/tpwj

Received: 20.02.2026
Received in revised form: 27.06.2026
Accepted: 31.07.2026

XXIV INTERNATIONAL INDUSTRIAL FORUM

Paton International LLC exhibition stand

The **XXIV International Industrial Forum (26–28 May, 2026, Kyiv)** is the largest industrial exhibition in Ukraine. Since 2005, it has been included among the world's leading industrial exhibitions officially certified and recognized by the **Global Association of the Exhibition Industry (UFI)**, representing the highest level of international recognition for exhibition events. The event is organized by **KYIV GLOBAL EXPO LLC**.

The International Industrial Forum comprises specialized exhibitions in the fields of **metalworking, mechanical engineering, and related industries**, as well as an extensive program of scientific and technical conferences, seminars, and exhibitors' presentations. The exhibitions featured leading industrial enterprises from Ukraine and abroad. Every year, the Forum showcases the latest industrial technologies, equipment, tools, components, and services. Annually, the Forum brings together thousands of industrial professionals, equipment manufacturers, technology suppliers, and business representatives from across Ukraine and abroad. The International Industrial Forum is far more than an exhibition — it is the country's premier platform for showcasing innovations, establishing partnerships, exchanging professional experience, and advancing the development of Ukrainian industry.

The XXIV International Industrial Forum is reflected in figures that speak for themselves:

- 427 exhibiting companies;
- more than 23,000 m^2 of exhibition space;
- 13,000 professional visitors;
- 25 business events;
- 12 participating countries (Switzerland, China, Poland, Germany, the Czech Republic, Latvia, Lithuania, Portugal, Romania, Slovakia, Italy, and Ukraine).

Fronius Ukraine LLC exhibition stand

Among the Forum's long-standing participants are leading Ukrainian manufacturers and suppliers of welding and non-destructive testing equipment and materials, including **Paton International LLC**, **Fronius Ukraine LLC**, **ARAMIS LLC**, **BINZEL Ukraine GmbH**, **SUMMIT LLC**, **DONMET Autogenous Equipment Plant**, **Diagnostic Instruments R&D Company LLC**, **KHIMLABORREAKTIV LLC**, **LEM Ukraine LLC**, **Ultrakon LLC**, **Elvatech LLC**, and others.

As part of the International Industrial Forum, the **Second PATON WELDING CUP 2026**, a welding competition for instructors of vocational education and training institutions of Ukraine, was held. The competition was dedicated to the outstanding Ukrainian welding scientists E.O. Paton and B.E. Paton.

The E.O. Paton Electric Welding Institute of the National Academy of Sciences of Ukraine (PWI) has been a regular participant in the International Industrial Forum in recent years. This year, visitors to the Institute's exhibition stand had the opportunity to become acquainted with its latest developments in welding and related technologies. Information was presented together with demonstration samples produced using the following technology:

● Electron beam 3D printing, demonstrated by samples of a gas turbine engine blade, a hip joint implant, and a maxillofacial implant.

● Magnetically impelled arc butt welding of pipes.

● Single-pass welding of steel structures with thicknesses ranging from 6 to 200 mm.

● Electroslag welding of vertical, inclined, and curvilinear joints in metals 30–200 mm thick in a single pass.

Participants, organizers, sponsors, and judges of the welding competition

● Welding and surfacing of copper and copper alloys (including dissimilar welding with steel), as well as restoration of components made of copper and its alloys.

● A narrow-gap gas tungsten arc welding (GTAW) system for titanium with magnetic arc control.

Personalized biopolymer implants with a functionalized surface for bone regeneration.

● A new generation of manual electron beam welding equipment designed for welding operations in outer space.

During the International Industrial Forum, the **PWI** and **PATON PUBLISHING HOUSE LLC** organized two scientific and technical seminars devoted to current issues in **metal additive manufacturing** and **non-destructive testing**.

Seminar "3D Printing of Metallic Components", 26 May, 2026

The seminar was attended by **26 representatives** of research institutions, educational establishments, and industrial enterprises. A total of eight presentations were delivered:

● **Determination of Electron Beam Printing Parameters for Thin-Walled Components Manufactured from VT6 Titanium Alloy**
V.A. Matviichuk, V.M. Nesterenkov, M.O. Sysoiev
PWI, Kyiv, Ukraine.

● **3D Printing of Steel and Alloy Components by Plasma Arc Additive Manufacturing: New Technological Approaches and Equipment Development**
V.M. Korzhyk, V.Yu. Khaskin, Ye.V. Illiashenko, O.S. Tereshchenko, O.Ye. Bozhok
PWI, Kyiv, Ukraine.

Exhibition stand of the PWI

● **Analytical Methods for Investigating Materials and Processes in Metal Additive Manufacturing:**
Solutions from TA Instruments, Micromeritics, RX Solutions, and Physical Electronics
O.V. Rudyk
LEM Ukraine LLC, Kyiv, Ukraine.

● **Multi-Layer Surfacing of Pipeline Sections with Wall-Thinning Defects**
H.V. Vorona, O.S. Kostenevych
PWI, Kyiv, Ukraine.

● **The Economics of Wire-Based Directed Energy Deposition (DED): When the Technology Reduces the Total Manufacturing Cost**
D.V. Kryvoruchko[1], L.B. Kryvoruchko[2], O.D. Kryvoruchko[3]
[1]*Center for Technological Initiatives LLC, Sumy, Ukraine*
[2]*ALDA Research and Production Company LLC, Kyiv Region, Ukraine*
[3]*Heilbronn University, Germany*

● **WAAM Fabrication of Three-Dimensional Components with Adaptive Thermal State Control Using Artificial Intelligence Tools**
I.M. Lahodzinskyi, V.V. Kvasnytskyi, A.V. Chornyi, V.O. Chernii
National Technical University of Ukraine "Igor Sikorsky Kyiv Polytechnic Institute", Kyiv, Ukraine.

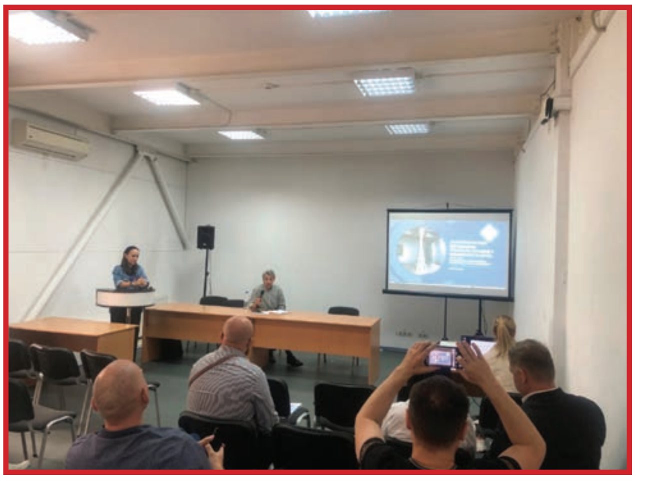

Seminar "3D Printing of Metallic Components". Presentation by O.V. Rudyk

● **Influence of Build Platform Position on Melt Pool Formation for Different Laser Beam Types**
S.V. Adzhamskyi[1], R.V. Podolskyi[1], T.V. Balakhanova[2], O.Ye. Baranovska[2], N.P. Tohobytska[3]
[1]*Additive Laser Technology of Ukraine LLC, Dnipro, Ukraine*
[2]*Z.I. Nekrasov Iron and Steel Institute of the NASU, Dnipro, Ukraine*
[3]*HTW University of Applied Sciences, Berlin, Germany*

● **Structural Characteristics of Steam Turbine Blade Material During Laser Repair Restoration**
O.M. Berdnikova, An Tiancheng, O.S. Kushnariova
PWI, Kyiv, Ukraine.

Seminar "Non-Destructive Testing and Technical Condition Monitoring", 27 May, 2026

The seminar was dedicated to the **30th anniversary of Diagnostic Instruments R&D Company LLC**, a well-known Ukrainian company specializing in non-destructive testing equipment.

More than **30 representatives** of research institutions, educational establishments, and industrial enterprises participated in the seminar. A total of ten presentations were delivered:

● **Non-Destructive Testing Methods for Weld Inspection in the Oil and Gas Industry**
O.V. Pavlii
Diagnostic Instruments R&D Company LLC, Kyiv, Ukraine.

Seminar "Non-Destructive Testing and Technical Condition Monitoring". Presentation by O.V. Pavlii

● **Quality Control in Mechanical Engineering**
O.M. Kozin
Diagnostic Instruments R&D Company LLC, Kyiv, Ukraine.

● **Inspection Methods for Modern Composite and Polymer Products**
O.V. Pavlii, S.M. Hlabets, O.M. Kozin
Diagnostic Instruments R&D Company LLC, Kyiv, Ukraine.

● **Reliability of Non-Destructive Testing of Austenitic Welded Joints: A Case Study of the Chornobyl NPP Unit 3 Pipelines**

V.M. Torop, Ye.O. Davydov, M.D. Rabkina
PWI, Kyiv, Ukraine.

● **Reducing the Human Factor in Ultrasonic Non-Destructive Testing of Pipeline Welded Joints and**
Equipment Using the Wave Ultrasonic Flaw Detector
D.V. Kazarchuk
KHIMLABORREAKTIV LLC, Brovary, Ukraine.

● **Advanced XRF Solutions for Non-Destructive Testing and Technical Diagnostics of Metals**
M.E. Amirseidov
Elvatech LLC, Kyiv, Ukraine.

● **Advanced Thermal Imaging Technologies for the Inspection of Critical Facilities**
V.Yu. Hlukhovskyi
PWI, Kyiv, Ukraine.

● **Activities of Technical Committee for Standardization TC 78 'Technical Diagnostics and Non-Destructive Testing'**
Yu.M. Posypaiko
PWI, Kyiv, Ukraine.

● **The XIV European Conference on Non-Destructive Testing (15–19 June 2026, Verona, Italy)**
Yu.M. Posypaiko
PWI, Kyiv, Ukraine.

● **Application of RX Solutions X-ray Computed Tomography Systems in Non-Destructive Testing:**
Equipment Overview and Technical Capabilities
O.V. Rudyk
LEM Ukraine LLC, Kyiv, Ukraine.

During the seminars

The seminar participants expressed their interest in taking part in future thematic seminars to be organized by the **PWI** and **PATON PUBLISHING HOUSE LLC**.

At the exhibition stand of **PATON PUBLISHING HOUSE LLC**, visitors had the opportunity to become acquainted with the Forum's information partners — the professional journals **Automatic Welding**, **Electrometallurgy Today**, **Technical Diagnostics and Non-Destructive Testing**, as well as **The Paton Welding Journal**, which was indexed in the **Scopus** abstracting and indexing database in **2025**.

The **XXV International Industrial Forum** is scheduled to take place on **25–27 May 2027**.

Oleksandr Zelnichenko, Iryna Romanova (PWI)

INNOVATIVE EQUIPMENT OF THE "PATON INTERNATIONAL" COMPANY

PATON Laser-Pro-1200

The "PATON INTERNATIONAL" LLC Company participated in the International Industrial Forum 2026 — one of the most important events of the Ukrainian industry, which took place on 26–28.05.2026. For three days, the Company stand became a meeting place for welding specialists, representatives of manufacturing enterprises, educational institutions and all those interested in modern welding technologies.

New products at the exhibition. One of the main highlights of the Forum was the PATON LaserPro-1200 laser welding machine. This multifunctional solution combines three capabilities: laser welding, cutting and surface cleaning. The maximum power of the machine is 1200 W. It has sensor control, is powered by a single-phase network and is equipped with a reliable four-roller mechanism for stable wire feed and high quality work.

New welding systems of the MasterTIG series — MasterTIG-200 AC/DC WK and MasterTIG-315-400V AC/DC WK were also presented at the exhibition. Both models are designed for professional welding in TIG AC/DC/MIX, MMA and TIG SPOT (COLD TIG) modes, ensuring effective work with aluminium and copper alloys and steels. These systems are equipped with a cooling unit and are designed for professional (MasterTIG-200 AC/DC WK) and industrial use (MasterTIG-315-400V AC/DC WK). Both models are fitted with TFT displays for comfortable adjustment of welding parameters, have all the necessary functions for units of this specialization and modes, in particular the CLEAN mode, which allows cleaning and polishing of welds and stainless steel surfaces. In addition, the units are equipped with a contactless arc ignition system.

Another new product is the PATON TIGCleaner — a compact unit for electrochemical cleaning and polishing of stainless steel. This equipment effectively removes oxides and annealing colours after welding, restoring the aesthetic appearance of the products and their corrosion resistance.

Among the new products, SynerMIG-500-15-4-400V attracted special attention. The unit is designed for semi-automatic welding and is equipped with the function of synergic control in the pulse mode, which automatically selects the optimal welding parameters, provides a stable arc and high quality of the weld. The model also supports the MMA and TIG modes, which makes it a universal solution for a wide range of production tasks.

Update of popular series of equipment. The updated semi-automatic machine StandardMIG-350–400 V was presented in the Company stand, in which the wire feed unit is located in the upper part of the structure, while the power source is installed below. Moreover, the machine design envisages a place for installing a shielding gas cylinder, making the system more mobile and convenient for use in the production conditions.

Among the key advantages of the model are:

- synergic control in pulsed MIG/MAG mode;
- monoblock design;
- separate closed compartment for a coil with welding wire weighing up to 18 kg;
- four-roller wire feed mechanism.

The Company also presented the StandardCUT-100-400V MAXflow plasma cutter. Thanks to the built-in compressor, the device does not require an additional source of compressed air and provides cutting of metals and alloys up to 35 mm thick. The model is equipped with a pilot arc, a non-contact ignition unit (oscillator) and a pneumatic system with two valves, which increases the reliability and comfort of the user's work.

A new direction is air purification systems. During the Forum, the Company also presented AirGUARD — a local exhaust ventilation system for welding work. This system is designed to effectively remove and clean the air from smoke, dust, welding aerosols and other harmful particles formed during welding. The use of PATON AirGUARD contributes to the creation of safer and more comfortable working conditions for welders and production personnel.

Participation results. The presented new products of PATON INTERNATIONAL LLC confirmed the Company's desire to develop innovative solutions for professional and industrial applications, and support for educational initiatives was another demonstration of the contribution of the PATON brand to shaping the future of the welding industry in Ukraine.

Bogdan Bogdanov,
PATON INTERNATIONAL LLC